University of Cape Town
Department of Physics

5

THE RESPONSE OF ORGANIC SCINTILLATORS TO NEUTRONS OF ENERGY 14-63 MeV

A. BUFFLER

A thesis submitted to the
University of Cape Town
for the degree of
Master of Science

December 1990

ABSTRACT

The response of a 5 cm (diameter) by 5 cm cylindrical NE213 liquid scintillator to neutrons has been measured as a function of neutron energy in the range 15-63 MeV, using time-of-flight to select neutron energy. The response function at each neutron energy was separated into components associated with the emission of different charged particles, identified by pulse shape discrimination to be protons, deuterons and alphas, respectively. The response (light output) of NE213 to protons, deuterons and alphas was measured as a function of energy. Furthermore, total cross sections for neutron-induced proton, deuteron and alpha production from ^{12}C were determined from the charged particle yields. The simultaneous presence of n-p elastic scattering in the scintillator provided a reference for establishing an absolute cross section scale for the measurements. The results give information about reaction mechanisms and provide an improved basis for determining the neutron detection efficiency of the scintillator as a function of energy over this range.

ACKNOWLEDGEMENTS

The author wishes to express his thanks to the following:

His supervisor, Prof. F.D. Brooks, for his selfless assistance, untiring encouragement and support;

The staff of the National Accelerator Centre for their co-operation and use of their facilities;

The students and staff of the Physics Department, University of Cape Town; in particular, Mr. C.G.L. Henderson, for extensive discussion and use of his Monte Carlo code, and Mr. M.S. Allie for his assistance and guidence.

The Foundation for Research Development for financial assistance.

TABLE OF CONTENTS

LIST OF TABLES

LIST OF FIGURES

CHAPTER 1

INTRODUCTION

The scintillation detector is one of the most extensively used particle detection devices in both basic and applied nuclear and particle physics today. Ionization and excitation produced by a charged particle slowing down in the scintillator medium leads to the emission of a flash of light - a **scintillation.** This scintillation may be translated into an amplified electronic pulse by a photomultiplier tube and the characteristics of this pulse (amplitude and time-dependence) provide information about the charged particle such as its energy and type (e.g. electron, proton, deuteron, etc.). If the photomultiplier output is integrated by using a time constant which is long compared with the scintillation lifetime, the amplitude or 'height' of the resulting pulse will be proportional to the total light in the scintillation. This integrated or total light is known as the **response** of the scintillator. The dependence of scintillator response on the type and energy of particle causing the light output is an important characteristic of scintillators.

Organic detectors consisting predominantly or entirely of hydrocarbons form an important class of scintillators. They are particularly suited for

neutron detection, the neutron being detected indirectly via the secondary protons or other charged particles released in its interactions with the hydrogen or carbon nuclei in the organic material. At low incident neutron energies, E_n < 20 MeV, n-p elastic scattering is the dominant process. For incident neutron energies, E_n > 8 MeV, the neutron can break a ^{12}C nucleus up into three alpha particles. As E_n increases further, the ^{12}C nucleus can be disintegrated into any one of a variety of allowed combinations of neutrons, protons, deuterons, tritons, ^{3}He ions, alphas, and lithium, beryllium and boron ions. All in all, 65 reaction channels for 90 MeV neutrons on ^{12}C have been listed (see table I) by Kellogg (Ke53), each of which includes one or more charged particles included in the products.

In this work, carried out at the low-resolution neutron time-of-flight spectrometer facility at the National Accelerator Centre (NAC), attention was confined to the neutron energy range 15-63 MeV and focussed on the results obtained using the liquid organic scintillator NE213. This scintillator is well-known for its good **pulse shape discrimination,** which allows one to distinguish the scintillations from different types of charged particle via differences in their scintillation decay characteristics.

1.1 RESPONSE VERSUS ENERGY CHARACTERISTICS OF ORGANIC SCINTILLATORS.

One of the best known properties of the organic scintillators is the non-linear dependence of their response on particle energy. A semi-empirical model for the behaviour of the response of organic scintillators, proposed by Birks (Bi51) in 1951 within four years of the first publication on organic scintillator counters (Ka47), provides a good description of these characteristics. Birks proposed that the non-linear response is caused by quenching effects in the scintillator governed by dE/dx, the specific energy loss, or energy deposited per unit length in the track of the ionizing particle. In organic scintillators the light output for a given energy loss is less when the

(i) production of carbon isotopes

^{12}C (n;n) ^{12}C
^{12}C (n;2n) ^{12}C
^{12}C (n;3n) ^{12}C

(ii) production of boron isotopes

^{12}C (n;p) ^{12}B
^{12}C (n;p,n) ^{11}B
^{12}C (n;p,2n) ^{10}B
^{12}C (n;p,4n) ^{8}B
^{12}C (n;d) ^{11}B
^{12}C (n;d,n) ^{10}B
^{12}C (n;p,d,3n) ^{8}B
^{12}C (n;t) ^{10}B
^{12}C (n;t,2n) ^{8}B

(iii) production of beryllium isotopes

^{12}C (n;2p,n) ^{10}Be
^{12}C (n;2p,2n) ^{9}Be
^{12}C (n;2p,4n) ^{7}Be
^{12}C (n;d,p) ^{10}Be
^{12}C (n;d,p,n) ^{9}Be
^{12}C (n;d,p,3n) ^{7}Be
^{12}C (n;2d) ^{9}Be
^{12}C (n;2d,2n) ^{7}Be
^{12}C (n;t,p) ^{9}Be
^{12}C (n;t,p,2n) ^{7}Be
^{12}C (n;t,d,n) ^{7}Be
^{12}C (n;α) ^{9}Be
^{12}C (n;α,2n) ^{7}Be

(iv) production of $Be^{*} \rightarrow 2\alpha$

^{12}C (n;α,n) 2α
^{12}C (n;^{3}He,2n) 2α
^{12}C (n;2p,3n) 2α
^{12}C (n;p,d,2n) 2α
^{12}C (n;p,2d,n) 2α
^{12}C (n;p,t,n) 2α
^{12}C (n;d,t) 2α

(v) production of lithium isotopes

^{12}C (n;3p,n) ^{9}Li
^{12}C (n;3p,2n) ^{8}Li
^{12}C (n;3p,3n) ^{7}Li
^{12}C (n;3p,4n) ^{6}Li
^{12}C (n;p,^{3}He) ^{9}Li
^{12}C (n;p,^{3}He,n) ^{8}Li
^{12}C (n;p,^{3}He,2n) ^{7}Li
^{12}C (n;p,^{3}He,3n) ^{6}Li
^{12}C (n;p,α) ^{8}Li
^{12}C (n;p,α,n) ^{7}Li
^{12}C (n;p,α,2n) ^{6}Li
^{12}C (n;d,^{3}He) ^{8}Li
^{12}C (n;d,^{3}He,n) ^{7}Li
^{12}C (n;d,^{3}He,2n) ^{6}Li
^{12}C (n;2p,d) ^{9}Li
^{12}C (n;2p,d,n) ^{8}Li
^{12}C (n;2p,d,2n) ^{7}Li
^{12}C (n;2p,d,3n) ^{6}Li
^{12}C (n;p,2d) ^{8}Li
^{12}C (n;p,2d,n) ^{7}Li
^{12}C (n;p,2d,2n) ^{6}Li
^{12}C (n;d,α) ^{7}Li
^{12}C (n;d,α,n) ^{6}Li
^{12}C (n;t,^{3}He) ^{7}Li
^{12}C (n;t,^{3}He,n) ^{6}Li
^{12}C (n;3d) ^{7}Li
^{12}C (n;3d) ^{7}Li
^{12}C (n;p,d,t) ^{7}Li
^{12}C (n;p,d,t,n) ^{6}Li
^{12}C (n;^{6}Li) ^{7}Li
^{12}C (n;^{6}Li,n) ^{7}Li
^{12}C (n;t,α) ^{6}Li
^{12}C (n;2d,t) ^{6}Li

Table I *Reaction channels for interactions of 90 MeV neutrons with ^{12}C* (Ke53).

density of ionization is high. Birks suggested a model relating the scintillation photons emitted per unit length, dL/dx, to dE/dx, of the form:

$$dL/dx \propto \frac{dE/dx}{(1 + B\, dE/dx)} \tag{1.1}$$

where B is the so-called 'Birks parameter', and $B\ dE/dx$ is the quenching probability which depends on dE/dx produced by the particle. The Birks parameter is usually found by fitting the Birks relation to experimental data.

The specific ionization density along the track of a charged particle moving through the scintillator depends on the energy, mass and charge of the particle as governed by the Bethe-Bloch relation. Therefore the scintillator response at a particular energy will characteristically depend on the type of ionizing particle and the light output is found to become more non-linear for more heavily ionizing particles.

By way of illustration, figure 1.1 shows the calculated response of the plastic scintillator NE102 to protons, deuterons, tritons and alphas presented by Gooding and Pugh (Go60), based on their measurements of the response of NE102 for protons from 28 to 147.5 MeV and for deuterons from 46 to 120 MeV. It can be seen, for example, that a 100 MeV alpha particle will have the same light output as a 50 MeV proton.

As the different organic detectors vary mainly by the relative proportions of hydrogen and carbon (although with different additives), their response to charged particles (indicated by the value of B) does not differ to a great extent between the various organics. Hence accurate knowledge of the response of one type of organic scintillator is valid to a good approximation for the family of hydrocarbon scintillators. By measuring, for example, the ratio L_d/L_p, where L_d and L_p are responses for deuterons and protons at a fixed energy, a comparison may easily be made between different measurements or calculations.

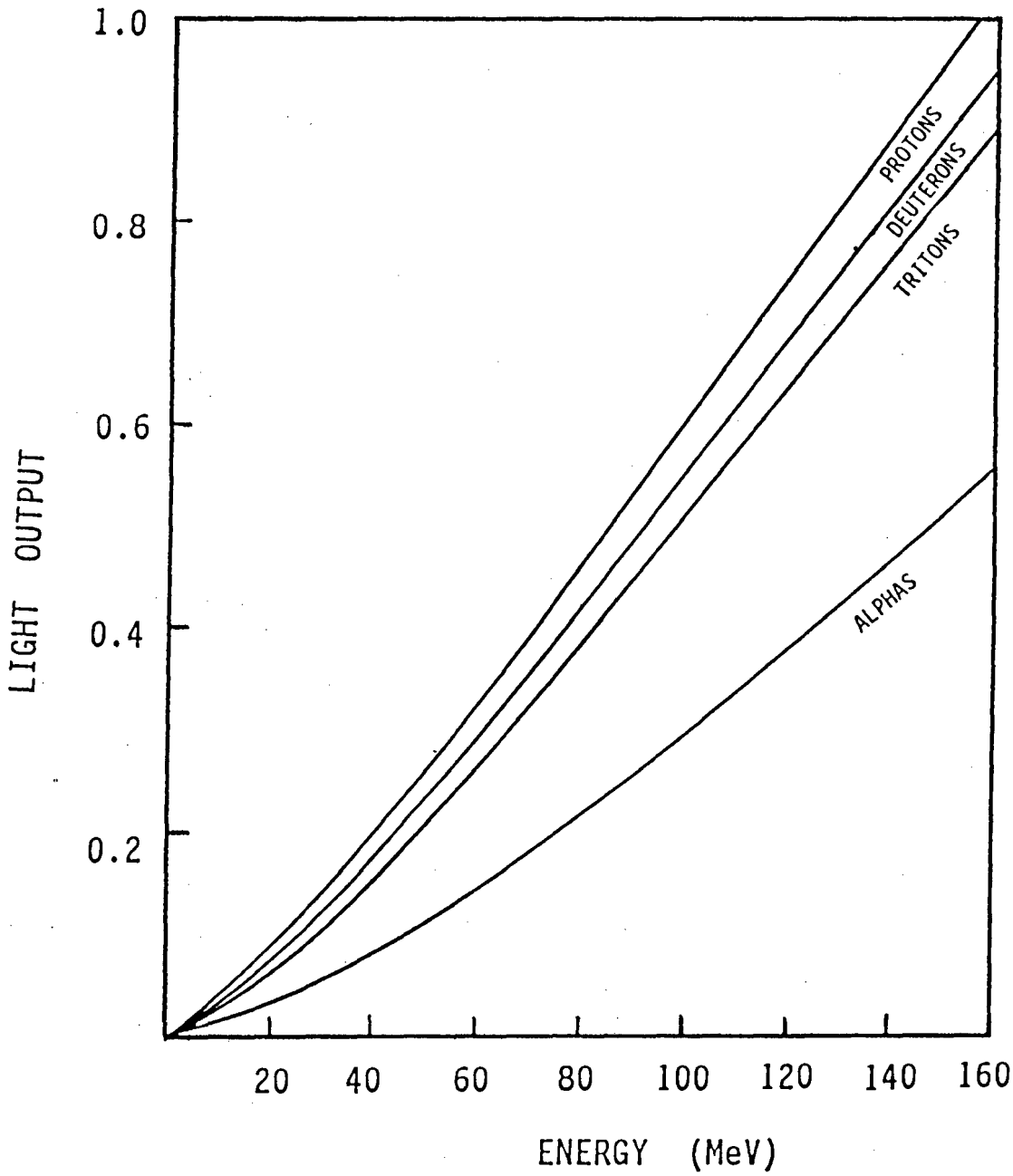

Figure 1.1 The calculated response (Go60) *of NE102A plastic scintillator to protons, deuterons, tritons and alpha particles. The scintillator response to a 160 MeV electron on this scale would be 1.16.*

1.2 PULSE SHAPE DISCRIMINATION

The scintillation time-decay of many organics may be described as the sum of a "fast" exponential component (lifetime typically less than 5 ns) and a "slow" non-exponential component (mean lifetime greater than 100 ns) as illustrated schematically in figure 1.2 (Vo68). For certain organic scintillators the relative intensities of these so-called "fast" and "slow" scintillation components depends on the type of charged particle that caused the scintillation. This offers the method of discriminating between different types of ionizing particles by comparing these components. This forms the basis of **pulse shape discrimination.**

Figure 1.3(a) shows measurements by Lynch (Ly75) of the average scintillation decay shapes of NE213 when excited by incident neutrons and gamma rays respectively. The two measurements have been normalized at the scintillation peaks to best illustrate the different proportions of fast and slow components in the scintillation decays. Figure 1.3(b) shows the integrals of the measured curves of figure 1.3(a) normalized at t = 500 ns. The "fast" pulse integral, measured from the start (t = 0) up to a certain fixed time value, say 50 ns, is a smaller fraction of the total integral for neutrons (72%) than for gammas (92%) due to the different shapes of their pulses. Therefore the light output pulses from neutrons and gammas may be distinguished from one other by comparing "fast" and "slow" integrals. To this end, a variety of electronic methods have been devised, for example see (Br79).

The detection of neutrons in organics relies on detecting the recoil particles (p, d, etc.) from neutron-induced events in the detector. The difference in response of organics to different charged particles allows a further discrimination between the pulses from neutron-induced events releasing these different particles. For example, the shape of the light output pulses for protons, will differ from those for deuterons, and the type of charged particle released in the event may be identified.

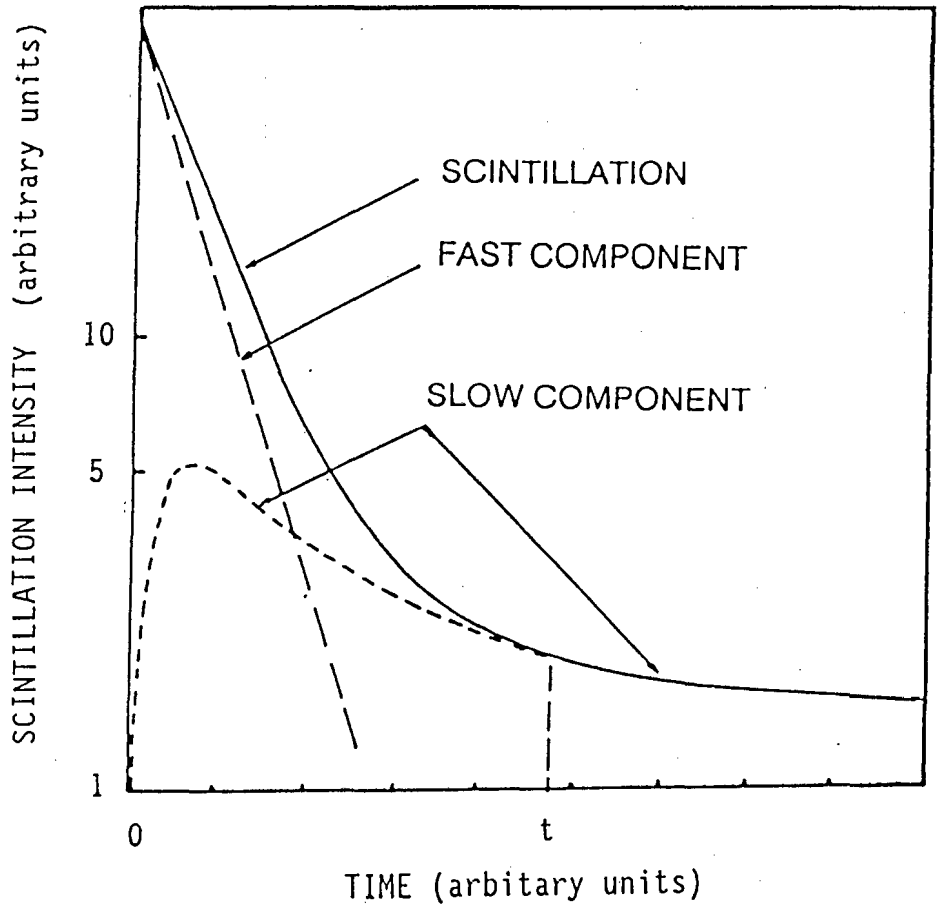

Figure 1.2 Schematic representation (Vo68) *of the scintillation decay of an organic scintillator showing the "fast" and "slow" components.*

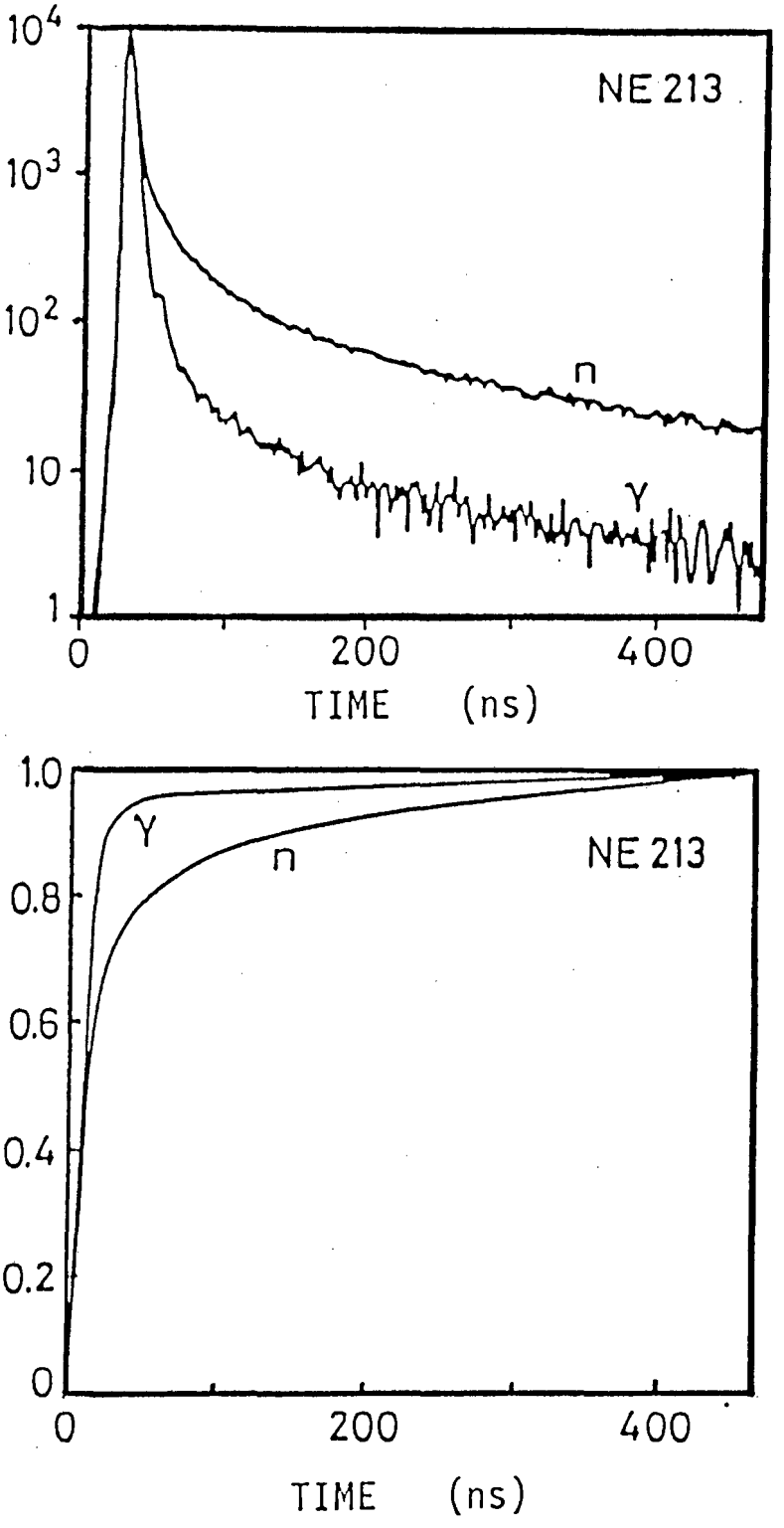

Figure 1.3 *(a) (above)* *Measured light intensity versus time t* (Ly75) *for scintillations produced by gamma rays and neutrons in an NE213 liquid scintillator*

(b) (below) *Integrals of measured curves in (a), normalised at t = 500 ns.*

Figure 1.4 (St75) is an example of the detail that can be resolved by pulse shape analysis of scintillation events caused by fast neutrons. Shown is an isometric spectrum of counts versus pulse height (particle energy) and pulse shape (type of particle) for events in NE213 liquid scintillator which was exposed to nearly monoenergetic 37.5 MeV neutrons.

1.3 THE RESPONSE FUNCTION OF NE213

The response function - or **lineshape** - of a scintillator to a particular type of incident particle or radiation of specific energy, is defined as the scintillation pulse height spectrum resulting from all interactions of that particle or radiation in the scintillator. The lineshape will thus be depend on:

(i) the energy of the incident radiation,
(ii) the types of interaction induced by the incident particles or radiation in the scintillator, and their cross sections, and
(iii) the type, size, shape and geometry of the detector.

The response function for neutrons incident on NE213 may be understood as having two sources of contribution from ionizing particles, namely: (i) recoiling protons from n-p elastic scatterings and (ii) outgoing charged particles produced from neutron-induced interactions with ^{12}C nuclei. These components differ in relative proportion at different incident neutron energies, depending on the cross sections of the competing nuclear reactions.

(a) THE RESPONSE FUNCTION TO LOW ENERGY MONOENERGETIC NEUTRONS (< 10 MeV)

Although outside the scope of this work the scintillator response function to low energy neutrons serves to illustrate features which remain important in the high energy domain which is our concern. At these low energies the major

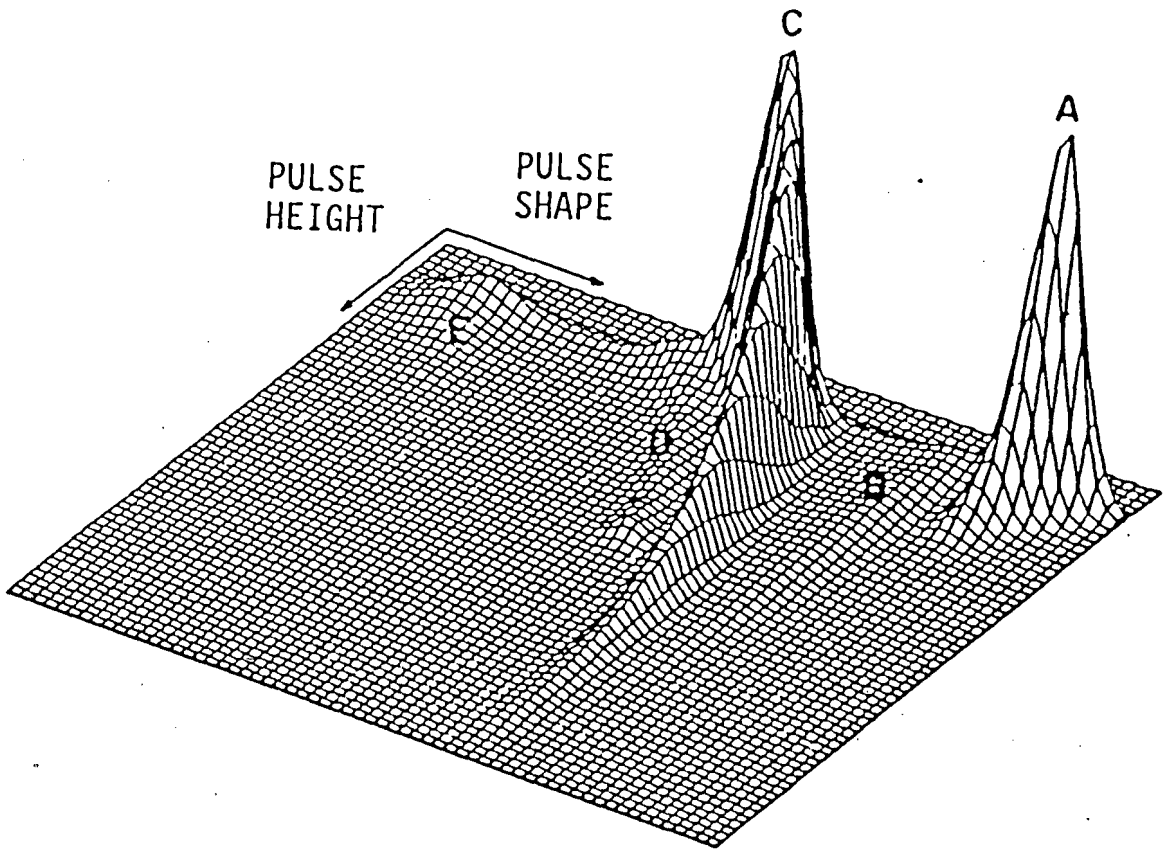

Figure 1.4 Counts (vertical) as a function of pulse height and pulse shape for events in a cylindrical 4.44 cm (diameter) by 1.91 cm NE213 liquid scintillator when exposed to radiation from a ^{7}Li target bombarded by 40 MeV protons (St75). *The ridges labelled* **A-E** *are associated with:* (**A**) *Compton electrons;* (**B**) *recoil protons which escape at the edge of the scintillator;* (**C**) *recoil protons from n-p scattering;* (**D**) *protons from the $^{12}C(n,p)^{12}B$ reaction; and* (**E**) *alpha particles from the $^{12}C(n,\alpha)^{9}Be$ and $^{12}C(n,n')3\alpha$ reactions.*

contritribution to the response function is from protons recoiling from n-p elastic scattering events.

Figure 1.5 (Ga70) shows fits of 2nd order Legendre polynomials to measurements of $d\sigma/d\Omega$ for the $^1H(n,n)^1H$ process. At low incident neutron energies, the angular distribution for n-p elastic scattering may be regarded, to a good approximation, as being isotropic in the centre-of-mass system. This yields a nearly flat proton energy distribution from zero up the the maximum kinematically allowed energy which is equal to the incident neutron energy.

(b) RESPONSE FUNCTION TO 14-63 MeV NEUTRONS

There have not been many measurements of the response function of the liquid organic scintillator NE213 to high energy neutrons. Lockwood *et al* (Lo76) measured lineshapes of NE213 to incident neutrons in the range 2-75 MeV. Pulse shape discrimination was used to extract proton pulse height spectra from a matrix of pulse shape versus pulse height signals. The authors stressed the importance of measuring these response functions at high energies, particularly because of the contributions from neutron-induced reactions on carbon which become competitive at $E_n > 20$ MeV. The suggestion is made by Lockwood that with better pulse shape resolution and hence better particle separation, cross sections for neutron-induced charged particle production from carbon could be accurately determined from pulse height spectra measured in this way.

The two competing processes are now discussed separately:

(i) n-p elastic scattering: With increasing incident neutron energy, p-wave and higher order scattering begins to contribute significantly, and the $^1H(n,n)^1H$ differential cross section becomes more forward-backward peaked in the centre-of-mass system (see figure 1.5) . This will affect the response function measured at higher incident neutron energies. Figure 1.6 shows the

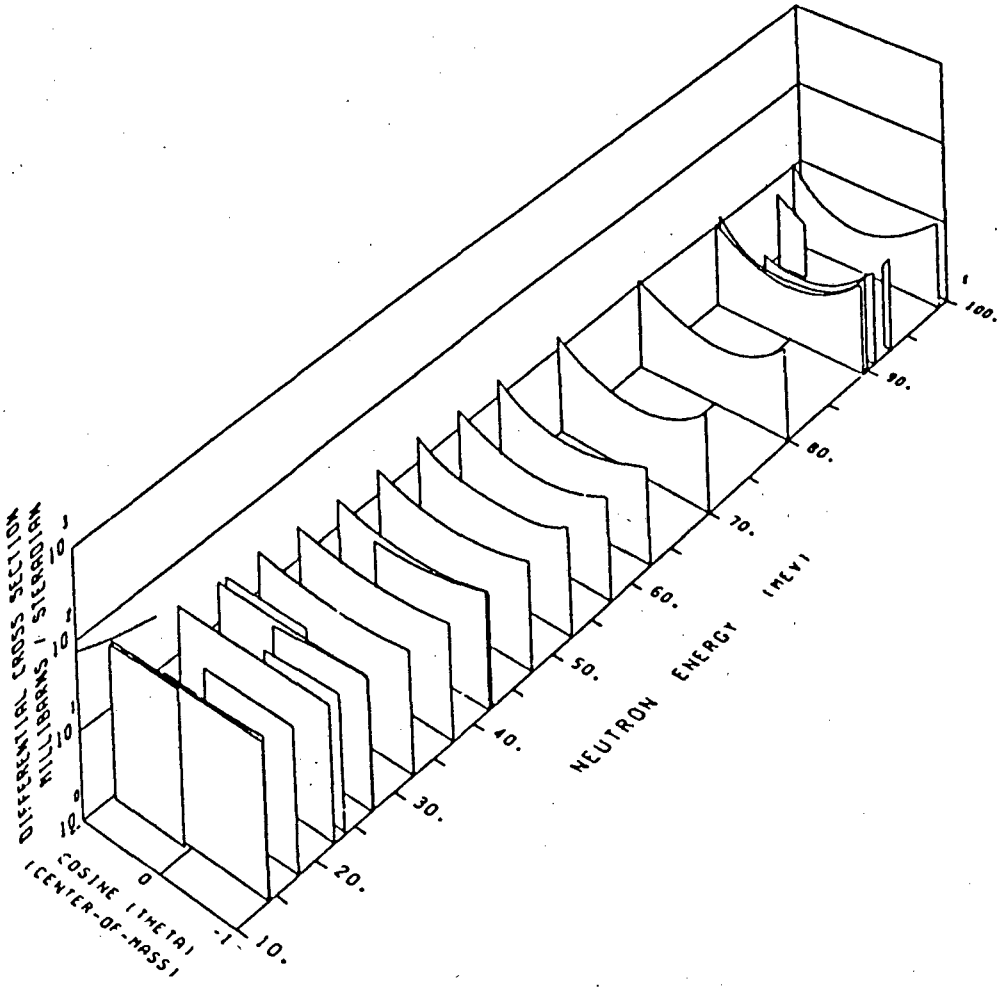

Figure 1.5 Legendre polynomial fits (Ga70) *to measured n-p differential cross section data (not shown) as a function of incident neutron energy. The curves are seen to become increasingly forward-backward peaked with increasing neutron energy.*

numerous measurements of the $^{1}H(n,n)^{1}H$ total cross section, together with a theoretically predicted curve (St64).

(ii) n-^{12}C interactions: As the energy of the incident neutron increases beyond 14 MeV, an increasing number of reactions releasing protons, deuterons, tritons and ^{3}He become energetically feasible. Extensive data have been reported for neutron induced complex charged particle production around 20 MeV (De65, Ri68, Kr59). Figure 1.7 shows the recommended cross sections proposed by Lachkar *et al* (La75) for the $^{12}C(n,p)^{12}B$, $^{12}C(n,d)^{11}B$, $^{12}C(n,\alpha)^{9}Be$ and $^{12}C(n,n')3\alpha$ reactions at $E_n \leq 20$ MeV

Del Guerra (De76) presented an extensive compilation of the neutron inelastic cross sections on carbon for neutrons in the energy range 1-300 MeV. These cross sections are shown in figure 1.8 together with the recommended cross sections (curves) which were used in a Monte Carlo code by Del Guerra to calculate neutron detection efficiencies of organic scintillators. It has been pointed out (Ce79) that the $^{12}C(n,np)^{11}B$ channel is the most important reaction channel at these higher energies where its cross section exceeds the $^{1}H(n,n)^{1}H$ elastic cross section. However, it can be seen that there is a deficiency of measurements at $E_n > 20$ MeV of the cross sections for the different n-^{12}C reaction channels.

Alpha-producing carbon reactions have been studied for $E_n < 20$ MeV (An75) and a critical evaluation of the n-^{12}C interaction cross sections up to 20 MeV has been performed (La75). The sequential breakup reaction $^{12}C(n,n')3\alpha$ induced by neutrons in the energy range 10 to 35 MeV has been studied (An83) and the different reaction channels have been identified.

It can be seen that the lineshapes of organic scintillators to neutrons of energy greater than 20 MeV will be complicated and will include contributions from all interactions releasing charged particles in their products. Figure 1.9 shows the measured and calculated response function of a cylinder (2.54 cm x 7.62 cm) of NE218 to 40.1 MeV neutrons (An79). The hatched area schematically shows the contribution to the lineshape from recoiling n-p scattered protons as compared to the n-^{12}C componant. The

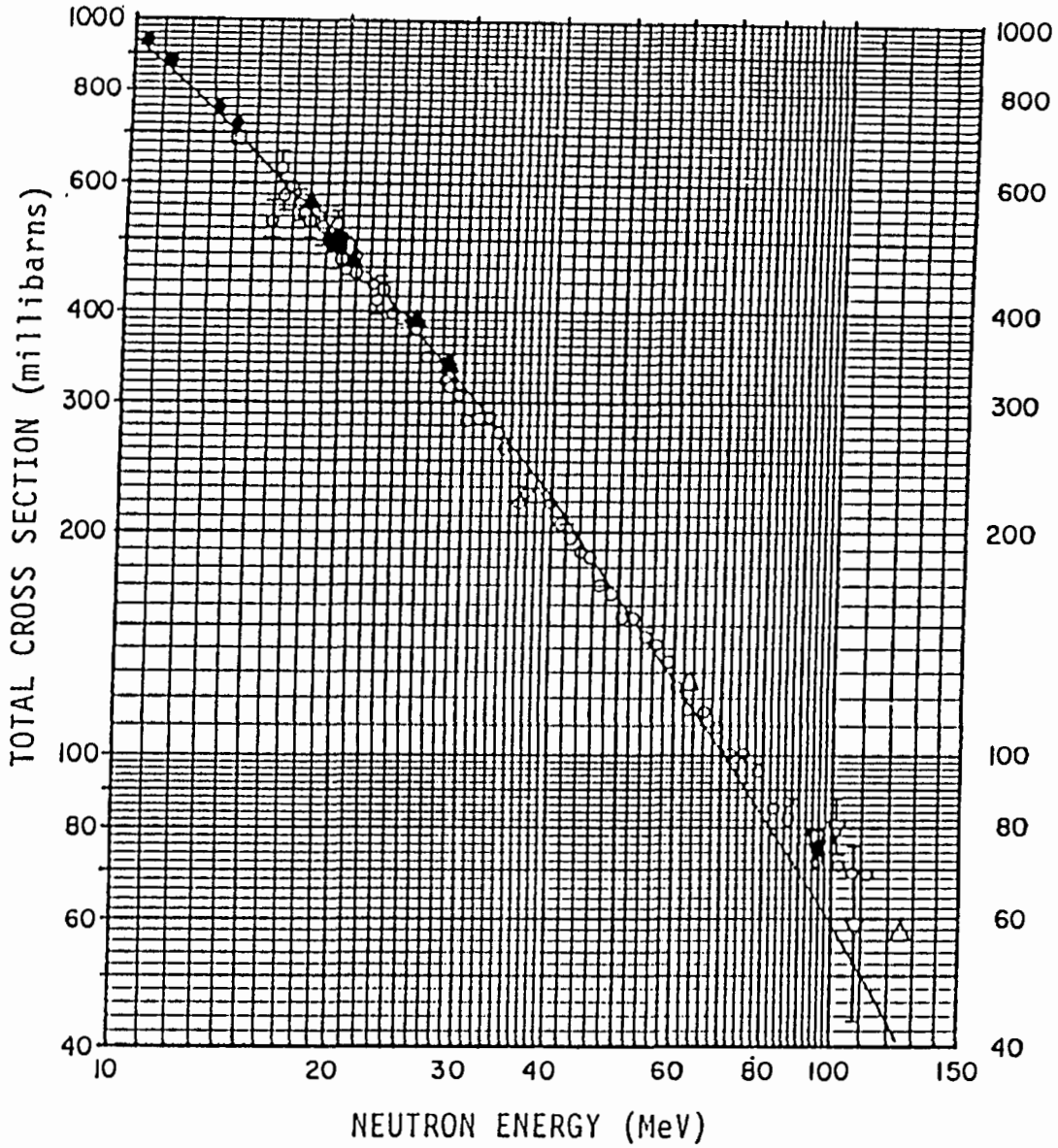

Figure 1.6 A compilation of total cross section measurements (St64) *for* $^{1}H(n,n)^{1}H$ *together with a theoretical curve (see reference).*

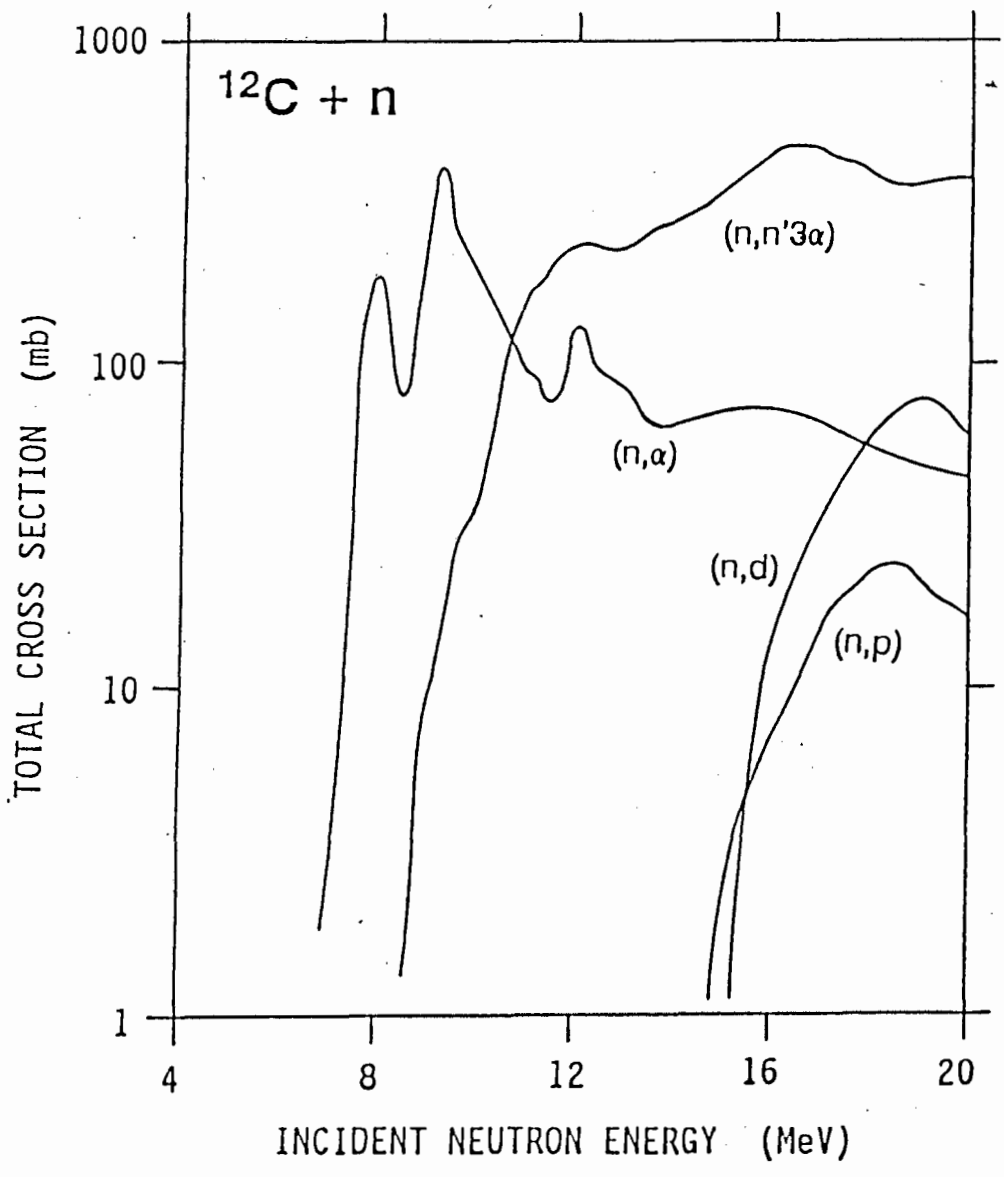

Figure 1.7 Recommended cross sections (La75) *for* $E_n < 20$ *MeV for the* $^{12}C(n,p)^{12}B$, $^{12}C(n,d)^{11}B$, $^{12}C(n,\alpha)^{9}Be$ *and* $^{12}C(n,n')3\alpha$ *reactions.*

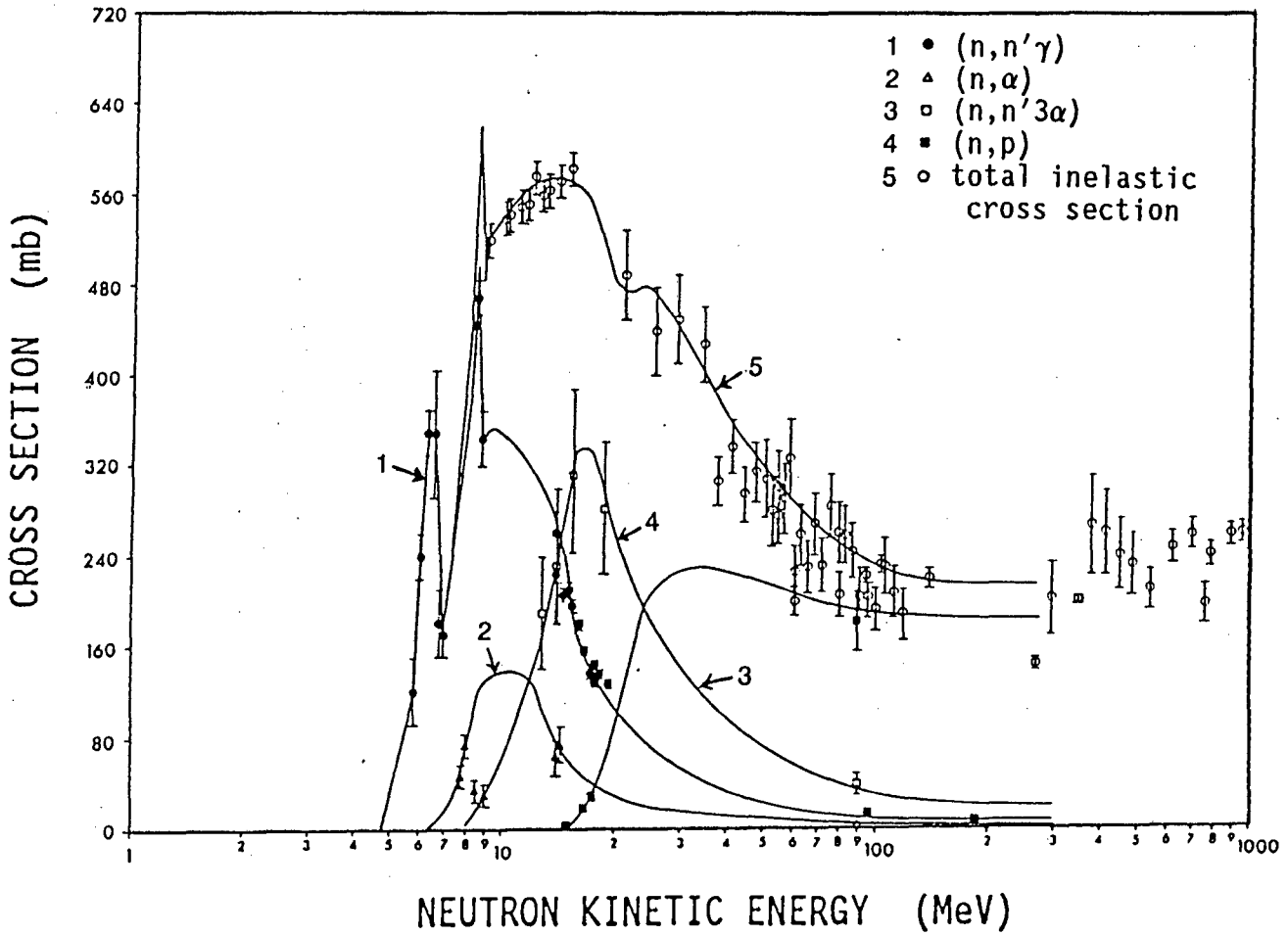

Figure 1.8 A compilation of cross section measurements (De76) *for neutron-induced reactions on ^{12}C. The lines show the cross sections used in a Monte Carlo program* (De76) *to calculate neutron detection efficiencies of organic scintillators.*

upper energy limit for protons released from the $^{12}C(n,p)^{12}B$ reaction is also indicated in the figure.

1.4 NEUTRON DETECTION EFFICIENCY

Accurate knowledge of the efficiency of hydrocarbon scintillation neutron detectors is important in many experiments involving measurements of fast neutron spectra. However, this has become one of the persistent problems in work using organic detectors due to the complexity of the neutron response function. To this end there has been a steady development over the years in sophistication in both experimental techniques and in Monte Carlo codes which are used to estimate detection efficiencies.

Early work in the field (Ku64, Te68, Ve68, St71, Th71, Ed72, El74) led to a variety of methods for calculating neutron detection efficiencies but the results that were predicted were firstly at variance with each other and were not able to reproduce the experimentally determined values, being as much as 30% in disagreement at energies above 40 MeV.

As a first approximation the efficiency was calculated assuming only n-p scattering events in the detector. As a result, early codes were able to emulate the measured scintillator response functions well for neutron energies less than 20 MeV but were not as successful with increasing E_n. Montgomery (Mo73) pointed out the important contribution from neutron-carbon reactions in hydrocarbon neutron detectors. McNaughton and Brady (Mc74) reported on work done on the neutron detection efficiency of NE102A plastic scintillator in the energy range 6 to 41 MeV. They subsequently improved their predictions by using measurements of the differential cross sections for the $^{12}C(n,p)^{12}B$ and $^{12}C(n,d)^{11}B$ reactions at 56 MeV (Mc75).

Cecil (Ce79) was able to make improvements to the code of McNaughton by incorporating new measurements of scintillator light response to protons introduced by Madey *et al* (Ma78) and thought was given to effects due to

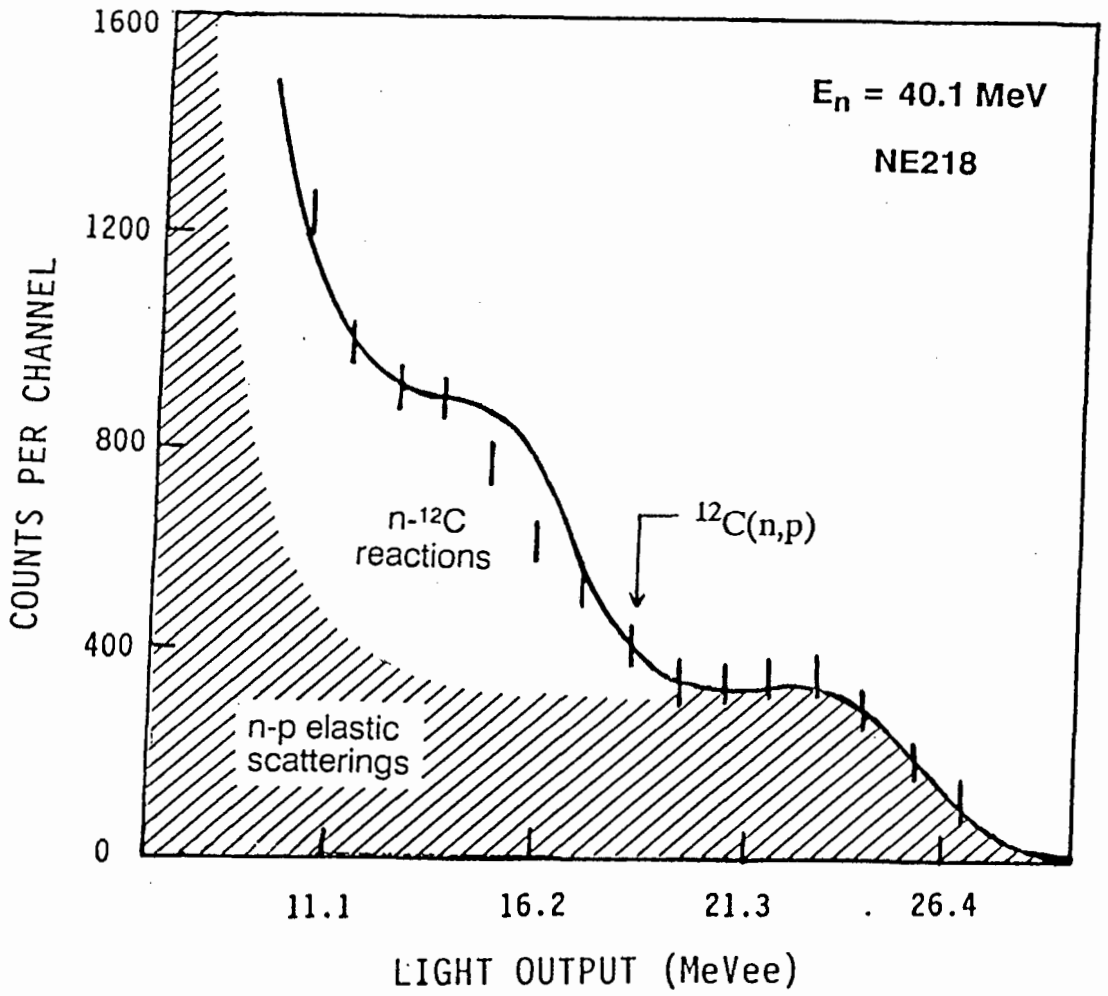

Figure 1.9 Response function (An79) *of a 2.5 cm (diameter) by 7.62 cm cylindrical NE218 liquid scintillator measured for incident neutrons of 40.1 MeV. The full curve is the result of a Monte Carlo calculation. The separation of the two components of the response function, namely protons recoiling from n-p elastic scattering events, and charged particles released from neutron-induced carbon reactions in the scintillator, is also schematically shown. The upper energy limit for protons released in the $^{12}C(n,p)^{12}B$ reaction is indicated.*

escaping charged particles. Shown in figure 1.10 is the calculated neutron detection efficiency for a 13 cm x 13 cm cylindrical cell of NE213 as predicted by the Cecil code.

The new measurements of the n-^{12}C cross sections (De76) largely resolved previously reported discrepancies between efficiency data and the predictions of the Kurz (Ku64), Stanton (St71) and *O5S* (Te68) codes. Both measured and predicted efficiencies were now found to rise rapidly at threshold to a low energy peak around 10 MeV (dominated by n-p elastic scattering in the detector); with increasing energy the efficiency falls as the n-p cross section falls, and then rises again as interactions with carbon begin to contribute significantly, and finally at high energies the efficiency falls steadily as all contributing cross sections fall.

More recently a code, *SCINFUL*, has been developed by Dickens (Di88) to provide full scintillator response to neutron detection for E_n between 0.1 and 80 MeV. The breakup of ^{12}C into final reaction channels having two, three or four outgoing charged particles has been simulated. Measurements of double differential cross sections for the neutron induced production of p, d, t, ^{3}He and alpha particles from carbon have been made by Subramanian *et al* (Su83). These data were combined to provide angle-integrated differential cross sections for measured outgoing particle energy. Figure 1.11 shows a comparison (Di89) between the measurements of Subramanian *et al* and the predictions of the Dickens code. It can be seen that the program provides quantitative differential results that are generally agree within ± 25 % of the measurements.

1.5 SCOPE AND AIMS OF THIS WORK

This experiment was performed as part of a project in which the differential cross section for n-p radiative capture is being measured at E_n = 63 MeV (see Appendix C). In the n-p capture experiment, an NE213 liquid scintillator is used as an active target, i.e. used to provide the target

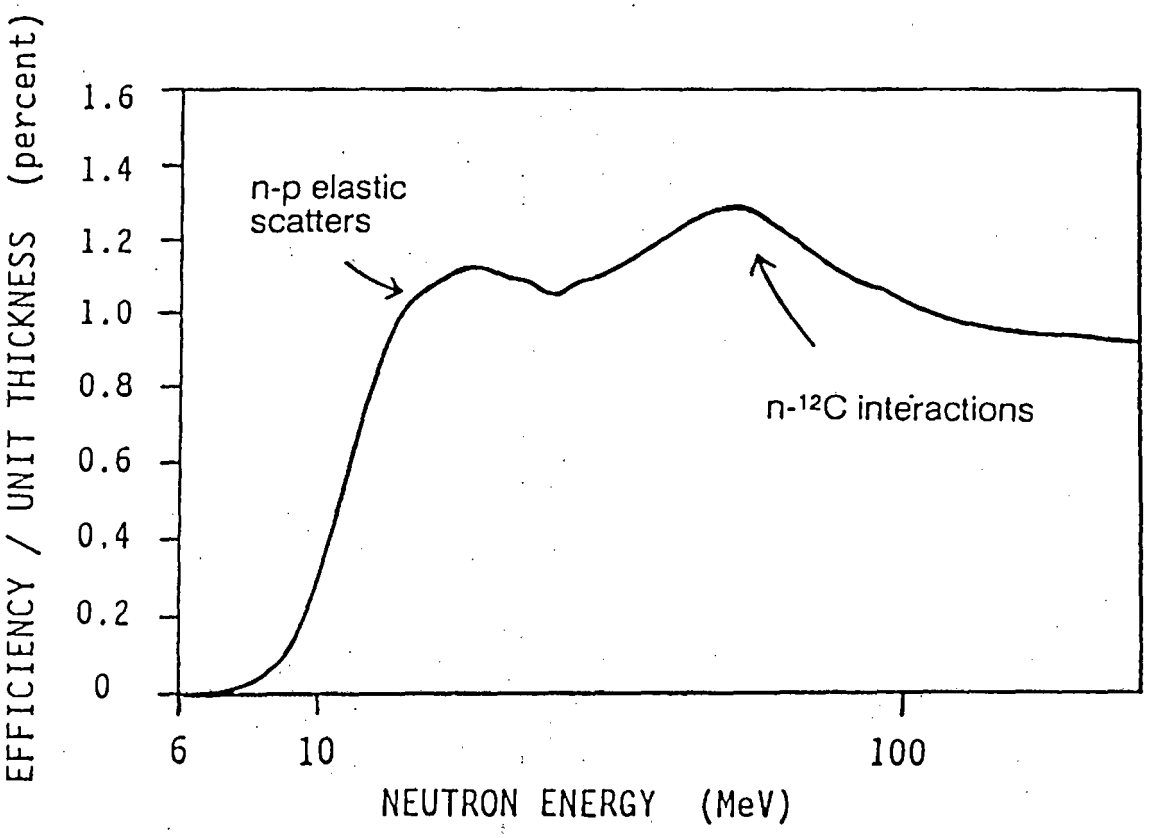

Figure 1.10 Calculated neutron detection efficiency (Ce79) *of a 13 cm (diameter) by 13 cm cylinder of NE213 liquid scintillator, normalized to the scintillator thickness in g/cm²* (By89)*, for a detection threshold of 6 MeVee. Indicated are features attributed to n-p elastic scatterings and n-^{12}C reactions in the scintillator respectively.*

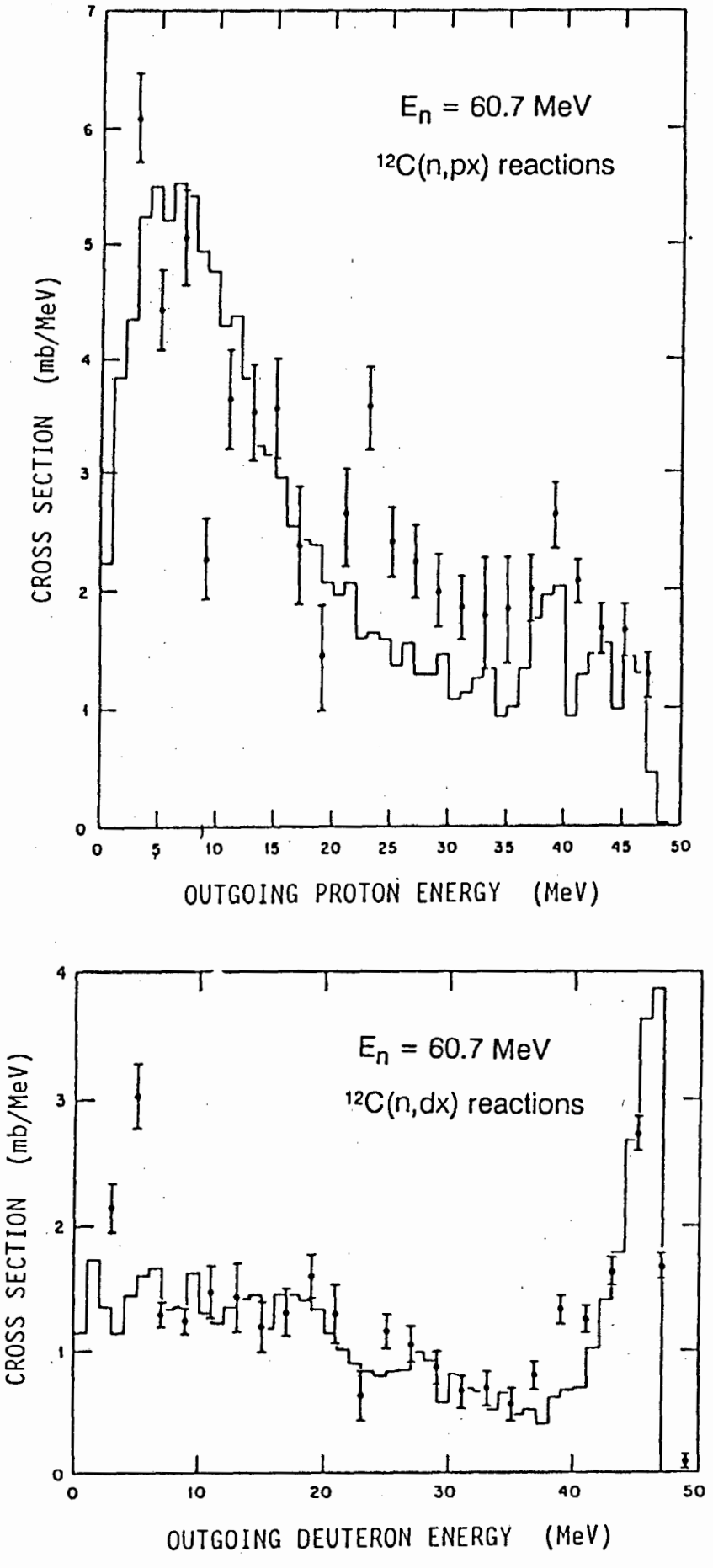

Figure 1.11 Comparison (Di89) *of the predictions of* SCINFUL (Di88) *with the measured data of Subramanian et al* (Su83) *for the integrated (a) proton (above); and (b) deuteron (below) spectra following 60.7 MeV neutron interactions with* ^{12}C.

protons, as well as detecting the deuterons formed in capture events. The simultaneous monitoring of n-p elastic scattering in the scintillator allows the $^{1}H(n,\gamma)^{2}H$ measurements to be transformed to an absolute cross section scale. The ratio of n-p elastic scatters to n-p radiative captures may be related to the $^{1}H(n,\gamma)^{2}H$ total cross section by the well known $^{1}H(n,n)^{1}H$ total cross section in the literature. To this end, a careful evaluation of the neutron-induced interactions in the scintillator was required to separate the n-p elastic scattering component from the n-^{12}C component of the detector lineshape measured at E_n = 63 MeV. For the n-p capture measurements, neutron time of flight was used to select neutron energies of 63 MeV.

The measurements which are the subject of the present work, formed part of the calibration runs of the n-p capture experiment. Time of flight was used to study the wider incident neutron energy range of 15-63 MeV. These data provided detailed information on a range of related topics related to the neutron induced interactions in the NE213 scintillator as outlined below.

(i) The response functions (lineshapes) of the NE213 detector were measured for monoenergetic neutrons in the energy range 15-63 MeV. These lineshapes were separated offline into components for events releasing charged particles, identified by pulse shape discrimination, to be protons, deuterons and alphas, respectively. Particular attention was given to analysing the lineshape measured at E_n = 63 MeV, the neutron energy for the radiative capture measurements.

(ii) The charged particle components of the lineshapes, displayed features which could be identified with particular energy for the charged particle concerned. This allowed the response (light output) of the scintillator to be determined simultaneously for protons, deuterons and alphas as a function of charged particle energy, from the data obtained under the same experimental conditions.

(iii) Total cross sections for neutron induced proton, deuteron and alpha production from ^{12}C were measured as a function of incident neutron energy, by comparing the yields for each type of charged particle with the yield for

protons recoiling from n-p elastic scatters. The simultaneous presence of these $^{1}H(n,n)^{1}H$ events in the scintillator provided a reference for establishing an absolute scale for the n-^{12}C reaction cross section measurements. A Monte Carlo code was used to correct the measurements for the effect of protons escaping from the detector.

(iv) The efficiency of the scintillator for detection via n-p elastic scattering only, was calculated assuming the $^{1}H(n,n)^{1}H$ total cross section in the literature. The ratio of the number of n-p elastic scattering events to the number of n-^{12}C interaction events detected above the low detection threshold, was measured as a function of neutron energy. The efficiency of the scintillator for detecting n-^{12}C interactions, and thus the efficiency for detecting all neutron induced interactions, was determined with reference to the calculated efficiency for n-p elastic scattering.

The following chapter describes the experimental details and the method of data acquisition of this work.

CHAPTER 2

THE EXPERIMENT

A neutron beam obtained via the $^{7}Li(p,n)^{7}Be$ reaction was collimated onto an NE213 cell which provided 4π detection of the neutron-induced charged particle products from the interactions in the scintillator. The signals of the different charged particles arising from neutron induced events in the scintillator were separated by pulse shape discrimination. Neutron time-of-flight was used to investigate an incident energy range of 15-63 MeV in a single run, with a timing resolution (FWHM) of better than 2 ns.

2.1 EXPERIMENTAL DETAILS

(a) NEUTRON PRODUCTION

Figure 2.1 shows the experimental configuration for the measurements. A pulsed 66 MeV proton beam from the separated-sector cyclotron at the

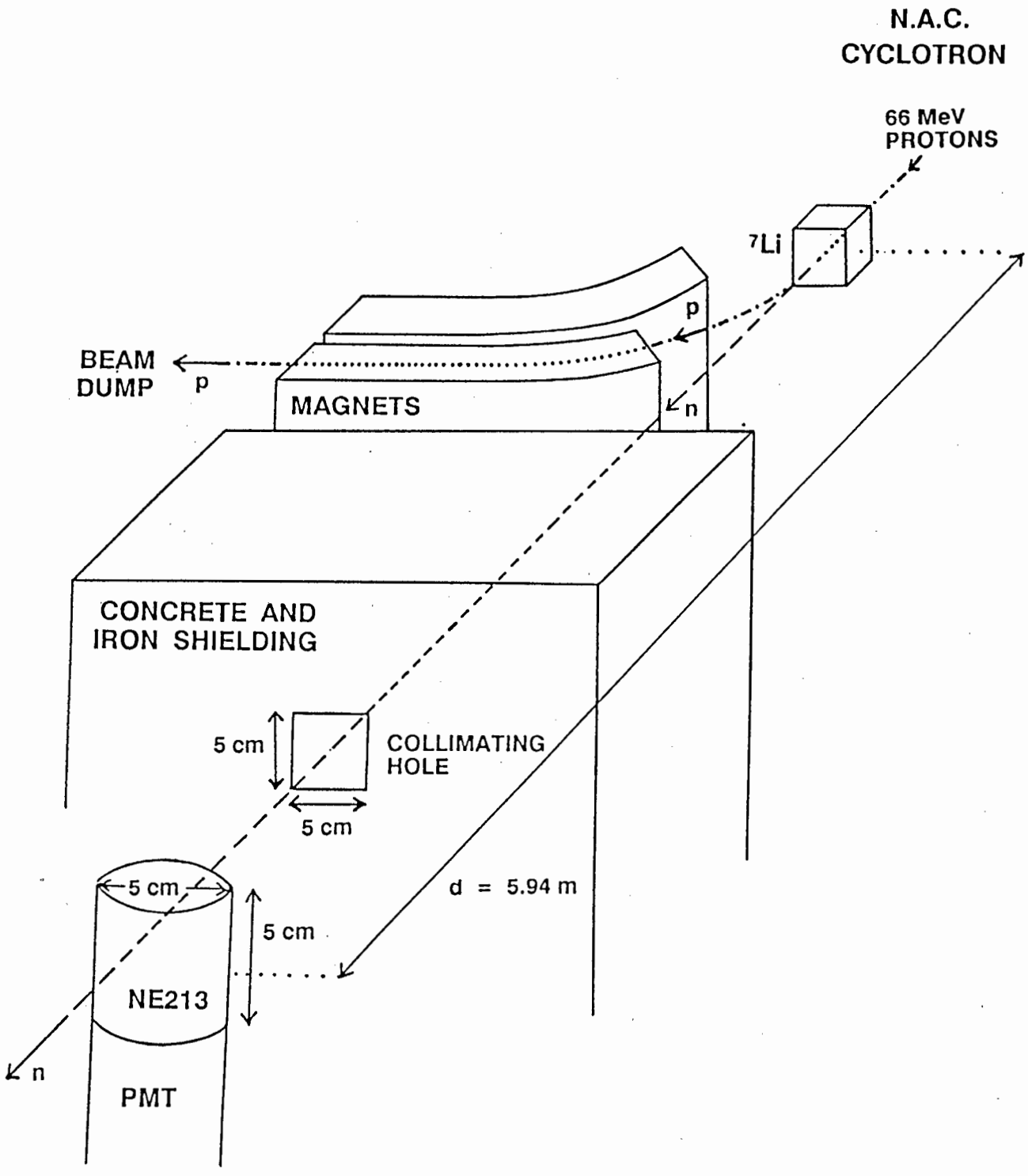

Figure 2.1 A sketch of the experimental geometry. Neutrons released from the $^{7}Li(p,n)^{7}Be$ reaction were collimated in the forward direction to form a beam which illuminated the 5 cm (diameter) by 5 cm cylinder of NE213 liquid scintillator.

National Accelerator Centre (NAC) was directed through a 4.5 mm thick metallic lithium target. Neutrons were produced via the $^{7}Li(p,n)^{7}Be$ reaction and the neutron energies were measured and selected by neutron time-of-flight. The neutron flight path was 5.9 m. Every fifth proton beam pulse from the injector cyclotron (period 61.07 ns) was selected to give the desired period of 305.35 ns between each burst of neutrons.

Concrete and iron shielding surrounded the natural lithium target in the neutron production area. A 5 cm by 5 cm aperture collimated the neutrons from the $^{7}Li(p,n)^{7}Be$ reaction in the forward direction. The transmitted protons were swept away by a system of magnets into a beam dump including a Faraday cup. The proton beam current was confined to a range 270-300 nA during running to avoid dead time and pileup in the electronics.

(b) NEUTRON DETECTION

Neutrons were detected by a cylindrical (5 cm high x 5 cm diameter) single-window BA1 cell of NE213 liquid scintillator. The BA1 cell consists of a thin aluminium casing surrounding a capsule (with a single glass wondow) around which is wound a thin polythene expansion tube. The primary component of NE213 liquid scintillator is xylene ($C_6H_4(CH_3)_2$), to which naphthalene ($C_{10}H_8$) is added to reduce quenching effects in the scintillator and to enhance the slow component of light emission to improve the pulse shape discrimination capability (Bu69). See table II for a list of physical characteristics of this scintillator.

The window of the BA1 cell was optically coupled to an RCA 8850 photomultiplier (RCA) using silicon jelly. The detector was mounted vertically on with its axis perpendicular to the incident neutron beam. This orientation of the detector was dictated by the requirements for the n-p capture measurements. Subsequent measurements, still awaiting analysis, have been made with the detector aligned with its axis facing the beam. The distance

Light output (relative to anthracene)	78%
Density	0.874 g/cm^3
H/C (atomic ratio)	1.212
No. of H atoms per cm^3	4.82×10^{22}
No. of C atoms per cm^3	3.98×10^{22}
Electron density (electrons per cm^3)	2.87×10^{23}
Wavelength of maximum emission	425 nm
Refractive index, n_o	1.505
Refractive index at 425 nm	1.530
Decay time (fast component)	3.2 ns

Table II Physical characteristics of NE213 liquid scintillator (NE).

from the centre of the lithium target to the centre of the scintillator was measured to be 5.940 ± 0.005 m.

(c) BEAM PROFILE MEASUREMENTS

The neutron beam profile was measured at the detector site using a small (10 mm diameter x 21 mm) cylindrical organic crystal with its axis aligned parallel to the beam. A horizontal scan was made across the neutron beam, recording the number of detected events detected in the crystal for a fixed integrated proton charge. Figure 2.2 shows the measured horizontal beam profile as a function of distance from the position at which the NE213 detector was afterwards centred. As the beam width (~7 cm) was found to be greater than the diameter of the NE213 cell, it could be deduced that the whole of the scintillator was being uniformly illuminated by the beam.

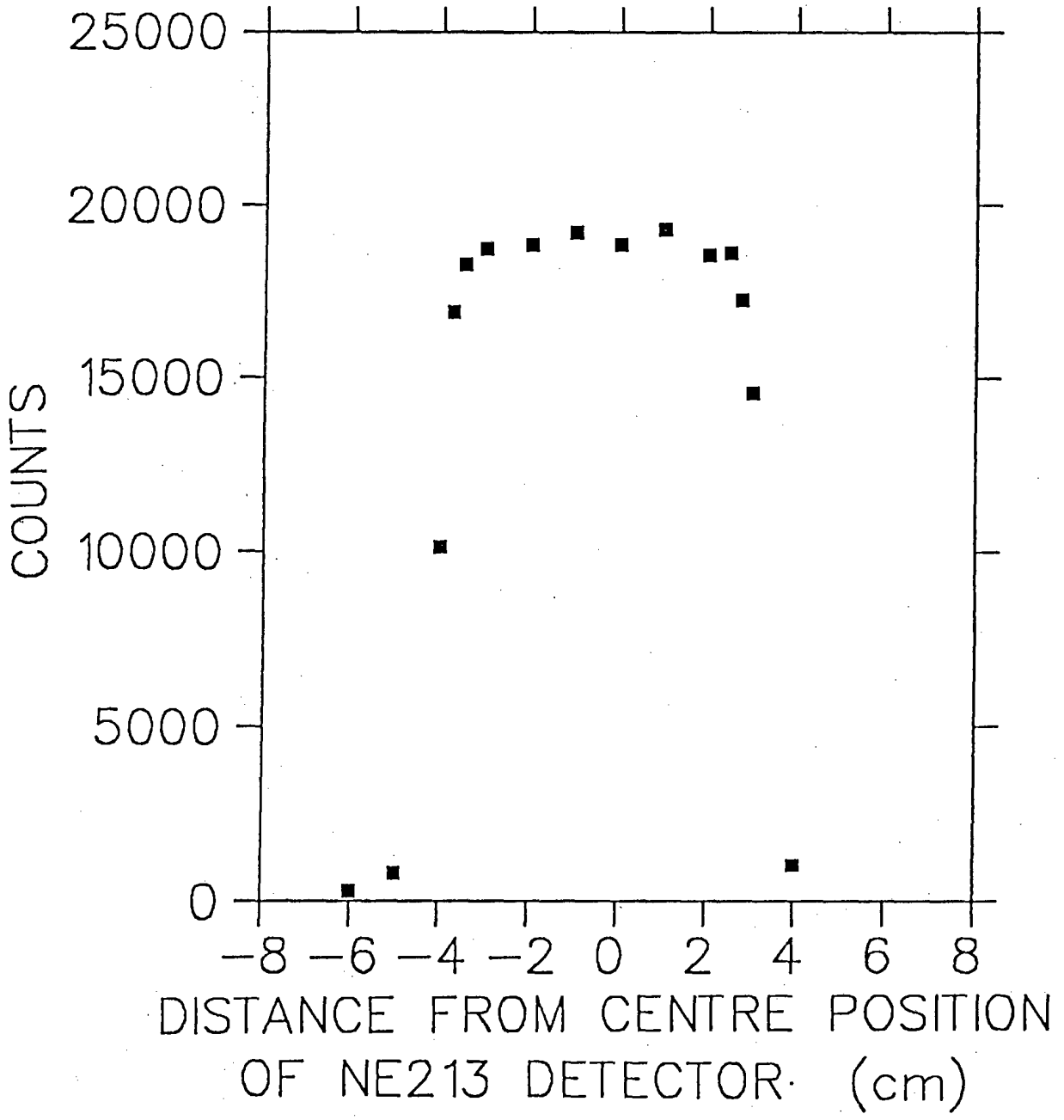

Figure 2.2 Neutron beam profile measured at the position of the NE213 detector by scanning a 1.0 cm (diameter) by 2.1 cm cylindrical organic crystal horizontally across the beam diameter. Shown are counts measured for a fixed number of protons incident on the lithium target as a function of distance from the position at which the centre of the NE213 detector was afterwards situated.

2.2 ELECTRONICS

(a) DATA ACQUISITION SYSTEM

Three parameters were recorded for each event, namely L, the scintillation pulse height , F, the integral over the fast component of the scintillation pulse, and T_n , the neutron time of flight, which was measured relative to a fixed phase point in the cyclotron r.f. cycle. Figure 2.3 shows a schematic diagram of the main components of the electronic configuration. A more detailed circuit diagram is included in figure 2.4.

The output pulse from the anode of the photomultiplier tube was fed into a LINK Model 5010 pulse shape discrimination unit which generated the L and F signals. The pulse height, L, was generated in the LINK by integrating the scintillation pulse over a period of 500 ns, while the F signal was generated by integrating over a period of 30 ns. In order to produce the F output, the LINK circuitry was modified as described by Smit (Sm86).

The LINK also generated a timing pulse, T, which was used to start the time-to-amplitude converter (TAC) for measuring the neutron time of flight, T_n. The stop pulse for the TAC was provided by the beam pulse. An event was passed by the coincidence unit whenever there was simultaneously a pulse on the TAC output and the PSD gate from the LINK, as shown in figure 2.3. The three parameters L, F and T_n were fed through the ADCs into a VAX computer where they were recorded as an event on magnetic tape using the data acquisition code, *XSYS*. All phases of the data acquisition were monitored on a system of displays to detect any electronic drifts.

The pulse height scale was calibrated by recording the pulse height spectrum for the 4.44 MeV γ-ray from an AmBe source (see figure 4.2(a)) under the same experimental conditions as the beam measurements.

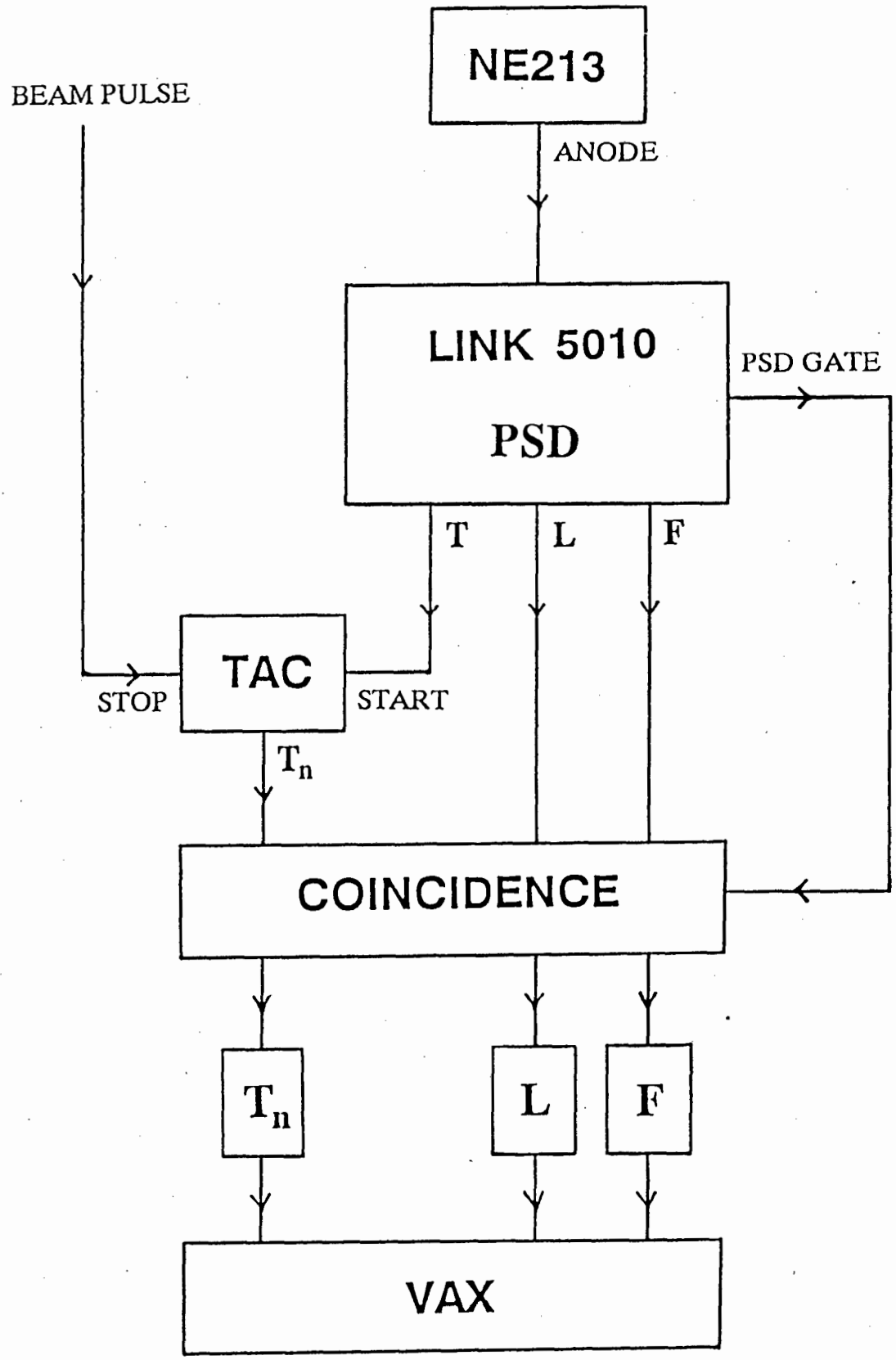

Figure 2.3 Schematic diagram of the main components of the electronic configuration used for the pulse processing. The full circuit is shown in figure 2.4.

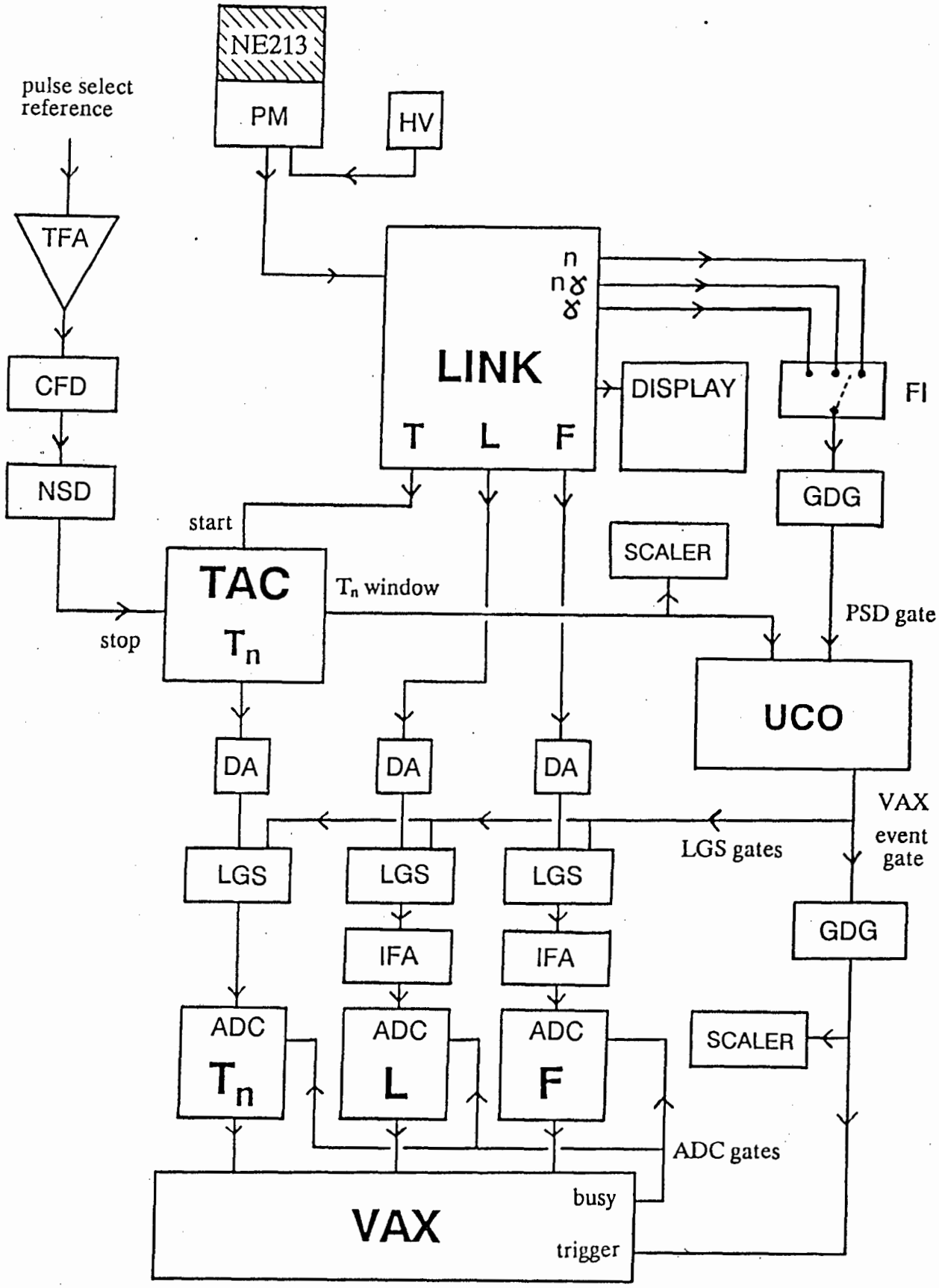

Figure 2.4 *The full electronic circuit used for the pulse processing.*

(b) PHOTOMULTIPLIER BASE CIRCUIT

The photomultiplier voltage divider circuit (figure 2.5(a) recommended in the LINK manual (LINK) was used in this work. For reasons outlined below, it has since been replaced by the circuit recommended in the RCA photomultiplier catalogue (RCA), shown in figure 2.5(b).

The purpose of the 150V Zener diodes shown in figure 2.5(a) is twofold. Firstly they maintain a constant electron collection efficiency between the cathode and first dynode in the chain to provide good energy resolution of the scintillation pulses, independent of the voltage across the circuit. The Zeners at the lower end of the dynode chain maintain a constant potential difference across the last three dynodes and the anode. The current, I_d, through the potential divider must exceed 0.5 mA to ensure stable operation of the Zeners. At this current the voltage across the dynodes connected by the 100K resistors is 50 V, which is sufficient to avoid space charge non-linearities for small pulses (e.g. for protons of energy < 15 MeV). In present work in which charged particles of energies less than 66 MeV were detected, the photomultiplier voltage was set at - 1770 V (I_d = 0.6 mA). However, it was recognised afterwards (see section 4.1(b)) that the photomultiplier had not provided linear current amplification under these operating conditions and it may be concluded that this voltage divider circuit is only suitable for work at E_n < 15 MeV.

2.3 THE NEUTRON BEAM

Figure 2.6 shows the neutron time-of-flight spectrum measured in this work. The time of flight channel scale was calibrated to a nanosecond scale by the standard method of operating the TAC in self-stopped mode with two different delays respectively between the start and stop pulses. The spectrum shift produced by standard 100 and 150 ns delay boxes was measured. A time

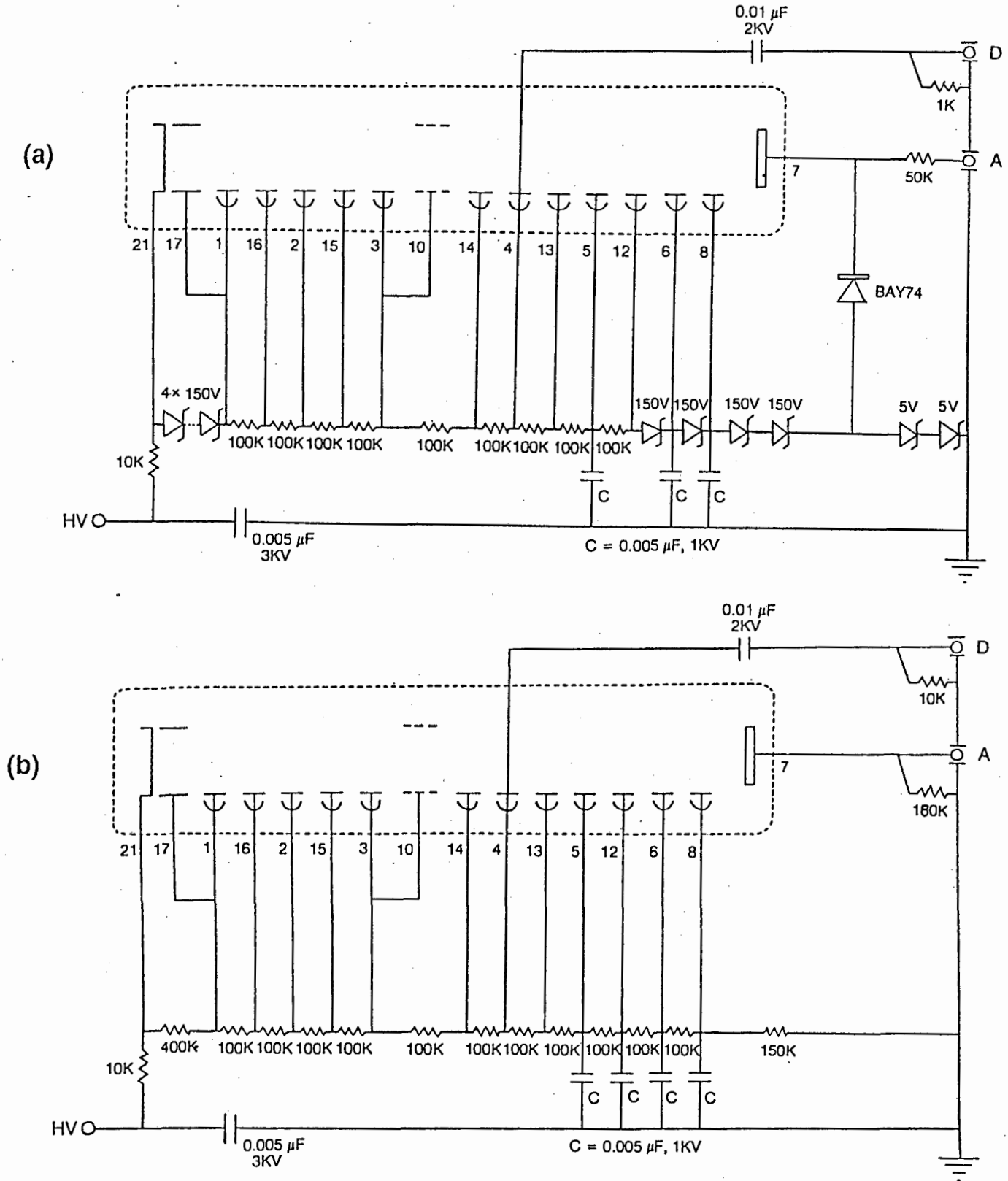

Figure 2.5 *(a) (above) Photomultiplier voltage divider used in this work* (LINK).

(b) (below) The standard RCA circuit which is now being used in current work (RCA).

calibration of 8.39 ± 0.01 channels/ns was then calculated for this work and the linearity of the TAC was also verified. Also shown in figure 2.6 is a neutron energy scale which runs in the opposite direction to the time of flight scale. This transformation from neutron time of flight to neutron energy is described in section 2.3(b).

(a) THE TIME OF FLIGHT SPECTRUM

It can be seen in figure 2.6 that the highest energy neutrons produced fall within a sharp high energy peak in the time of flight spectrum. This peak arises principally from the transitions to the unresolved ground and first excited states of ^{7}Be in the ^{7}Li(p,n)^{7}Be reaction. The rest of the spectrum consists of a broad, lower energy, Maxwellian-like tail. These neutrons arise from excitation of higher states in ^{7}Be or from breakup reactions leading to three or more particles in the final state. Some neutrons also lose energy by multiple scattering before leaving the lithium target.

In addition to the inherent timing resolution of the system, the width of the ^{7}Li(p,n)^{7}Be$_{gs}$ neutron peak may be attributed to the energy losses of the incident protons in the lithium target prior to neutron production. This energy loss ranges from zero up to some maximum value which depends on both the thickness of the lithium target and the incident proton energy, with all intermediate values equally possible (Au72). The energy of the protons emerging from the lithium target was calculated to be 64 MeV. A linear proton energy loss was assumed across the lithium target. Then prior to neutron production in the target, the incident protons were regarded as having a mean energy of halfway between 66 MeV and 64 MeV, i.e. 65 MeV. Using the Q-value for the ^{7}Li(p,n)^{7}Be reaction of -1.644 MeV (Aj84), the mean energy of the ^{7}Li(p,n)^{7}Be$_{gs}$ peak was then calculated from the standard reaction kinematic equations (Appendix A) to be 63.4 ± 1 MeV.

Figure 2.7(a) shows the high energy neutron peak fitted by a standard Gaussian function. The full width at half maximum (FWHM) was measured

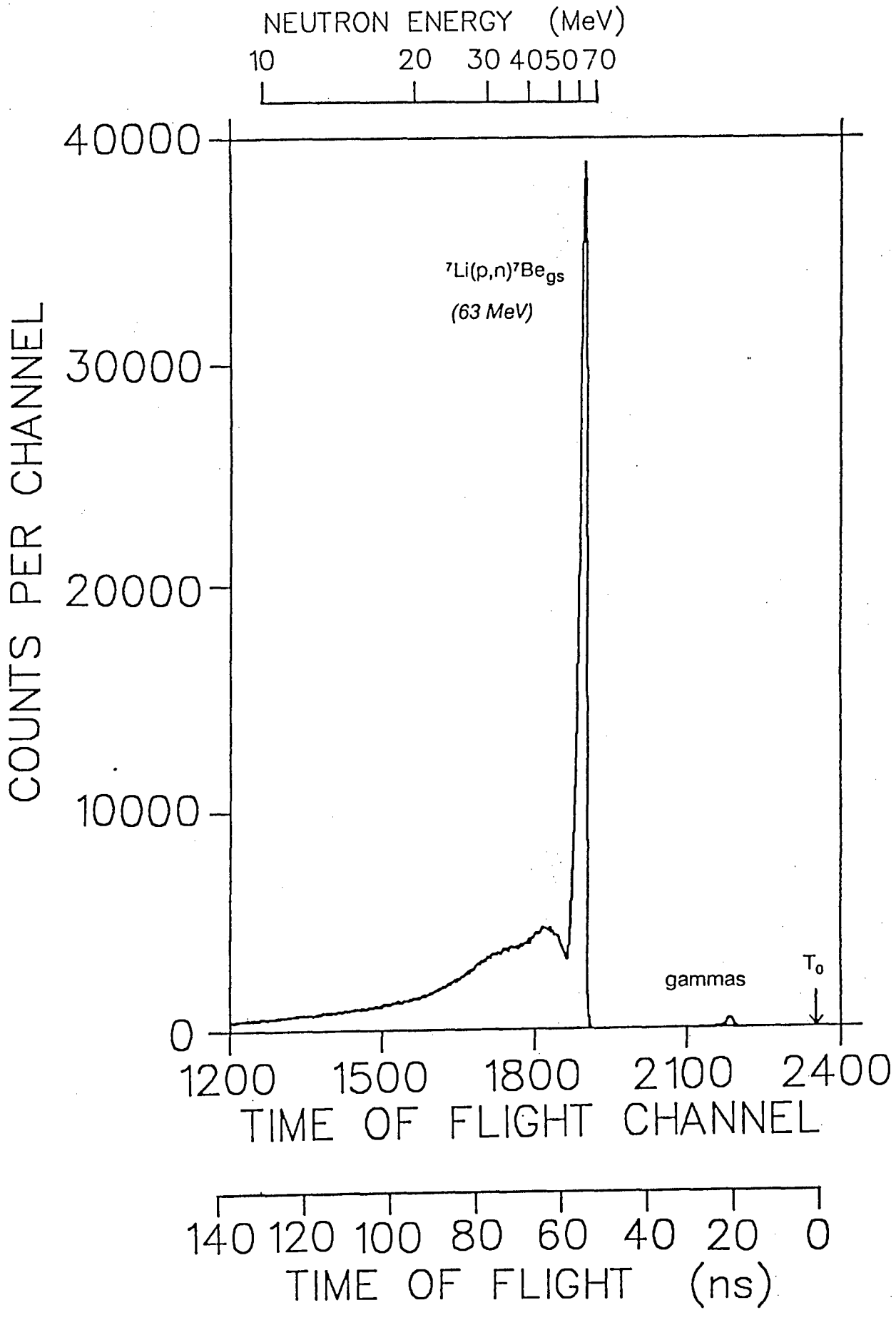

Figure 2.6 Time of flight spectrum measured by a 5 cm (diameter) by 5 cm cylindrical NE213 liquid scintillator placed 5.9 m from a ^{7}Li target which was bombarded by 66 MeV protons. The intense peak corresponds to neutrons released in the ground state transition of the $^{7}Li(p,n)^{7}Be$ reaction. A small peak arising from the detection of low energy gammas released in (p,n) reactions in the ^{7}Li target is labelled.

to be 2.2 ns which is a measure of the uncertainty in the energy of the neutrons falling within this peak.

There is also a small gamma peak to the right of the neutron peak at 19.8 ns in figure 2.6. This peak arises from the detection of the low energy gammas emitted in proton-induced reactions in the lithium target, and not excluded by the pulse shape discrimination. This peak is small, as a low pulse height threshold was set at about E_n = 5 MeV, which rejected the majority of signals from these low energy gammas. However, those gamma rays which were detected reached the NE213 detector at a time defined by the velocity of light, c, and the flight path, d. Figure 2.7(b) shows this peak fitted with a standard Gaussian distribution. The full width at half maximum of the peak of 1.7 ns is then a measure of the intrinsic timing resolution of the system. The additional width of the neutron peak (figure 2.7(a)) is attributed to the spread of the proton energy in the lithium target and a small contribution from the unresolved first excited state of ^{7}Be. These factors contribute of the order of 1.5 ns to the overall uncertainty in energy of the neutrons falling within the ^{7}Li(p,n)^{7}Be$_{gs}$ peak, as the quadratic summation of this uncertainty (1.5 ns) with the measured intrinsic resolution measured from the gamma peak (1.7 ns) yields the measured FWHM of the neutron peak (2.2 ns).

(b) TIME OF FLIGHT TO NEUTRON ENERGY CALIBRATION

With reference to figure 2.6, there exists a "time zero" channel, T_0, corresponding to the position of zero time-of-flight. The position of T_0 was calculated to be at T_n-channel = 2350 from:

$$T_0 = T_\gamma - (d/c)(1/F) \qquad (2.1)$$

where: T_γ : ADC channel at the centre of the γ-peak (T_n-channel 2184)

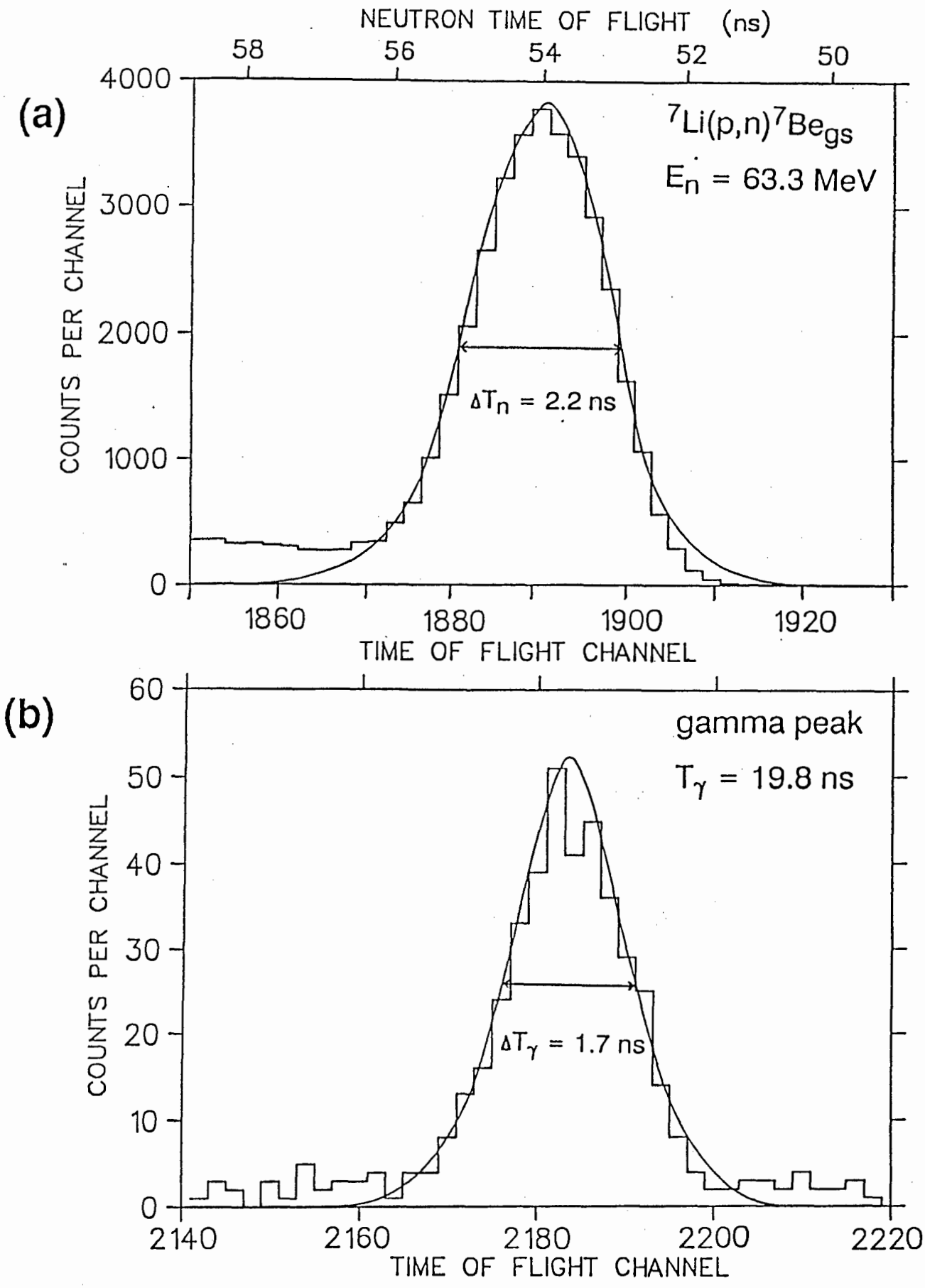

Figure 2.7 *(a) (above) A Gaussian fit to the $^7Li(p,n)^7Be_{gs}$ peak in the neutron time of flight spectrum (figure 2.1).*

(b) (below) A Gaussian fit to the gamma peak in the spectrum. The width of this peak of 1.7 ns indicates the intrinsic time of flight resolution of the system.

c : velocity of light = 0.300 m/ns

d : distance from the centre of the ^{7}Li sample to the centre of the NE213 cell = 5.940 ± 0.005 m

F : 8.39 ± 0.01 channels/ns

Then for any neutron time-of-flight, T_n (expressed in channels), a corresponding neutron energy, E_n, could be calculated using:

$$E_n = \left\{ \frac{72.3 \, . \, d}{(T_n - T_0) \, . \, F} \right\} 2 \qquad (2.2)$$

where:

T_0 : "time zero" ADC channel

T_n : neutron time-of-flight ADC channel

E_n : neutron energy in MeV

d, F : as for equation 2.1 above

72.3 : scaling factor

The uncertainty in the neutron energy measurement depends on the time of flight resolution of the system, ΔT_γ, and the uncertainty in the flight path, Δd, as well as on the spread in the mean proton energy in the lithium sample. The FWHM of the gamma peak, which is a measure of the intrinsic timing resolution of the system, sets the minimum energy uncertainty obtainable for neutrons selected by time of flight, i.e. at energies less than the 63 MeV peak. For measurements at E_n = 63 MeV, selecting the ^{7}Li(p,n)^{7}Be$_{gs}$ peak which heavily dominates the total neutron yield, the energy resolution is defined by the proton energy spread in the lithium target. The FWHM of the ^{7}Li(p,n)^{7}Be$_{gs}$ peak is a measure of this uncertainty, as discussed above.

Since $\Delta T_\gamma / T_n \gg \Delta d/d$, the latter was taken as negligable and the uncertainty, ΔE_n, in any neutron energy less than the 63 MeV peak was calculated in the standard way by:

$$\Delta E_n = 0.028 \; (\Delta T_\gamma / d) \; E_n^{3/2} \qquad (2.3)$$

where:

ΔT_γ	:	width of gamma peak (1.7 ns)
d	:	as for equation 2.1, above
E_n	:	neutron energy in MeV
0.028	:	scaling factor

Figure 2.8 shows ΔE_n as a function of E_n for the incident neutron energies considered in this work, calculated from equation 2.3 for E_n < 63 MeV, and determined from the measured width of the $^7Li(p,n)^7Be_{gs}$ peak at E_n = 63 MeV. Consequently, specific neutron energies could then selected off-line by setting the appropriate time window on the neutron time of flight spectrum. Time window widths of between 1.6 ns and 1.8 ns were chosen to be of the order of the intrinsic timing resolution of the system (1.7 ns).

The following chapter describes how the measured data were reduced to produce response functions for this detector at different incident neutron energies in the range 15-63 MeV, selected by time of flight. These lineshapes were then unfolded into components associated with the emission of different charged particles, identified by pulse shape discrimination to be protons, deuterons and alphas.

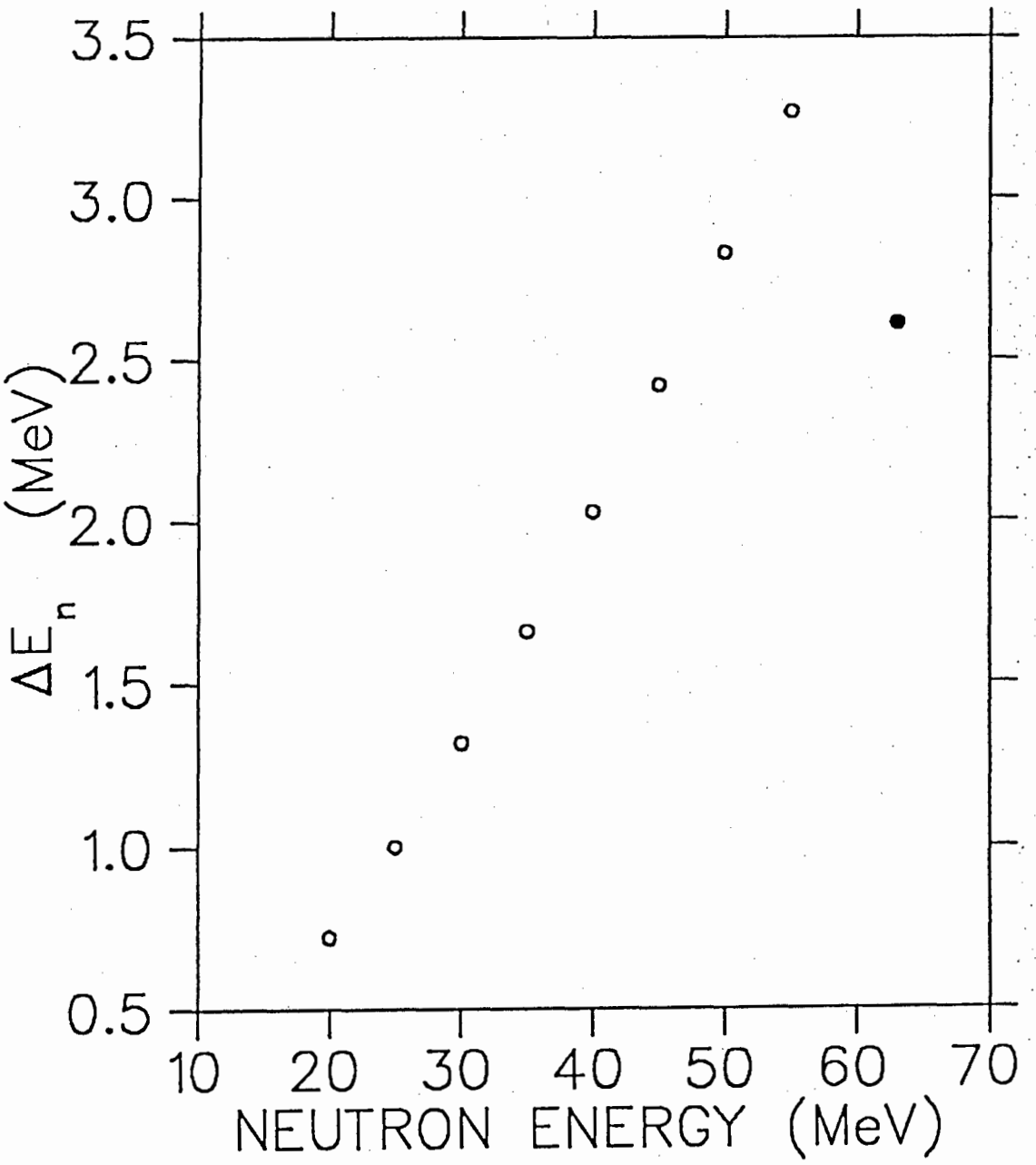

Figure 2.8 Energy resolution, ΔE_n, as a function of the incident neutron energies considered in this work. The values shown for E_n < 63 MeV (o) are related to the width of the gamma peak and were calculated using equation 2.3; while the value at E_n = 63 MeV (●) is determined from the width of the $^7Li(p,n)^7Be_{gs}$ peak.

CHAPTER 3

DATA REDUCTION

Chapter 2 described the experimental details of this work and the recording onto magnetic tape of three parameters, namely, L, F, and T_n for each event. This chapter decribes how the data were reduced to produce response functions of the NE213 detector to neutrons at different neutron energies. Furthermore, two methods of separation of these lineshapes into components associated with protons, deuterons and alphas are described.

3.1 PARTICLE DISCRIMINATION.

A pulse shape discrimination parameter, S, indicating the scintillation **pulse shape** and hence the type of the charged particle causing the scintillation, is determined from the fast and intregrated pulse parameters, F and L respectively, by:

$$S = L - kF + C \qquad (3.1)$$

where k and C are arbitrary constants chosen and introduced into the software to suit the data. The value k determines the angles of the loci in the L-S distribution (see below) and the value of C determines the position of these loci along the S-axis.

The signal from each type of ionizing particle detected has a particular set of L and S values, that when plotted on a plane, places it on a unique locus, dependent on the type and energy of the particle. Shown in figure 3.1 is a perspective plot of counts versus L and S measured at E_n = 63 MeV. The event signals corresponding to the detection of different ionizing particles are seen to contribute to the formation of well-defined ridges which are resolved on the L-S plane. These ridges are clearly distinguished at higher L, however, with decreasing pulse height, this separation diminishes due to poorer photomultiplier statistics.

The ridges as labelled in figure 3.1 are associated with neutron detection via the release in the scintillator of protons (p), deuterons (d), tritons (t), ^{3}He nuclei (h) and alpha particles (a) respectively. A locus formed by escaping protons (e) is also identified. Section 3.2 describes how the events forming these ridges were separated from each other to obtain pulse height spectra for the different ionizing particles.

Figure 3.2(a) is an event density spectrum of L (from which charged particle energy may be determined) versus T_n (associated with incident neutron energy), measured for all incident neutron energies, together with a perspective plot (b) of counts versus L and T_n for the same data. The projection of this entire matrix onto the T_n-axis yields the neutron time-of-flight spectrum (figure 2.1). Projection of the sharp ridge labelled ^{7}Li(p,n)^{7}Be$_{gs}$ in figure 3.2 leads, for example, to the sharp peak at T_n = 54 ns in the time of flight spectrum (figure 2.6).

There are three other features in figure 3.2. The first is the curved edge marking the upper pulse height (energy) limit for protons recoiling from n-p

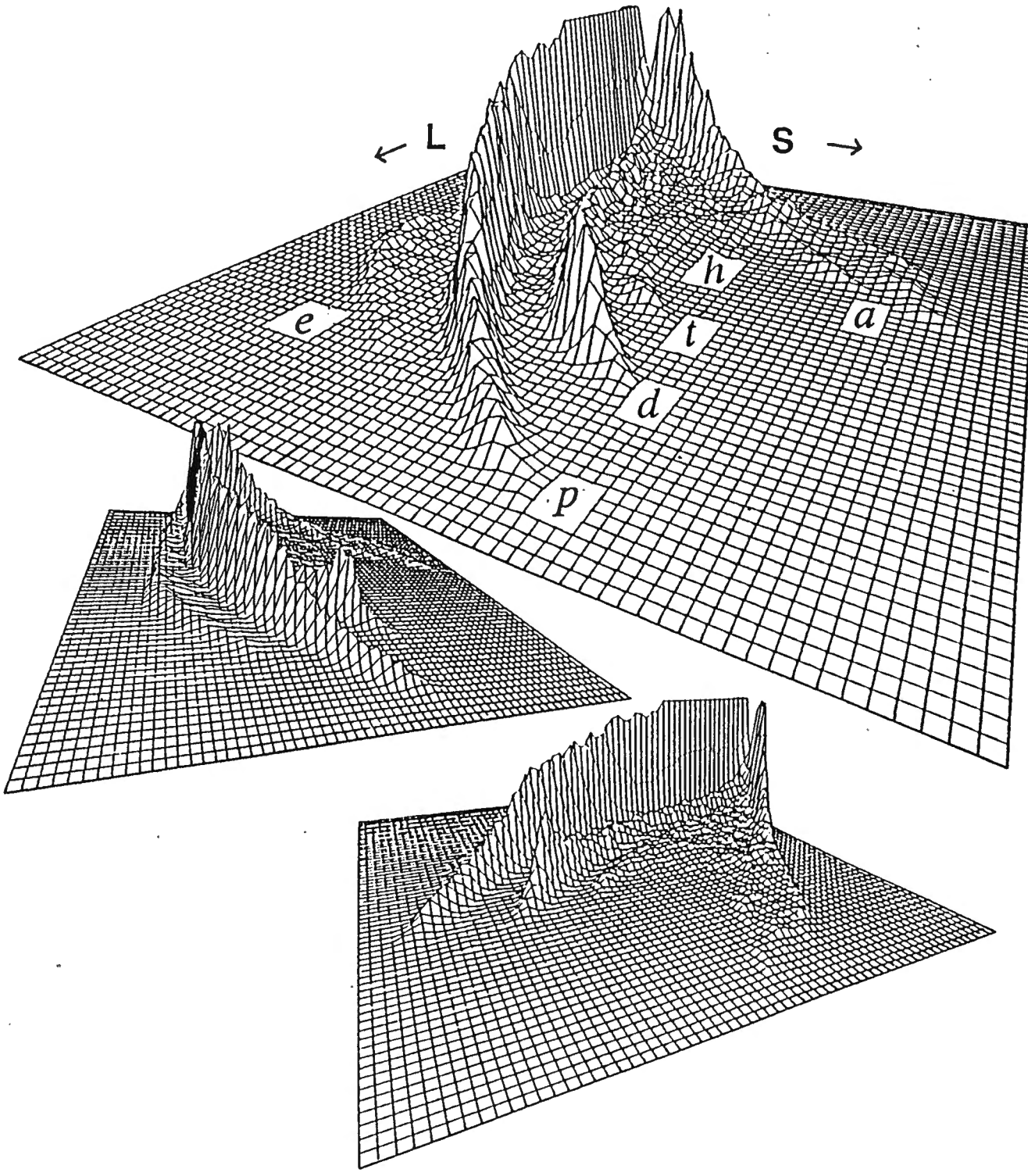

Figure 3.1 Perspective views of counts (vertical) as a function of pulse height, L , and pulse shape parameter, S , for events in an NE213 scintillator when exposed to 63 MeV neutrons. The loci associated with different charged particles are (p) *protons,* (d) *deuterons,* (t) *tritons,* (h) ^{3}*He nuclei and* (a) *alpha particles. Also identified is a locus* (e) *which arises from the detection of escaping protons i.e. protons which do not come to rest in the scintillator.*

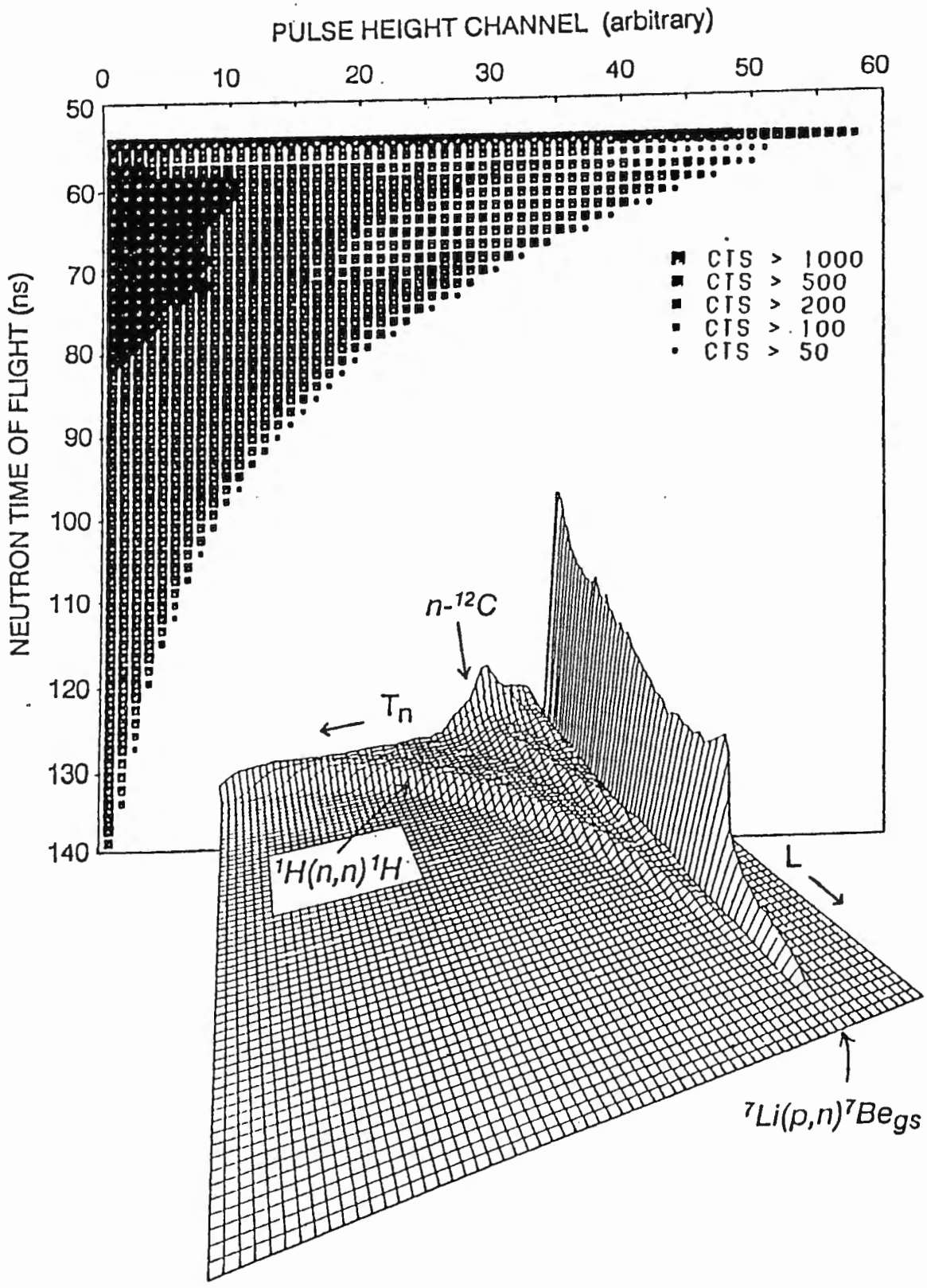

Figure 3.2 Event density (above) and perspective view (below) of counts (vertical) versus neutron time of flight, T_n, and pulse height, L, for events in an NE213 liquid scintillator when exposed to neutrons from a ^7Li target bombarded by 66 MeV protons. The sharp ridge on the right corresponds to the intense foward peak of 63 MeV neutrons from the $^7Li(p,n)^7Be$ reaction. Also labelled in the figure are the curved edge marking the upper pulse height limit for protons recoiling from $^1H(n,n)^1H$ events in the scintillator, and the events attributed to n-^{12}C reactions in the scintillator.

elastic scattering events. The proton energy associated with this edge will in turn be equal to the incident neutron energy.

There is a rise near the upper pulse height edge which is particularly noticeable at about T_n = 70 ns. This corresponds to the forward recoil peak predicted by the n-p elastic scattering differential cross section (figure 1.7), which has been enhanced by the effect of photomultiplier space charge saturation (see section 4.1(e). However, this rise is seen to disappear with further increase in neutron energy, due to the effect of escaping protons (refer to section 3.3).

The third feature in figure 3.2 is the increase in the proportion of the events due to n-^{12}C reactions with increasing neutron energy (T_n < 80 ns). It is this contribution that is often underestimated or even ignored in calculations of the neutron detection efficiency of organic detectors (as discussed in section 1.4).

The pulse height spectrum of the detector i.e. the detector response function (lineshape) for neutrons (as defined in section 1.4) may now be obtained for any incident neutron energy. After setting the appropriate T_n-window on the measured L-T_n spectrum, the events in the cut were projected onto the L-axis. For E_n < 63 MeV, time window widths of 1.6-1.8 ns (defined by the time of flight resolution of 1.7 ns) were set, centred at the particular neutron time of flight channel. This is related to an energy resolution ranging from 3.3 MeV (E_n = 55 MeV) to 0.7 MeV (E_n = 20 MeV) as shown in figure 2.8. Presented in figure 3.3 are the neutron lineshapes (pulse height distributions) measured at 10 different incident neutron energies spanning the energy range of this work. The two edges defining the upper pulse height limits for n-^{12}C interactions and n-p elastic scattering are clearly identified in the figure.

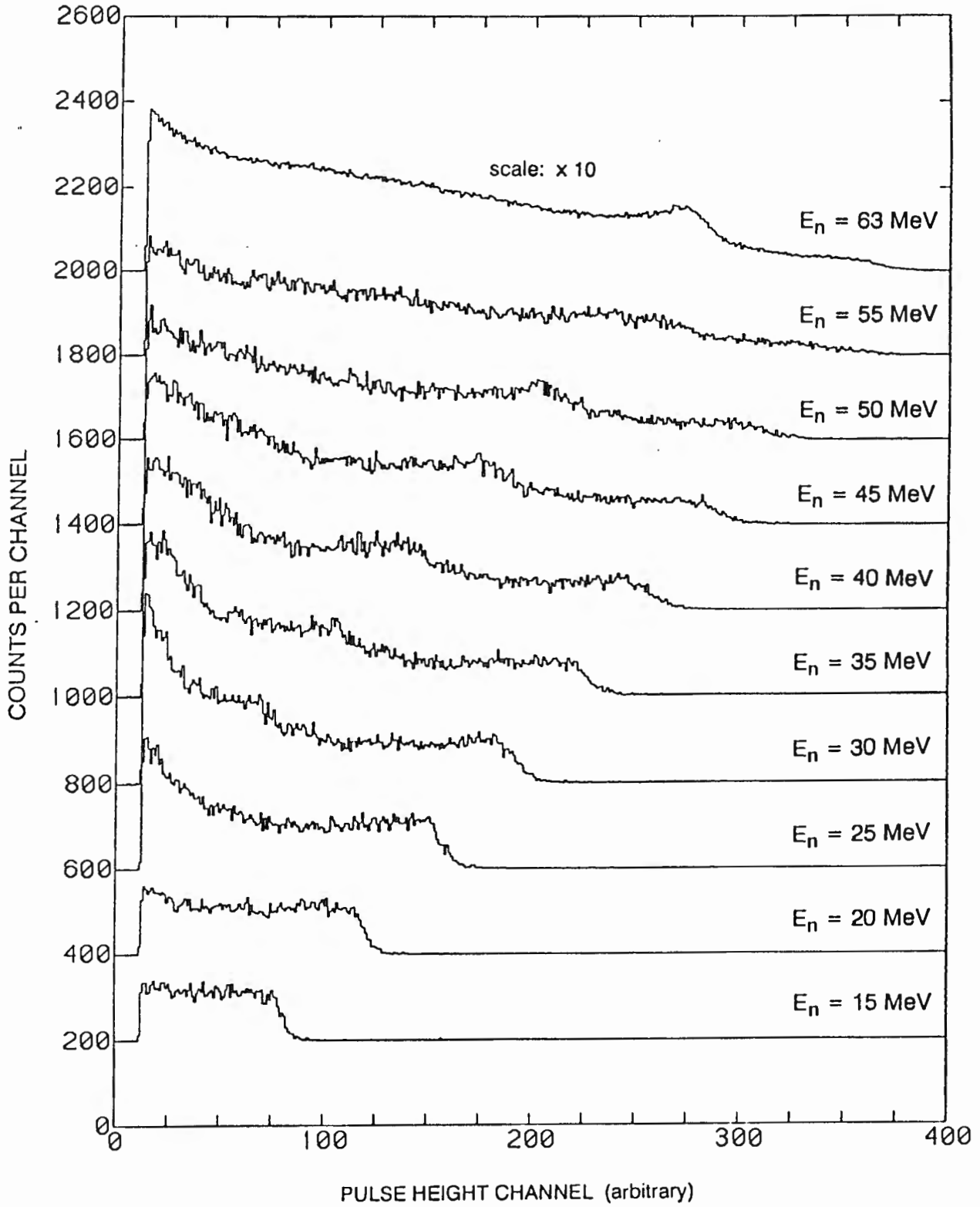

Figure 3.3 Neutron response functions for a 5 cm (diameter) by 5 cm cylinder of NE213, measured as a function of incident neutron energy. These spectra were obtained by setting neutron time of flight windows on the distribution shown in figure 3.2 and projecting the selected events onto the pulse height axis.

3.2 PARTICLE SEPARATION

Figure 3.4 shows the lineshape (pulse height spectrum) of the scintillator measured for incident neutrons of E_n = 63 MeV. This spectrum was obtained by setting a T_n-window on the $^7Li(p,n)^7Be_{gs}$ peak (figure 3.2) and projecting all the selected events onto the L-axis. Also shown in figure 3.4 are the components of this lineshape arising from the detection of protons, deuterons and alphas. These components were separated from the L-S spectrum (figure 3.1) by setting corridors to select the proton, deuteron and alpha loci respectively. This section describes (a) this method, and (b) a second more critical procedure of unfolding the neutron lineshapes .measured at E_n = 15-63 MeV.

(a) SEPARATION BY SOFTWARE CORRIDOR.

A computer program *GNU* - available in the Physics Department, University of Cape Town - allows the user to select and project regions from a two-parameter spectrum. A series of three of more points is specified to define each limit (upper and lower) of the region of interest on the matrix. The code then fits a smooth curve through these points and the events lying within the region may then be selected. *GNU* uses 12-bit resolution on both parameters when these regions are chosen i.e. operates on an effective resolution of 4096 x 4096 on the matrix.

Two-dimensional corridors were chosen to bound the ridges on the L-S plane corresponding to protons, deuterons and alpha particles. In order to determine accurately the points demarcating these corridors, at selected pulse heights, L, in figure 3.1, the events at these individual pulse heights were projected onto the S-axis, producing the spectra shown in figure 3.5. The "valleys" between the ridges could then be accurately discerned. Figure 3.6 shows the L-S two-parameter spectrum measured at E_n = 63 MeV (figure 3.1) plotted using the density plot option of the *PLOTDATA* graphics

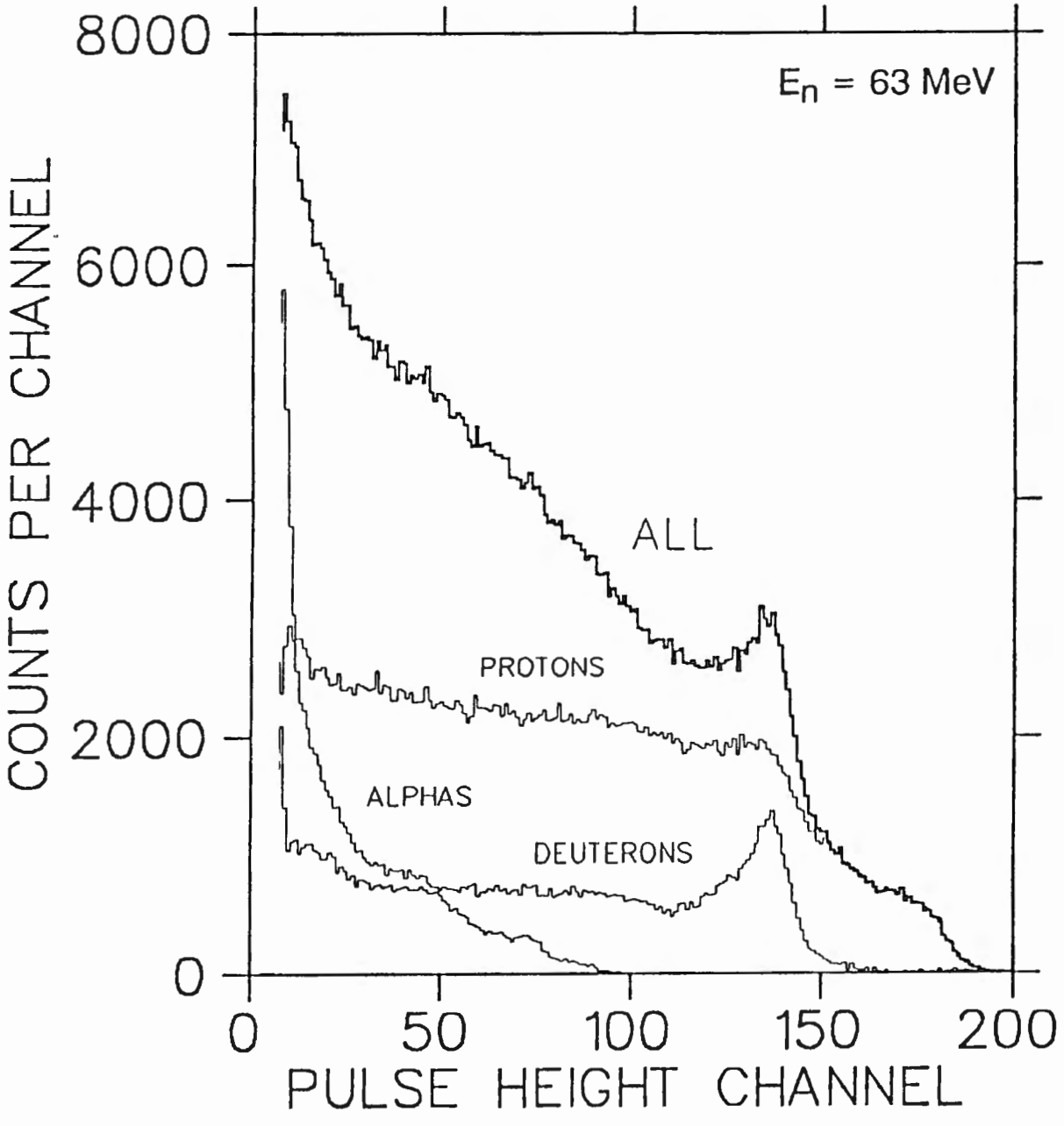

Figure 3.4 Response function (lineshape) of a 5 cm (diameter) by 5 cm NE213 liquid scintillator measured for incident neutrons of energy 63 MeV. The unfolding of the lineshape into its components (also shown) corresponding to protons, deuterons and alphas is described in the text.

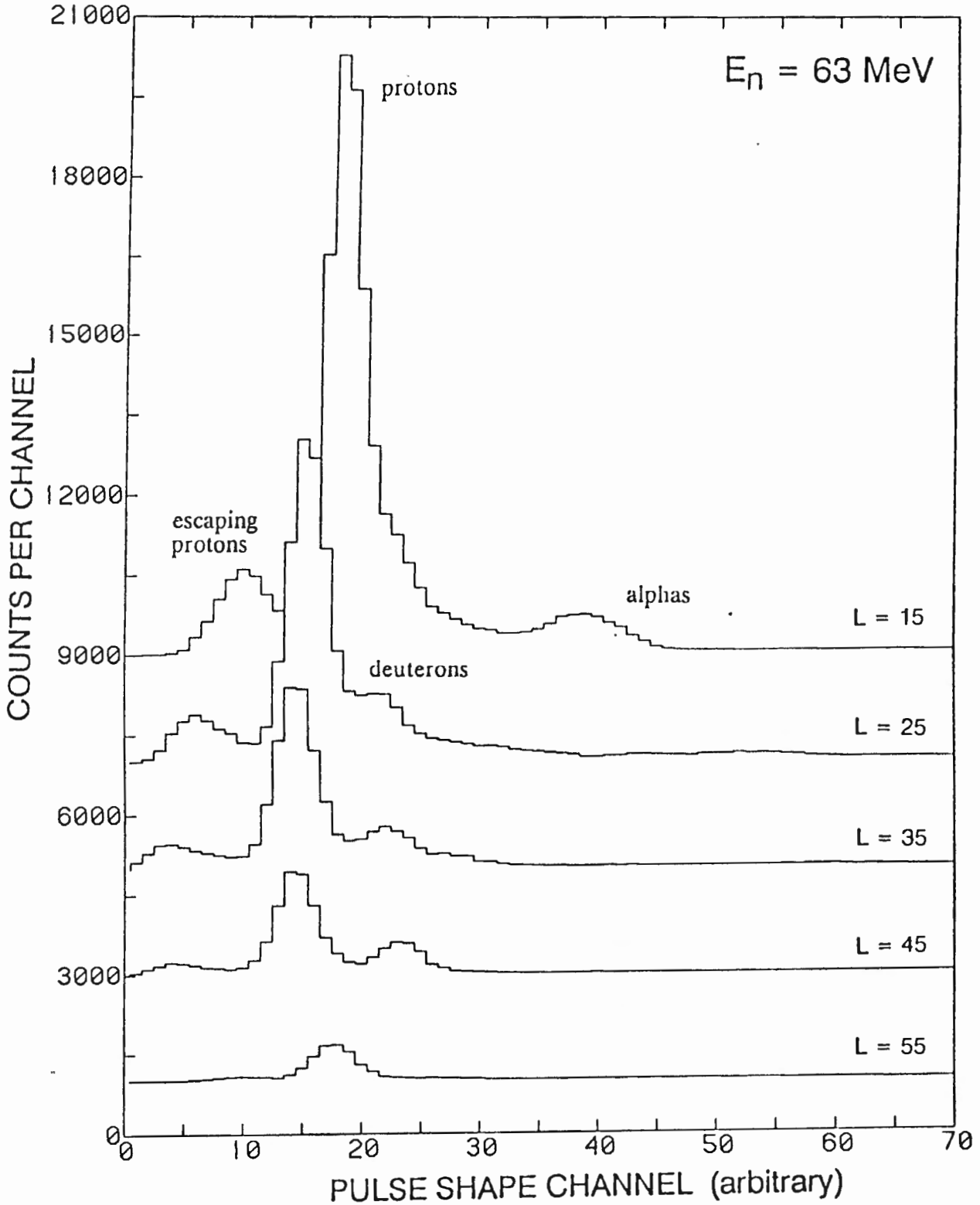

Figure 3.5 Counts versus pulse shape parameter, S , for a selection of pulse height (L) channels, measured at E_n = 63 MeV. The peaks associated with different charged particles are labelled.

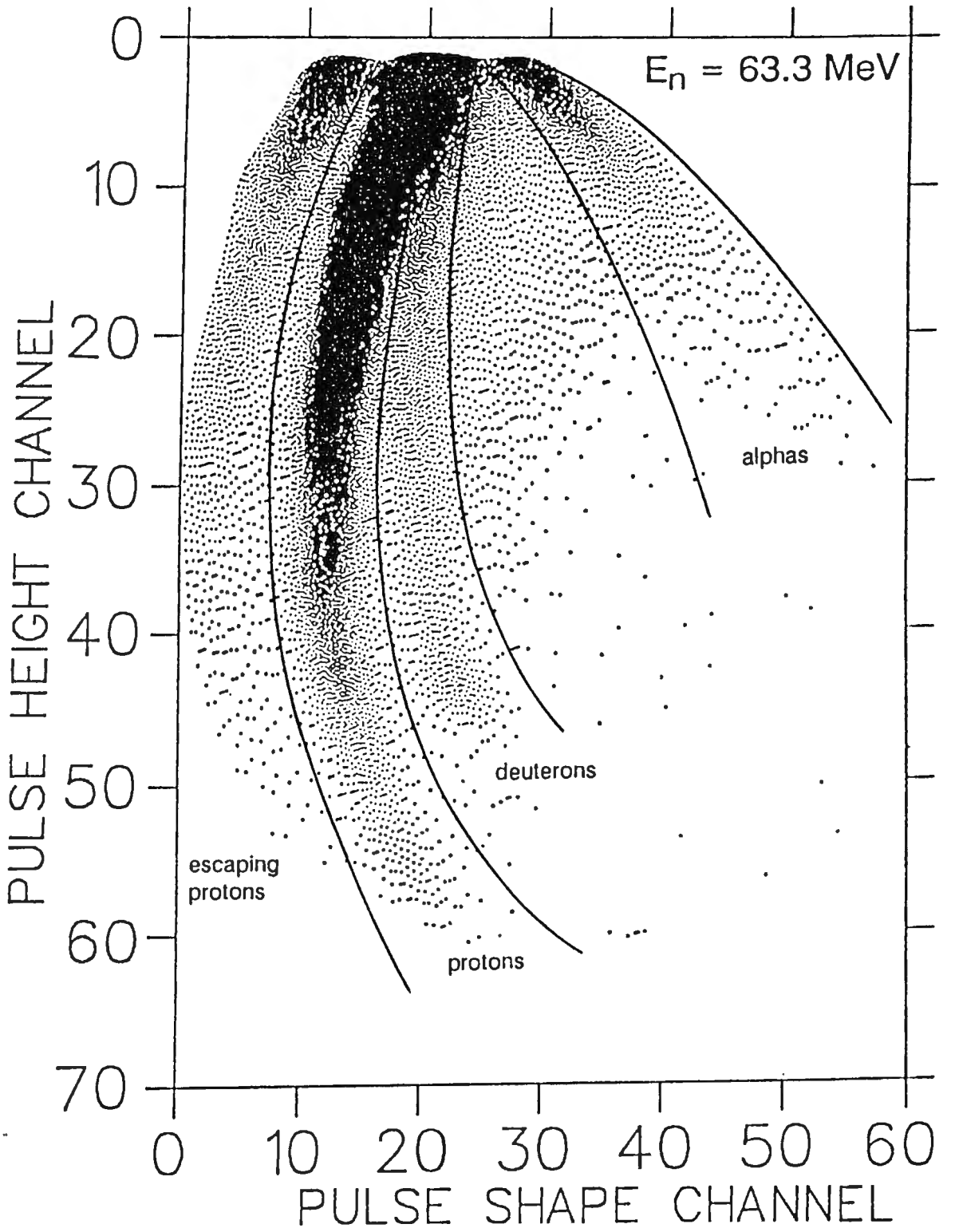

Figure 3.6 Event density plot (see text) of pulse height, L, versus pulse shape parameter, S, for all events detected at E_n = 63 MeV. Shown are the corridors that were set to select events which were identified as protons, deuterons and alphas by pulse shape discrimination.

package (Ch90) specified together with the "diffusion" qualifier. The figure illustrates the corridors that were chosen to demarcate the proton, deuteron and alpha loci.

From figures 3.5 and 3.6, it can be seen that the resolution of neighbouring loci via S is poorer at small pulse heights, L. The overlapping of the proton and deuteron peaks at low pulse height is particularly evident, for example, and may be understood in terms of photomultiplier statistics.

After the L-S corridors had been specified, the proton, deuteron and alpha signals could be selected at all incident neutron energies. Event density (a) and perspective (b) counts versus L and T_n spectra for protons and deuterons are shown in figures 3.7 and 3.8 respectively. The proton spectrum (figure 3.7) displays features similar to these as discussed for figure 3.2. A peak arising from the ground state transition of the reaction $^{12}C(n,d)^{11}B$ is identified in the deuteron spectrum (figure 3.8). Another feature in the spectrum is the 'breakthrough' of proton events into the deuteron corridor which is responsible for the 'ghost' of the proton distribution in the region above the deuteron ground state peak. Neutron multiple scattering in the scintillator enhances this breakthrough as explained in section 3.3.

Proton, deuteron and alpha pulse height spectra were now be selected at different incident neutron energies, E_n, by setting the appropriate T_n-window. These are presented as a function of incident neutron energy in figures 3.9, 3.10 and 3.11 respectively. The proton and deuteron spectra display the same features as described above for their L-T_n spectra. The alpha spectra are complex and include conributions from alphas released in both $^{12}C(n,\alpha)^{9}Be$ and $^{12}C(n,n')3\alpha$ reactions. The alpha pulse height spectrum measured at E_n = 63 MeV is discussed in detail in section 5.3.

(b) SEPARATION BY FITTING GAUSSIANS

The method of separation described in (a) above was successful in the intermediate and higher pulse height domain where the separation of the loci

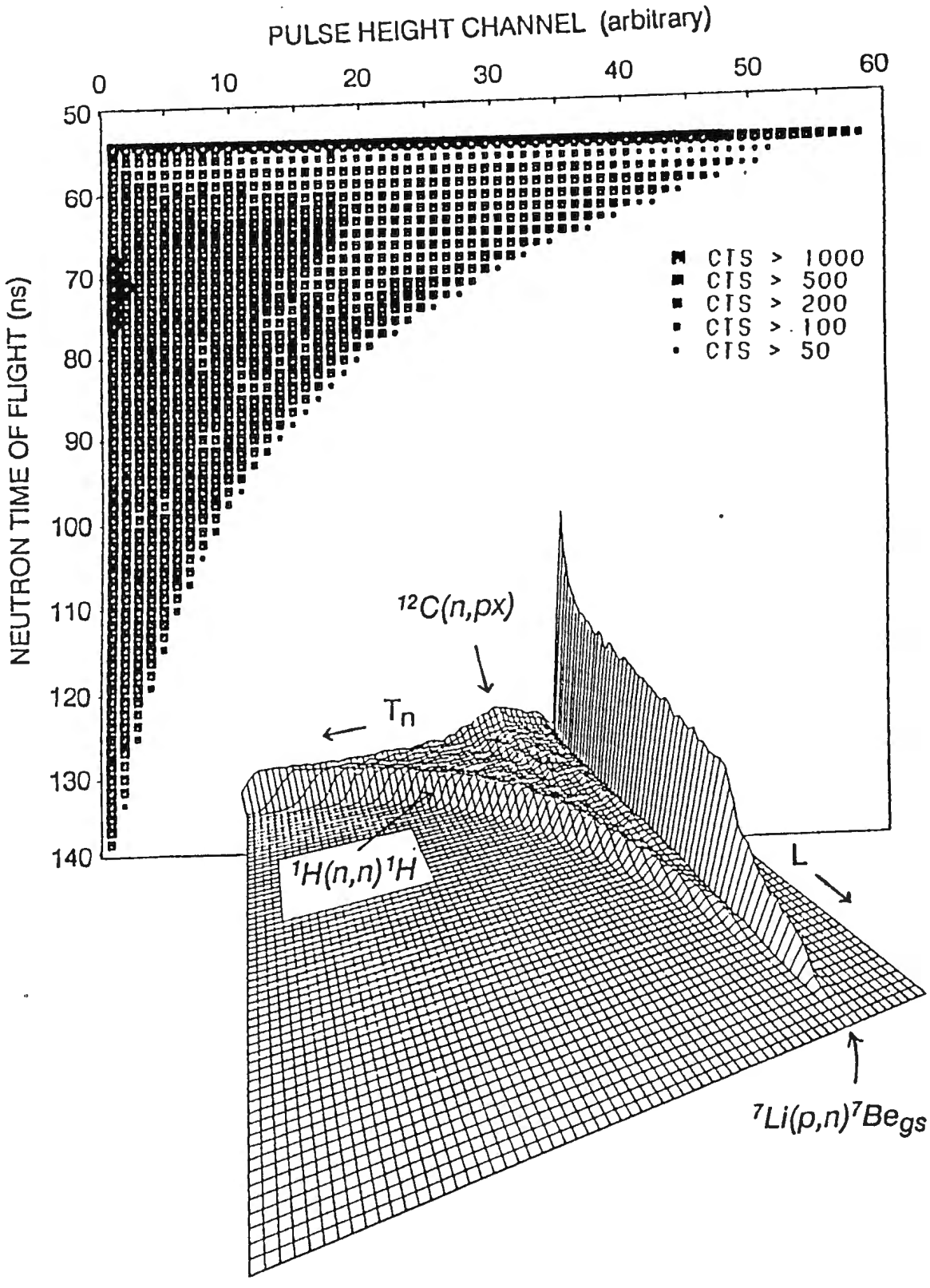

Figure 3.7 Event density (above) and perspective view (below) of counts (vertical) versus neutron time of flight, T_n, and NE213 pulse height, L, for events identified as protons by pulse shape discrimination (see figure 3.1). Labelled is the curved edge marking the upper pulse height limit for protons recoiling from $^1H(n,n)^1H$ events and the region associated with n-^{12}C events.

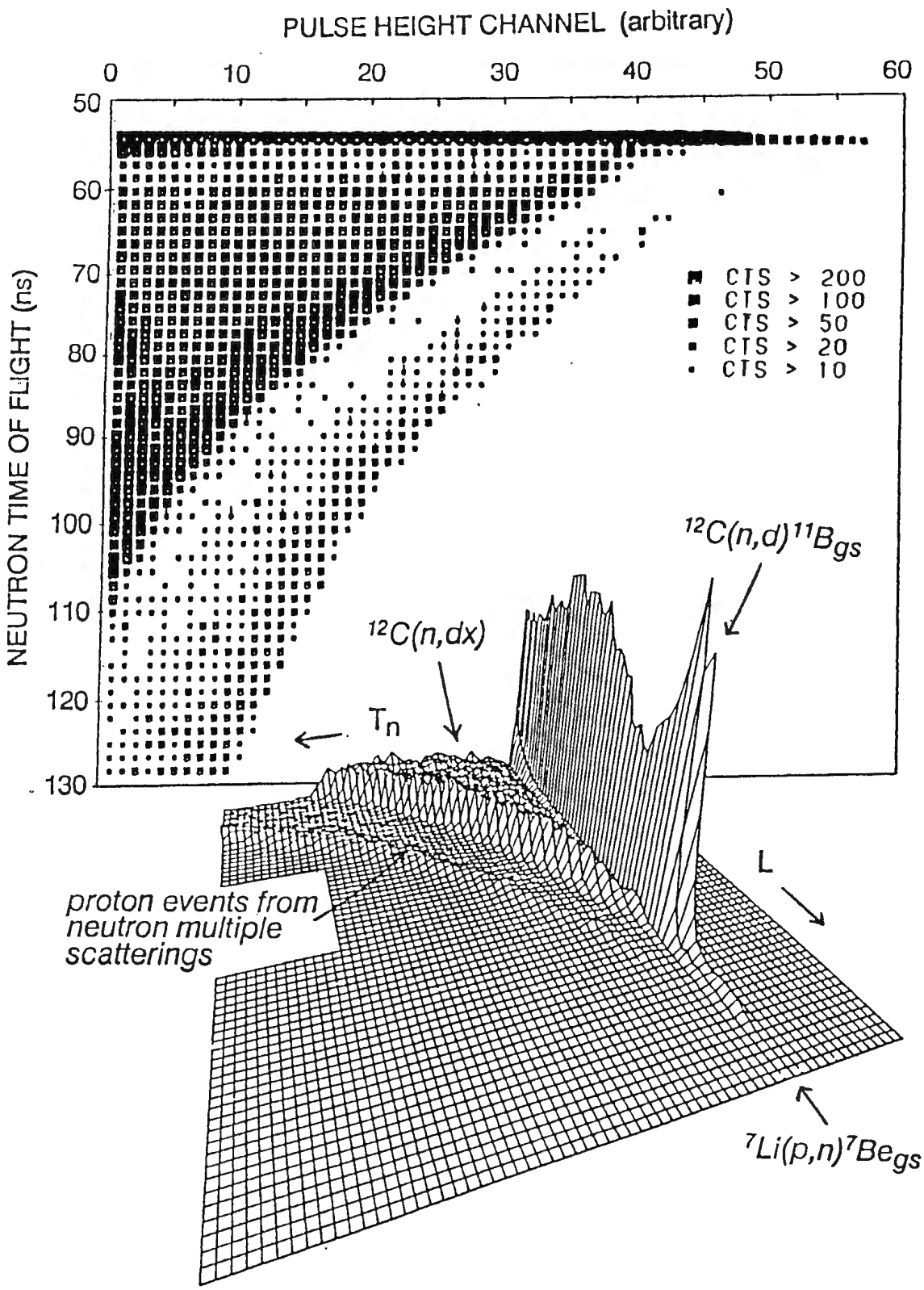

Figure 3.8 Event density (above) and perspective view (below) of counts (vertical) versus neutron time of flight, T_n, and NE213 pulse height, L, for events identified as deuterons by pulse shape discrimination (see figure 3.1). Labelled is the region associated with proton events from proton breakthrough into the deuteron corridor (see figure 3.6). Also labelled are the events associated with neutron induced deuteron production from ^{12}C nuclei in the scintillator and a peak which arises from the ground state transition of the $^{12}C(n,d)^{11}B$ reaction.

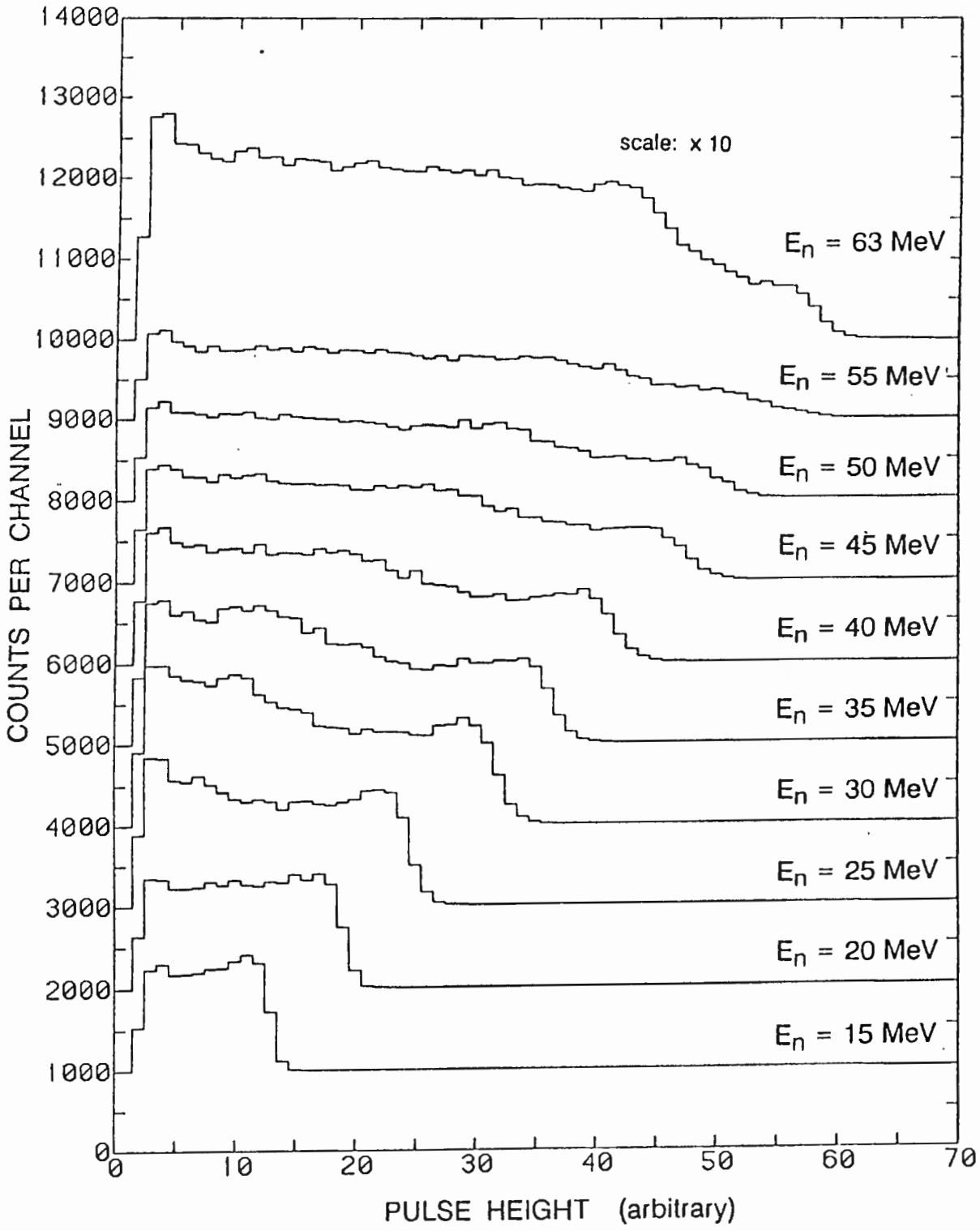

Figure 3.9 Counts versus pulse height (arbitrary) for the proton events observed at the different incident neutron energies considered in this work. Neutron energy was selected by time of flight windows and protons were selected by the L-S corridor (cut) shown in figure 3.6.

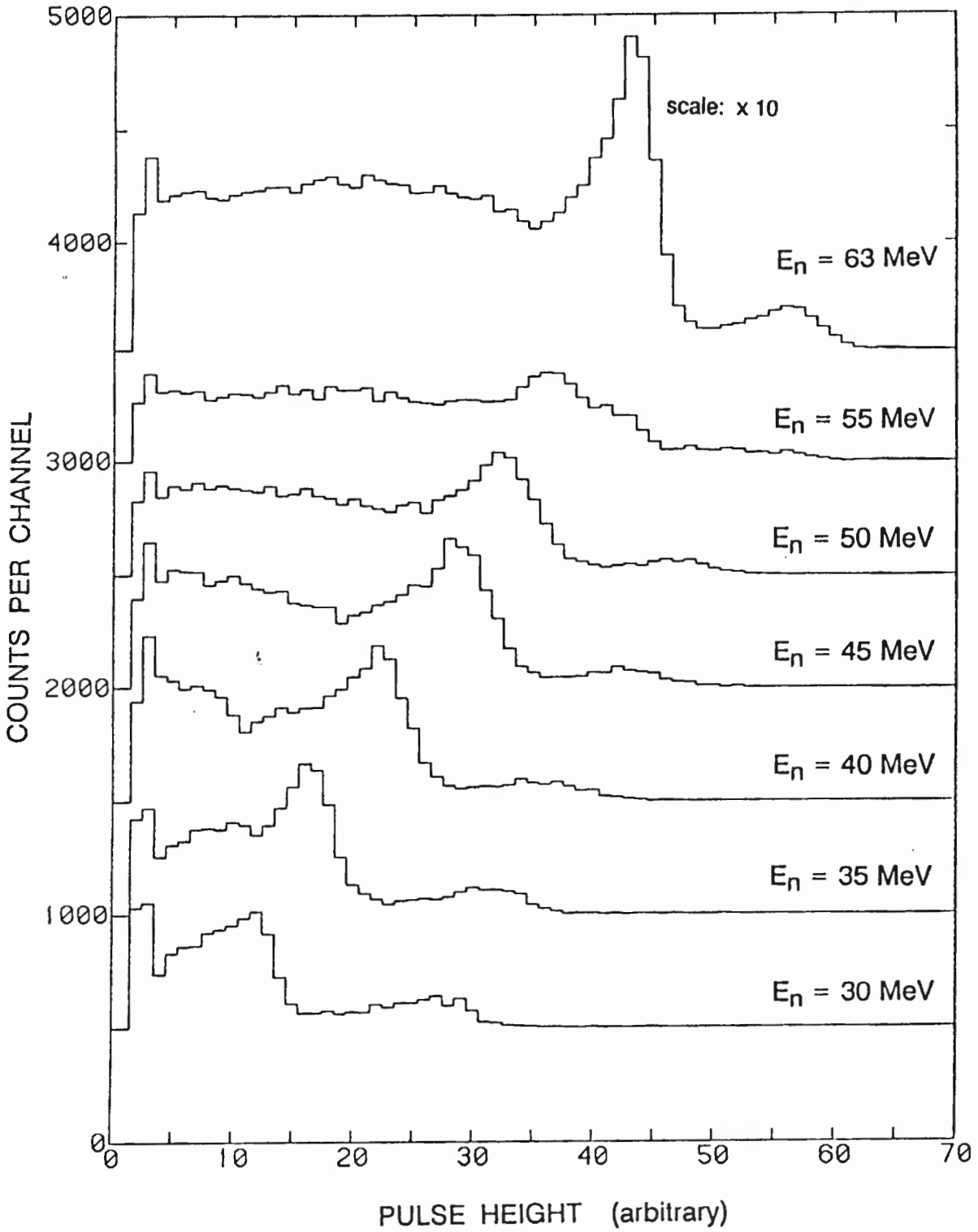

Figure 3.10 Counts versus pulse height (arbitrary) for the deuteron events observed at the different incident neutron energies considered in this work. Neutron energy was selected by time of flight windows and deuterons were selected by the L-S corridor (cut) shown in figure 3.6.

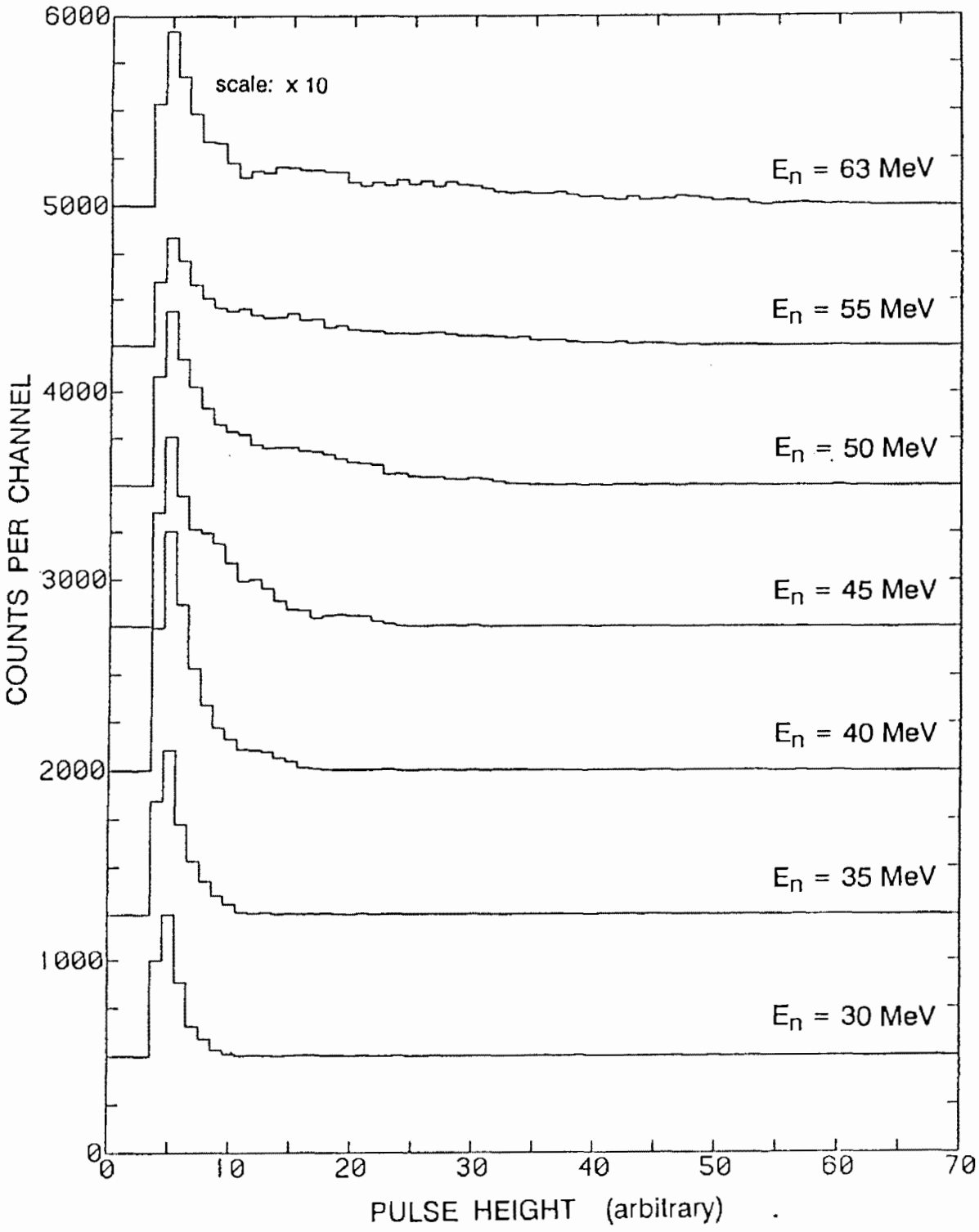

Figure 3.11 Counts versus pulse height (arbitrary) for the alpha events observed at the different incident neutron energies considered in this work. Neutron energy was selected by time of flight windows and alphas were selected by the L-S corridor (cut) shown in figure 3.6.

were clearly separated. However, at lower pulse heights particularly, where the overlap of neighbouring charged particle loci was appreciable, a more thorough method of separation was deemed to be necessary.

Consider the *L*-*S* spectrum measured at 63 MeV (figure 3.1). The counts in each pulse height channel were individually projected onto the *S*-axis. This produced pulse shape parameter (*S*) spectra at each pulse height, a selection of which was shown in figure 3.5. For each of these *S*-spectra, a standard Gaussian distribution was then fitted to the peak produced by each type of charged particle. To this end, use was made of the interactive data-manipulation code *OPDATA* (Be89). Typical *S*-spectra and fits for three pulse height channels are shown in figure 3.12. The integrals of the Gaussians fitted to the proton and deuteron peaks were determined at each pulse height, producing pulse height spectra for these charged particles at E_n = 63 MeV.

The same procedure was repeated for *L*-*S* spectra measured at other incident neutron energies in the range 15-63 MeV. Pulse height spectra for protons and deuterons obtained by this method are presented in figure 3.13 and figure 3.14 respectively. As this procedure of separation is considered superior to that described in (a) above, all further analyses, such as those to determine cross sections and neutron detection efficiencies, were made from these pulse height spectra.

From about three quarter the distance down the proton ridge, another Gaussian distribution (see figure 3.12(c)) was included between the proton and deuteron peaks to incorporate the effect of multiple scattering. In this way, much of the overlap of the proton and deuteron loci, which was manifested in figure 3.8, was eliminated.

Figure 3.15 shows the alpha region of the *L*-*S* two-parameter spectrum measured at E_n = 63 MeV plotted by the same method as figure 3.6. A finer discrimination may be made between the detected alphas released in the two competing alpha reations, viz. $^{12}C(n,\alpha)^{9}Be$ and $^{12}C(n,n')3\alpha$ (the basis for this identification is discussed in section 5.3). These could be well separated at the higher pulse heights where a peak arising from the transiton to the ground

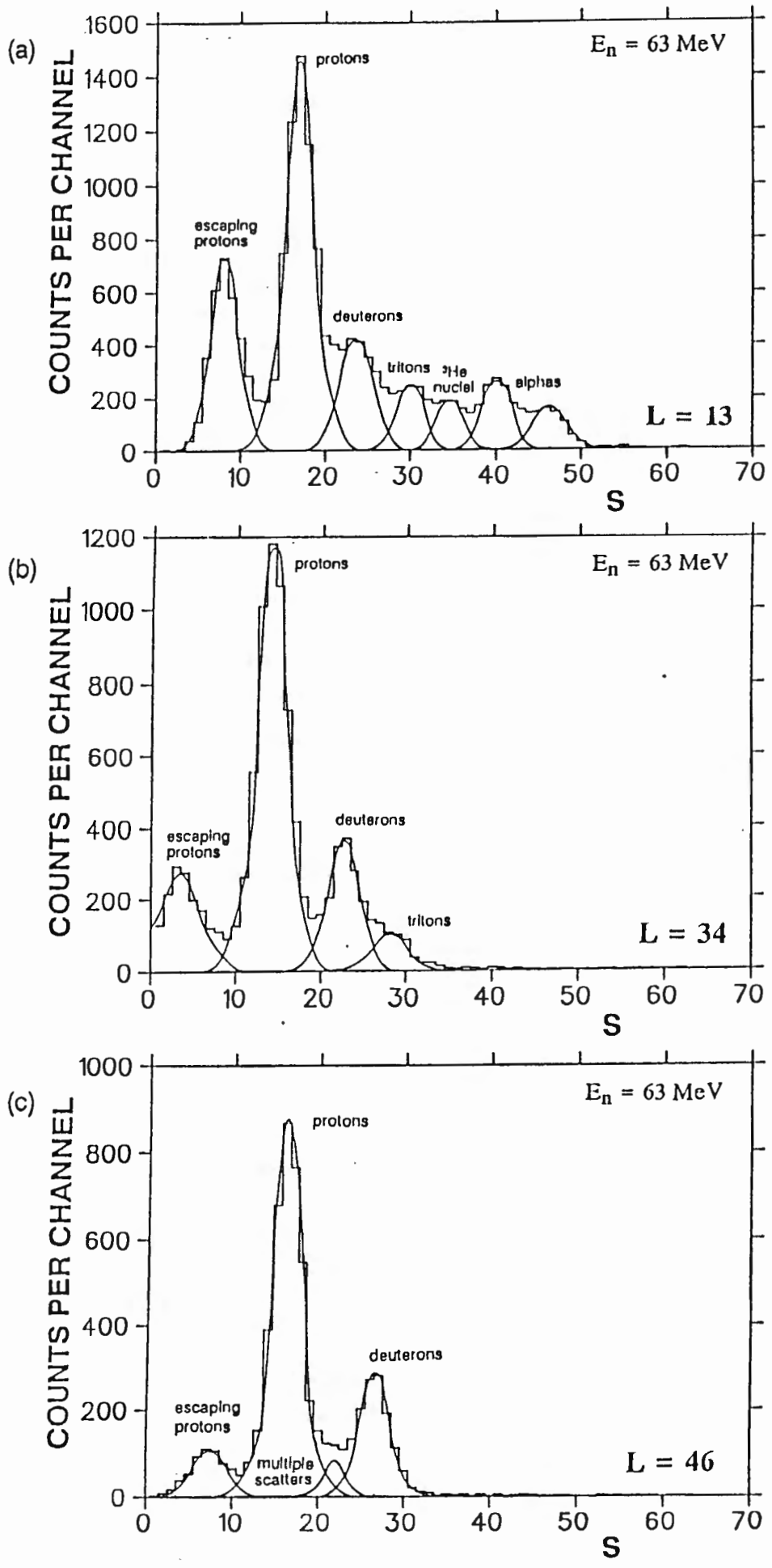

Figure 3.12 Counts versus pulse shape parameter, S , for the following pulse height channels of the L-S spectrum (figure 3.1) measured at E_n = 63 MeV: (a) L = 13; (b) L = 34; and (c) L = 46. Gaussian distributions are fitted to the peak associated with each type of charged particle, as labelled (see text).

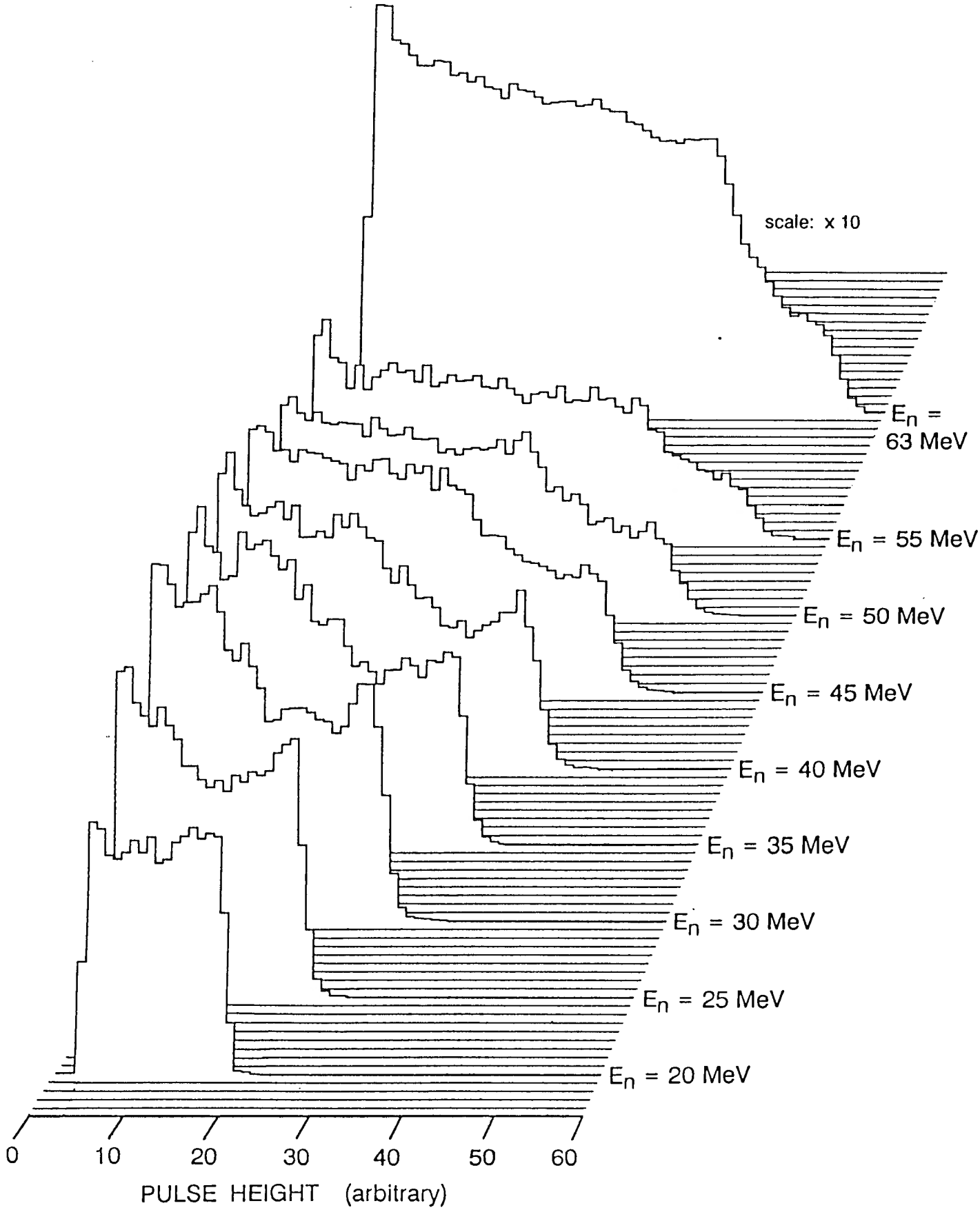

Figure 3.13 Proton pulse height spectra for the different neutron energies considered in this work. Each channel of each spectrum corresponds to an integral of a Gaussian distribution fitted to the proton peak (see figure 3.13) of the particular S-spectrum (see text).

state of ^{9}Be was resolved near the end of the ^{12}C(n,α)^{9}Be locus. As this peak was used as a reference for the measurement of the scintillator response to alphas, pulse height spectra for alphas released in the ^{12}C(n,α)^{9}Be reaction were obtained as a function of neutron energy (figure 3.16) using the procedure of Gaussian fitting described above.

Hence, by both methods described above, proton, deuteron and alpha pulse height spectra were separated from the measured neutron lineshapes as a function of incident neutron energy.

Figure 3.17 shows the time of flight spectrum (figure 2.6) together with the charged particle components of the spectrum, separated by the method (software corridor) outlined in section 3.2(a), above. These components were obtained by projecting the proton, deuteron and alpha signals measured at all E_n onto the T_n-axis. There are two features in the spectrum which are associated with the experimental conditions and method of separation respectively. The cyclotron pulse selector occasionally allowed the passage of protons from one of the four excluded injector cyclotron beam pulses (see section 2.1(a)). This gave rise to a "breakthrough" peak of 63 MeV neutrons associated with the next beam pulse, identified in figure 3.17 at T_n = 115 ns. Secondly, photomultiplier statistics causes the proton and deuteron spectra to merge towards the low energy limit of the time of flight spectrum (T_n < 100 ns).

In order to quantitatively compare the two different methods ((a) and (b)) used to resolve the different charged particle signals, figure 3.17 also shows the integrals of the proton and deuteron pulse height spectra obtained from the method of fitting gaussians. As expected, the two separation methods give similar results at the higher neutron energies. However, with decreasing neutron energy, the second, more critical method of fitting Gaussians as described in section 2(b), gives results which are consistently lower for the protons and consequently higher for the deuterons. This indicates the better separation by the second method of separation of the proton and deuteron loci in the region of poorer statistics at the lower neutron energies.

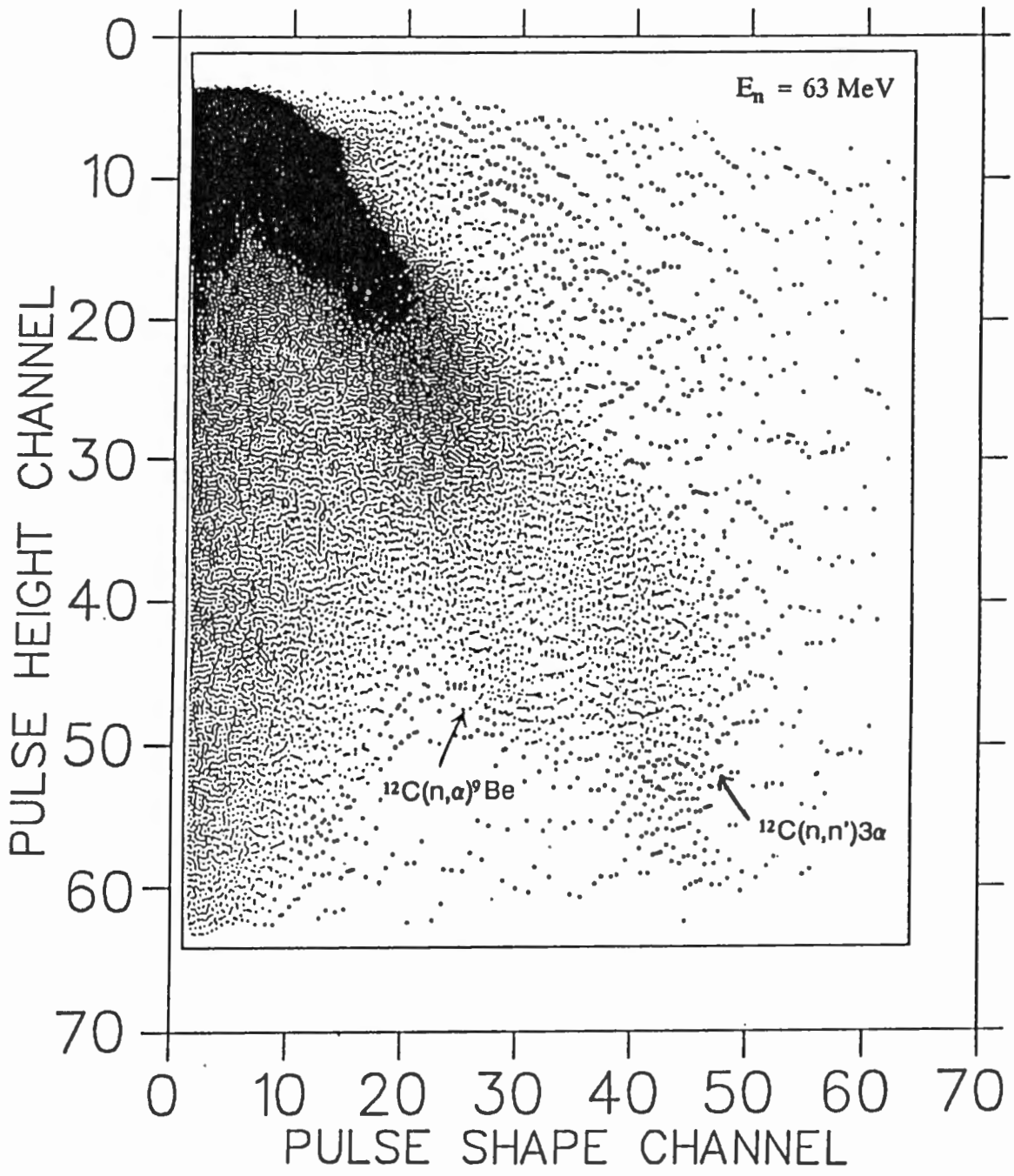

Figure 3.15 Event density plot of pulse shape parameter, S , versus pulse height, L (both arbitrary channels), for events identified as alphas by pulse shape discrimination. A partial separation of the event signals corresponding to alphas released in the two competing alpha reactions, namely $^{12}C(n,\alpha)^9Be$ and $^{12}C(n,n')3\alpha$, is identified (see also figure 3.1).

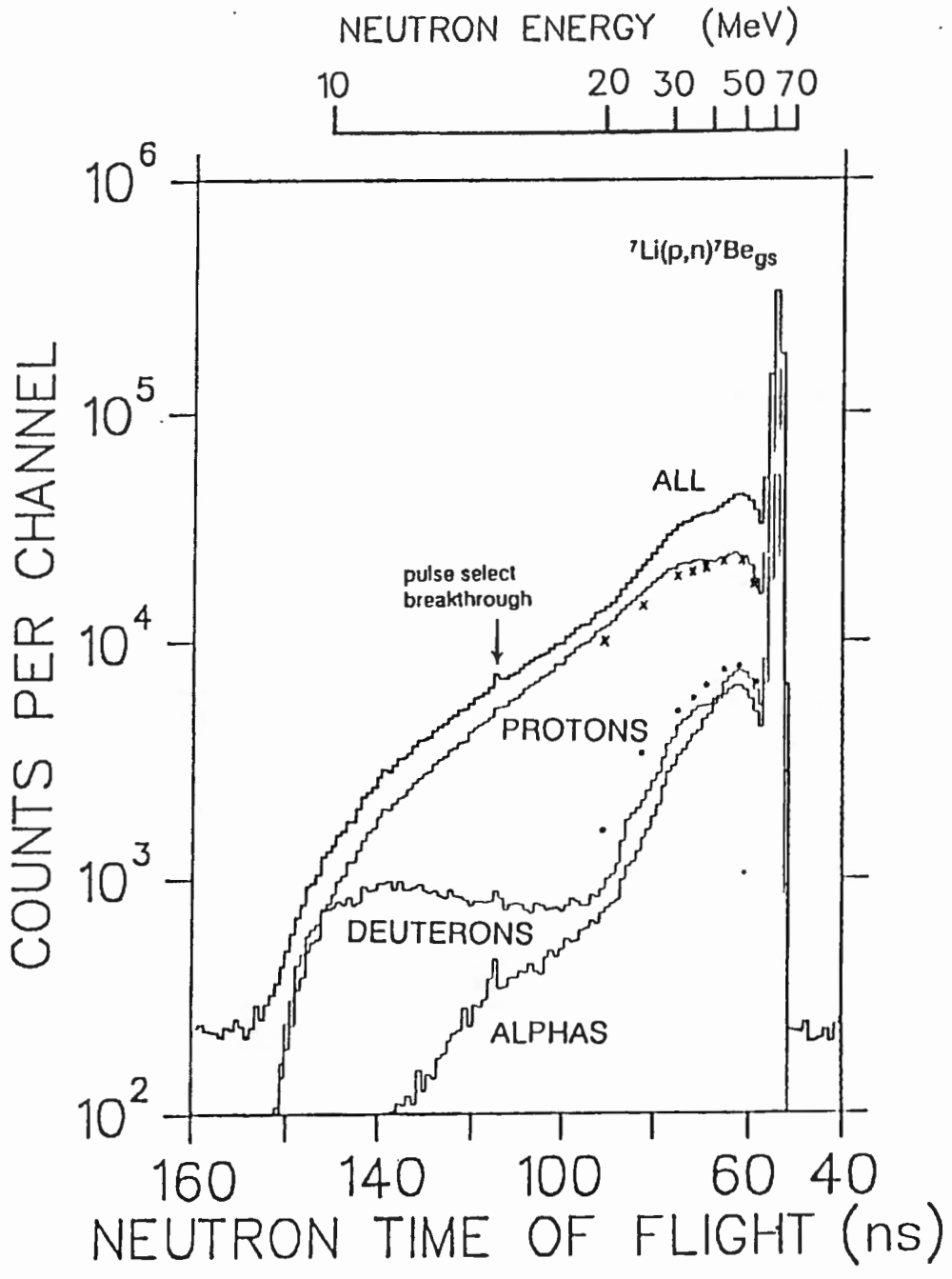

Figure 3.17 Counts versus neutron time of flight for all events measured in a 5 cm by 5 cm (diameter) cylidrical NE213 scintillator. Also shown are the components associated with events in the scintillator identified as protons, deuterons and alphas by pulse shape discrimination and selected by the L-S corridors shown in figure 3.6. Photomultiplier statistics is responsible for the deuteron spectrum approaching the proton spectrum with increasing neutron energy (T_n > 100 ns). The peak at T_n = 115 ns is attributed to pulse selection breakthrough of the next proton beam pulse.

Also shown are the integrals of the proton (x) and deuteron (•) pulse height spectra obtained by the method of fitting Gaussians as outlined in section 3.2(b). It is evident that this method of separating the different charged particle signals is superior, particularly with decreasing neutron energy.

3.3 FINITE SIZE EFFECTS

There are two experimental complications in this work which are sensitive to the physical dimensions of the scintillator used. The first is the "edge effect" whereby recoiling particles escape from the detector and the second is the multiple scattering effect whereby the same neutron will interact more than once in the scintillator.

(a) ESCAPING PROTONS

Recoiling charged particles are able to escape from any size detector without depositing all of their ionization in the scintillator volume. The fraction of particles escaping will increase with incident neutron energy (or decreasing detector size) as the range of the recoiling charged particle approaches or exceeds the dimensions of the detector. The number of particles escaping out of the sides of the detector will depend on the angular distributions of the reactions releasing the charged particles. It is clear that this effect will also depend on the geometrical orientation of the detector.

The range of 63 MeV protons in NE213 is 3.8 cm, which is significently larger than that for deuterons (2.0 cm) or alphas (0.3 cm) of the same energy. In this work therefore, since the dimensions of the cylindrical scintillator are 5 cm (diameter) by 5 cm, the dominant escape effects will be those for the protons.

The proton may escape after depositing any fraction of its energy in the scintillator depending on the distance it travels in the detector. Since energy losses are largest towards the end of the proton range, where the specific energy loss, dE/dx, reaches a maximum (the Bragg peak), most escaping protons will deposit only a small fraction ($< 40\%$) of their energy in the scintillator. Furthermore, since this energy is deposited with a significently lower average dE/dx than for a stopping proton which gives rise to the same pulse height in the scintillator, there is a marked effect on the pulse shape. As

a result, the pulse shape discrimination circuit will interpret the signal as coming from a lighter particle and escaping recoil protons, for example, can be detected and misidentified as electrons.

Shown in figure 3.18 is an event density *L*-*S* spectrum measured at E_n = 63 MeV. Consider protons of a particular energy released in either n-^{12}C or n-p elastic scattering events. Suppose that the *L* and *S* coordinates of the scintillation signals from protons of this energy that do not escape will place the events at the unique point, *P*, on the proton ridge as indicated in figure 3.18. The signals from escaping protons of this initial eneryg will then lie on a locus that starts at point *P* and is asymptotic to the position of the gamma ridge, as shown, at coordinates of *L* and *S* depending on the amount of energy deposited before escape. The escape loci associated with protons of all energies in the range 5-63 MeV, when summed together, form the proton escape ridge identified in the *L*-*S* spectrum. Only a small fraction of the escape events fall in the valley between the proton and escape ridges.

(b) MULTIPLE SCATTERING

Some of the neutrons entering the detector will be involved in two or more interactions before leaving the scintillator volume. For example, a neutron may enter the NE213 cylinder, elastic scatter off a proton and then initiate a ^{12}C(n,p)^{12}B reaction. The average ionization density in the scintillator for the event will obviously be higher than if only the n-p elastic scattering took place. The scintillator will simultaneously record the scintillations caused both protons and consequently the light output will appear to result from a slightly heavier particle. The region of counts arising from proton multiple scattering is labelled in figure 3.18. This effect will become more important as the size of the detector approaches and exceeds the neutron mean free path at the particular incident neutron energy.

In order to minimize, optimally, these effects of proton escape and neutron multiple scattering, the detector size should be chosen so as to fall between

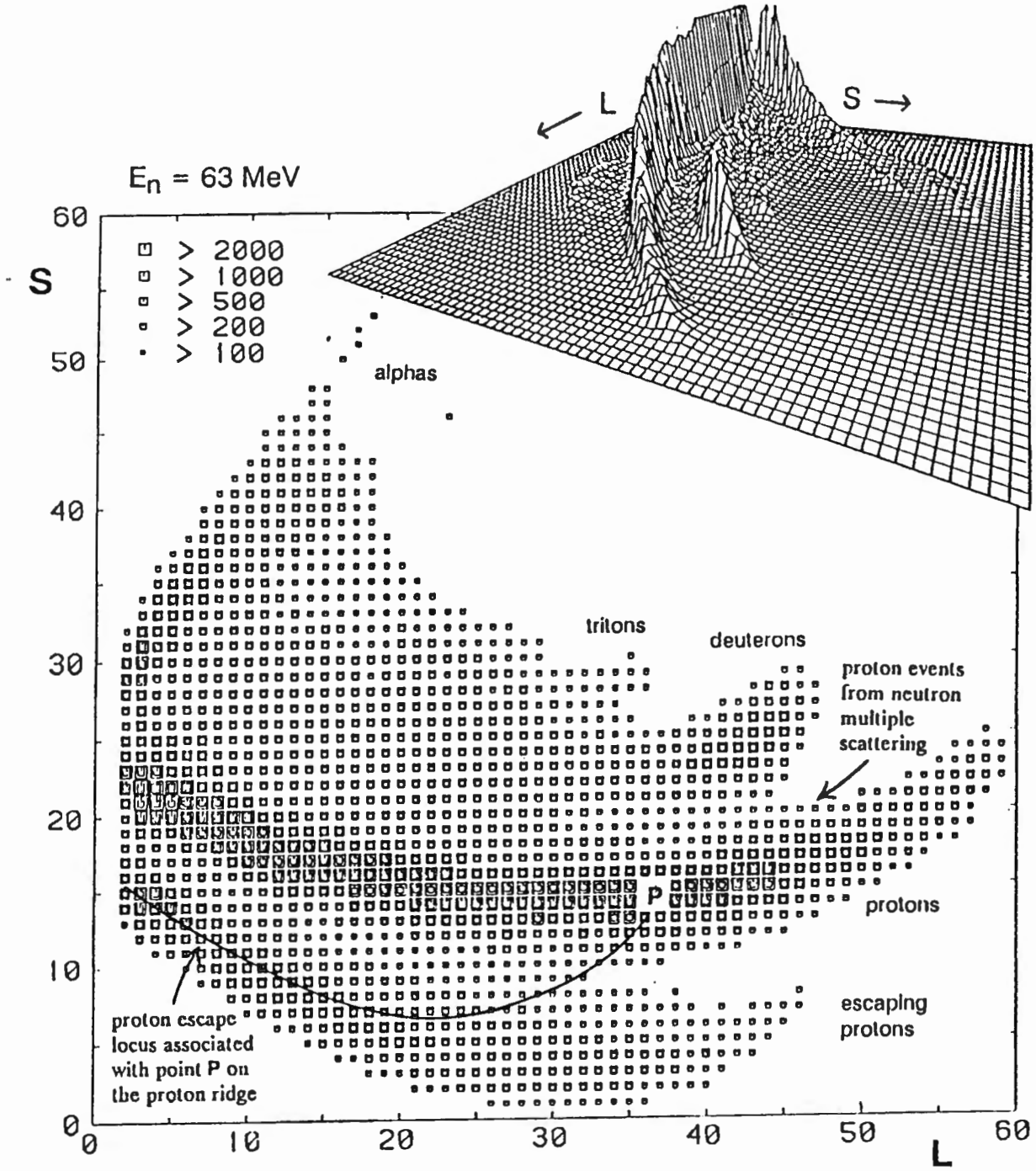

Figure 3.18 Event density plot of events versus pulse height, L, and pulse shape parameter, S, measured at E_n = 63 MeV; and (inset) a perspective view of the same spectrum. Consider protons of energy E_p, located at point P on the proton ridge if they do not escape from the detector volume. The signals of those protons of energy E_p which do escape then lie on the locus indicated by the curved line extending from P. Also labelled is the region of proton signals arising from neutron multiple scattering events.

the mean free path of the neutron in scintillator, and the maximum recoil range of the primary particle to be detected. For the cylindrical detector used in this work (50 mm high x 50 mm diameter), edge effects dominate at the higher neutron energies as 63 MeV protons have a range of 38 mm in NE213. However, these edge effects would be reduced by orientating the scintillator with its axis facing the incident neutron beam.

The detector lineshapes, measured for incident neutrons in the range 15-63 MeV, have been unfolded into charged particle pulse height spectra, identified as protons, deuterons and alphas by pulse shape discrimation. The following chapter describes how measurements were made from these spectra of the scintillator response to protons, deuterons and alphas as a function of charged particle energy.

CHAPTER 4

THE RESPONSE OF NE213 TO CHARGED PARTICLES

Pulse height spectra of the scintillator for protons, deuterons and alphas were unfolded from the detector lineshapes measured for incident neutrons in the energy range 15-63 MeV. These pulse height spectra each displayed features which could be identified with particular energy for the particle concerned. This allowed the scintillator response (light output) to be determined simultaneously for protons, deuterons and alphas as a function of charged particle energy, from the data obtained under the same experimental conditions. A comparison was made between the present measurements and the response theory for organic scintillators of Birks.

4.1 RESPONSE MEASUREMENTS

(a) THE RESPONSE TO ELECTRONS

It is useful to express the response of a scintillator to a charged particle, such as a proton, in terms of the equivalent electron energy, that is, in units of MeVee (MeV electron equivalent). This indicates the electron energy that produces the same light output or pulse height from the scintillator as the charged particle. Since the total light emitted by electrons of energies greater than 125 keV is a linear function of energy (Cr70), a few calibration measurements made using gamma sources of known energy suffice to calibrate the pulse height scale in this way. In this work, calibration was achieved by recording the pulse height spectrum for the 4.44 MeV γ-ray from an AmBe source at the same time and under the same experimental conditions as the neutron response measurements.

Figure 4.1 shows a pulse height spectrum recorded, for gammas only, from AmBe. The features in the spectrum are the Compton peak and edge as well as the pair production double escape peak. This 3.42 MeV double escape peak, which arises from the pair interaction of the 4.44 gamma ray on the carbon component of the NE213, provides an unambiguous calibration reference as its mean value is insensitive to both multiple scattering and the detector pulse height resolution.

The Compton peak and the Compton edge, the latter measured at half the peak intensity, were also used as calibration points. The pulse height channel of the Compton peak was associated with an electron energy equal to 0.95 that of the calculated maximum Compton electron energy as suggested by Madey *et al* (Ma78). The energy of the Compton edge, E_C, was calculated using:

$$E_C = \frac{2E_\gamma^2}{2E_\gamma + m_e c^2} \quad MeV \tag{4.1}$$

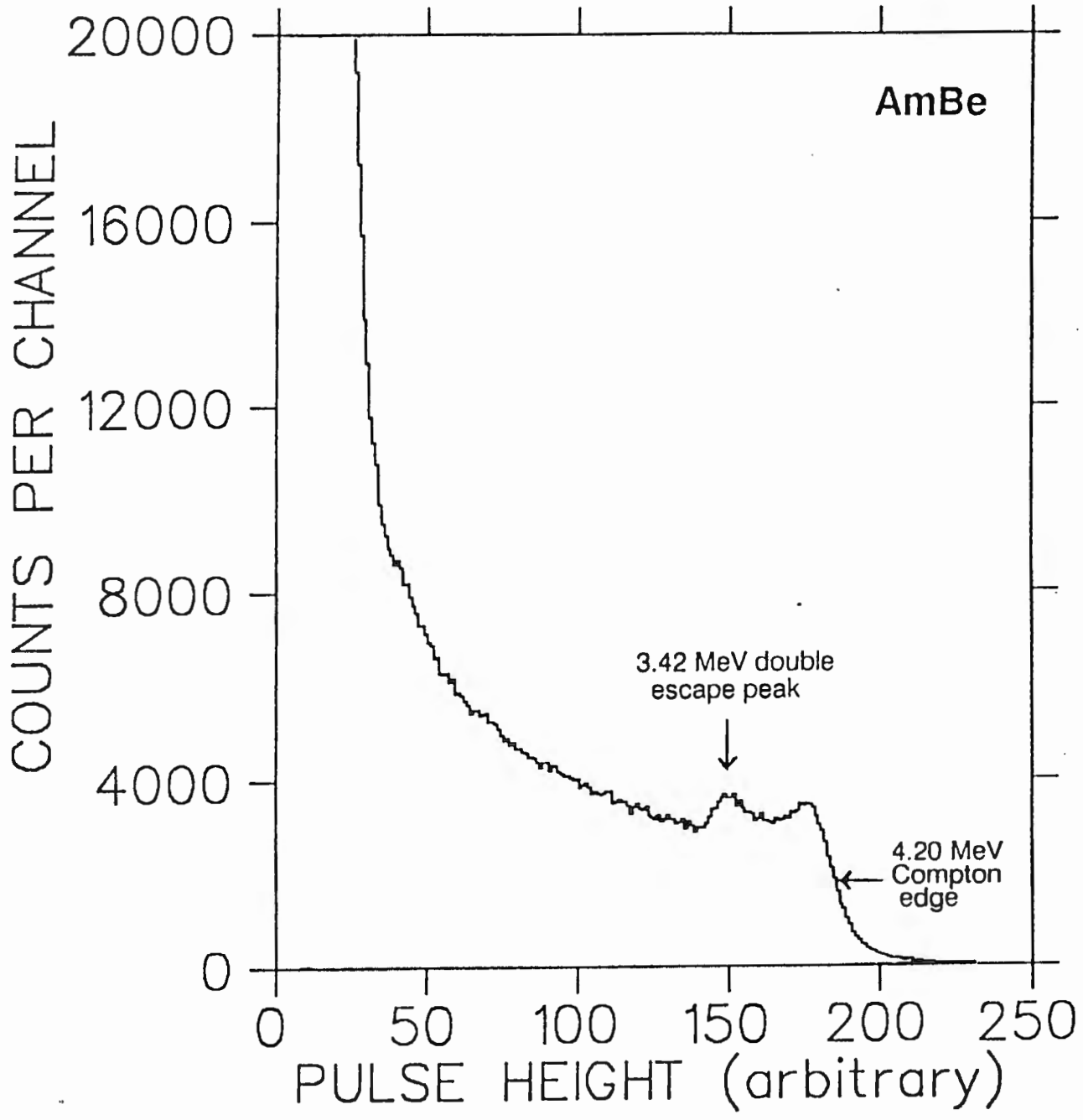

Figure 4.1 Pulse height spectrum for the 4.44 MeV γ-ray from an AmBe source, recorded with the NE213 detector, selecting gammas only, by pulse shape discrimination.

where $m_e c^2$ = 0.511 MeV is the electron rest mass energy. This gives E_C = 4.20 MeV for the Compton edge and 4.00 MeV for the electron energy associated with the Compton peak.

Figure 4.2(a) shows a pulse height spectrum for the 4.44 gamma ray from an AmBe source measured under the conditions of the neutron experiments, in which a pulse height threshold of about 3 MeVee was used. The three measurements of the Compton edge and the Compton peak, together with the double escape peak defined the electron energy scale shown in the figure. The linear dependence of the scintillation light output on electron energy was confirmed (figure 4.1(b)) and thus the pulse height scale could now be calibrated in units of MeVee.

(b) THE RESPONSE TO PROTONS

The half-height of the abrupt edge (broadened by the detection resolution) of the plateau at the upper edge of the proton pulse height spectra (figure 3.9) was assumed to correspond to the maximum energy of the recoil protons associated with $^1H(n,n)^1H$ events. This maximum proton energy, in turn, will equal the incident neutron energy, as only in scattering can a proton absorb all the energy of the neutron. The pulse height of this edge was measured in the proton pulse height spectra obtained at different neutron energies (time of flight). This gave the measurements of pulse height versus proton energy presented in figure 4.3.

The scintillator response to protons is predicted by response theories, such as that of Birks for organic scintillators (see section 1.1), and other measurements to be linear at high pulse heights with a slope equal to that of the scintillator response to electrons. The scintillator response to protons is also expected to approach zero in a non-linear fashion at low pulse heights. It can be seen in figure 4.3 than the proton responses measured in this work agree well with these predictions at proton energies less than about 15 MeV. However, there is a deviation from linearity (indicated by the dashed line) at

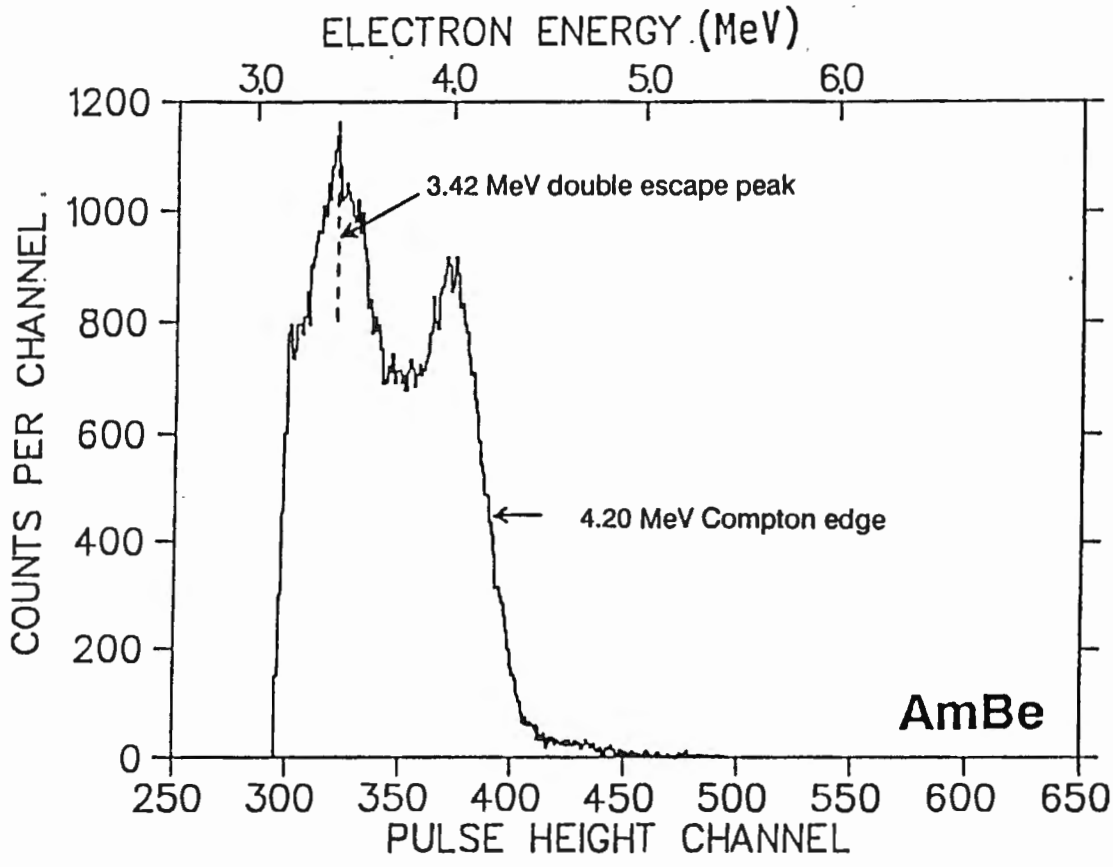

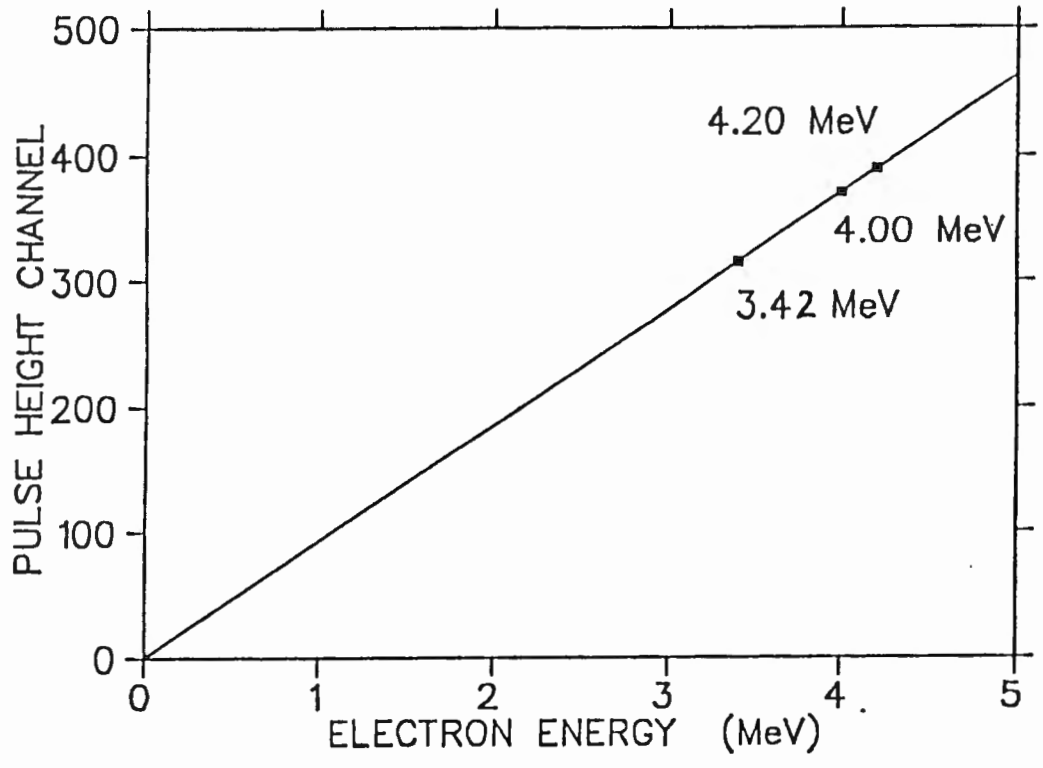

Figure 4.2 *(a) (above) Pulse height spectrum for the 4.44 MeV γ-ray from an AmBe source, recorded with the NE213 detector under the same experimental conditions as the measurements with the neutron beam.*

(b) (below) Calibration of pulse height channel to electron energy. The calibration points, measured from the spectrum in (a), above, are respectively: the Compton edge (4.20 MeV); the Compton peak (4.00 MeV); and the double escape peak (3.42 MeV).

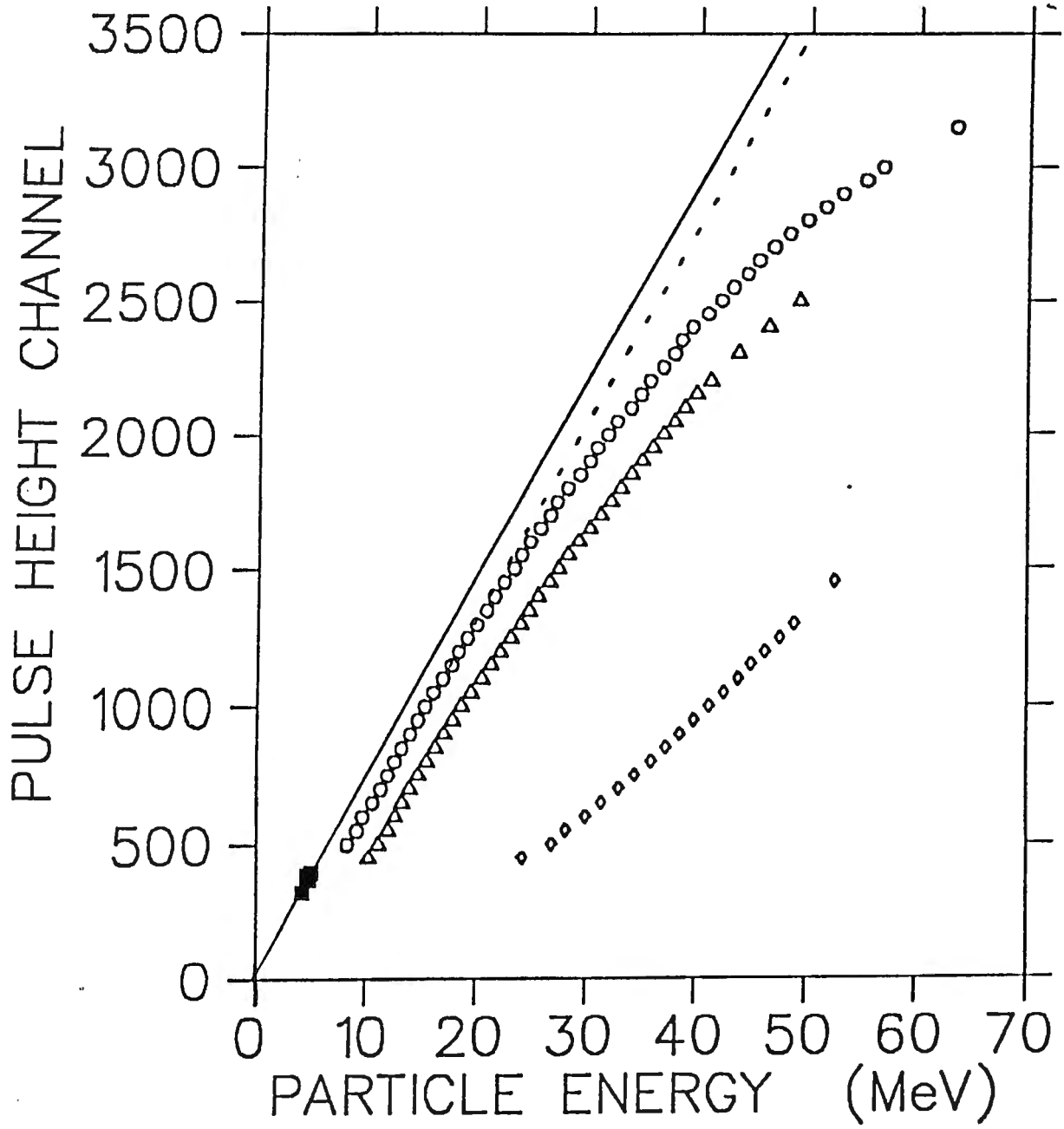

Figure 4.3 Measurements of the response (pulse height) of NE213 to (■) electrons, (o) protons, (△) deuterons and (◇) alphas as a function of charged particle energy. The solid line through the electron data has the same slope as the straight line in figure 4.2(b). The dashed line shows the non-linearity of the proton measurements at pulse height channels greater than 1300. This is attributed to space charge saturation in the photomultiplier (see text).

higher pulse heights which is attributed to space charge saturation in the photomultiplier, for reasons outlined below. Section 4.1(e) describes how the data have been corrected for this instrumental effect.

(c) THE RESPONSE TO DEUTERONS

A particular feature of the deuteron pulse height spectra (figure 3.10) is the peak which arises predominantly from the transition to the ground state of ^{11}B (Me67) in the reaction $^{12}C(n,d)^{11}B$. Figure 4.4 shows the outgoing deuteron energy as a function of incident neutron energy for this transition calculated using the standard reaction kinematics equations (see Appendix A). The $^{12}C(n,d)^{11}B$ reaction is forward peaked in the laboratory frame (see section 5.1) and the recoiling ^{11}B nucleus removes less than 5% of the available kinetic energy. Also, the scintillator light output for these recoiling ^{11}B nuclei will be of the order of 4% of the light output for a deuteron of the same energy. It therefore was assumed for the purpose of these measurements that the recoiling ^{11}B nucleus makes a negligable contribution to the scintillation pulse height.

The pulse height of the $^{12}C(n,d)^{11}B_{gs}$ peak, corresponding to deuteron energy calculated from the kinematic equations, was measured as a function of incident neutron energy (time of flight). The resulting deuteron response data are shown in figure 4.3. The space charge saturation effect is also clearly evident in these uncorrected data.

(d) THE RESPONSE TO ALPHA PARTICLES

The measured *L-S* two-parameter spectrum (figure 3.1) displayed fine structure in the alpha locus where the contributions from outgoing alphas released in the $^{12}C(n,\alpha)^{9}Be$ and $^{12}C(n,n')3\alpha$ reactions could be partially separated. This separation was sufficiently good to distinguish a peak near the end of the $^{12}C(n,\alpha)^{9}Be$ locus which is recognized to arise from the ground state transition of this reaction. The outgoing alpha energy corresponding to

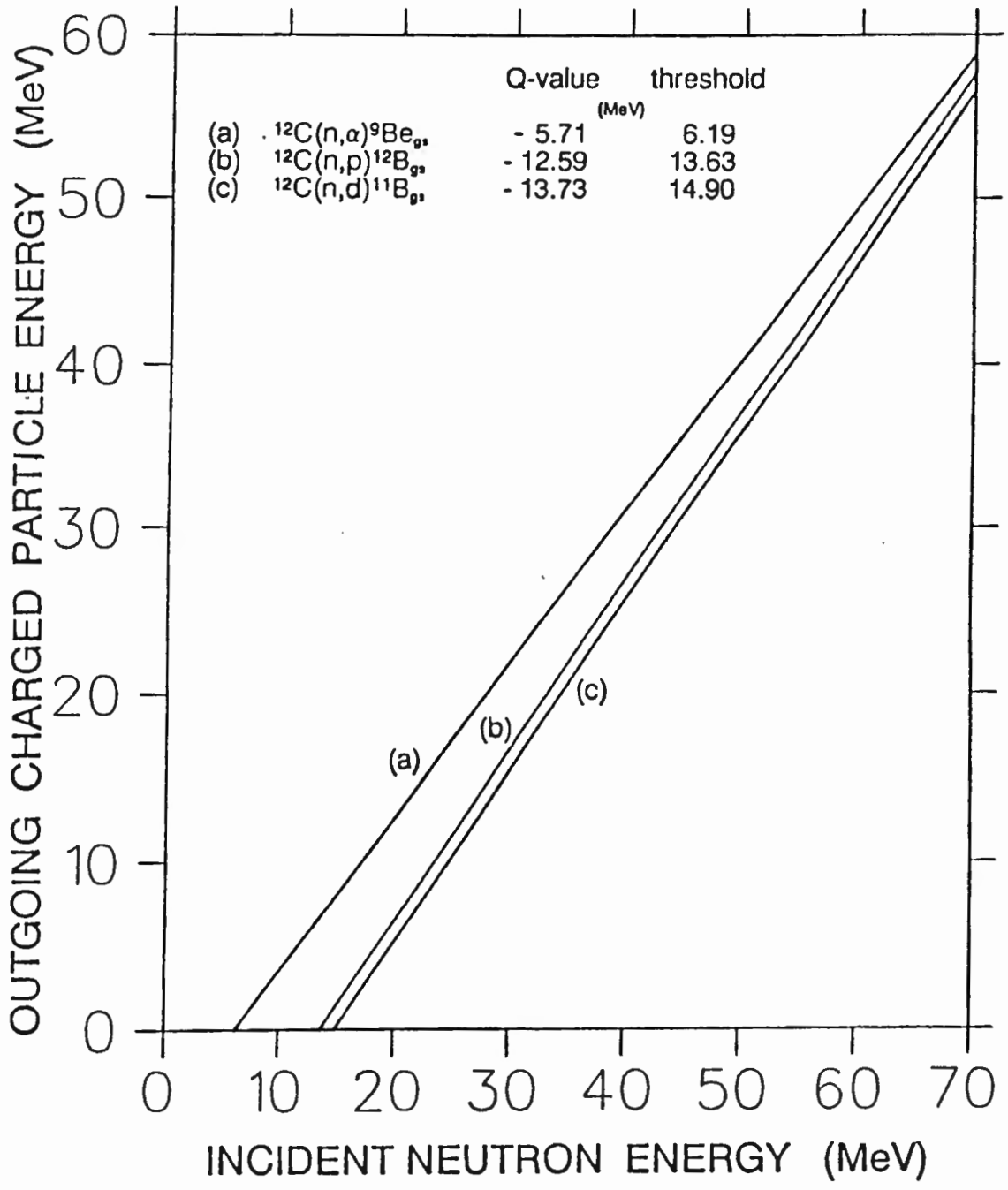

Figure 4.4 Maximum energy limit for the outgoing charged particle as a function of incident neutron energy for the reactions: (a) $^{12}C(n,\alpha)^{9}Be$; (b) $^{12}C(n,p)^{12}B$; and (c) $^{12}C(n,d)^{11}B$, calculated using the standard kinematics equations (Appendix A).

this transition was calculated as a function of incident neutron energy (figure 4.4). This ground state peak in the alpha pulse height spectra (figure 3.17) was used as a reference to measure the response of the scintillator to alphas as a function of energy (figure 4.3). Similarly, as in the case for deuterons, the recoiling ^{9}Be nucleus was assumed to contribute negligibly to the total pulse height.

(e) SPACE CHARGE SATURATION

It can be seen that the proton and deuteron response data deviate from the expected linear dependence (Br79) at higher pulse heights and that the deviation increases steadily with pulse height or particle energy. Subsequent tests showed that this effect was due to space charge saturation in the photomultiplier, arising largely from limitations introduced by the voltage divider circuit that was used (see section 2.2). In current work this problem has been overcome by replacing the photomultiplier voltage divider circuit (figure 2.5), so as to achieve operation without space charge saturation. For further processing of the data in this thesis, however, an empirical and essentially arbitrary correction has been made, as described below to remove the saturation effects.

To correct the measurements for this effect, a second order quadratic least squares fit of the form

$$L(E_p) = a E_p^{\,2} + b E_p + c \qquad (4.2)$$

was made in the affected region (L > channel 1300) of the measured proton response data where $a = -9.82 \times 10^{-5}$, $b = 1.13$ and $c = -62.31$ (figure 4.5(a)), for pulse height, L, in channels and proton energy, E_p, in MeV. As the scintillator response to protons is predicted by theory to be linear for high proton energies (Bi51), a straight line having slope equal to that of the measured electron response data (figure 4.2(b)) was fitted to the unaffected proton responses i.e. in the region L < 13 channel 1300. The proton responses measured in this work at pulse heights greater than

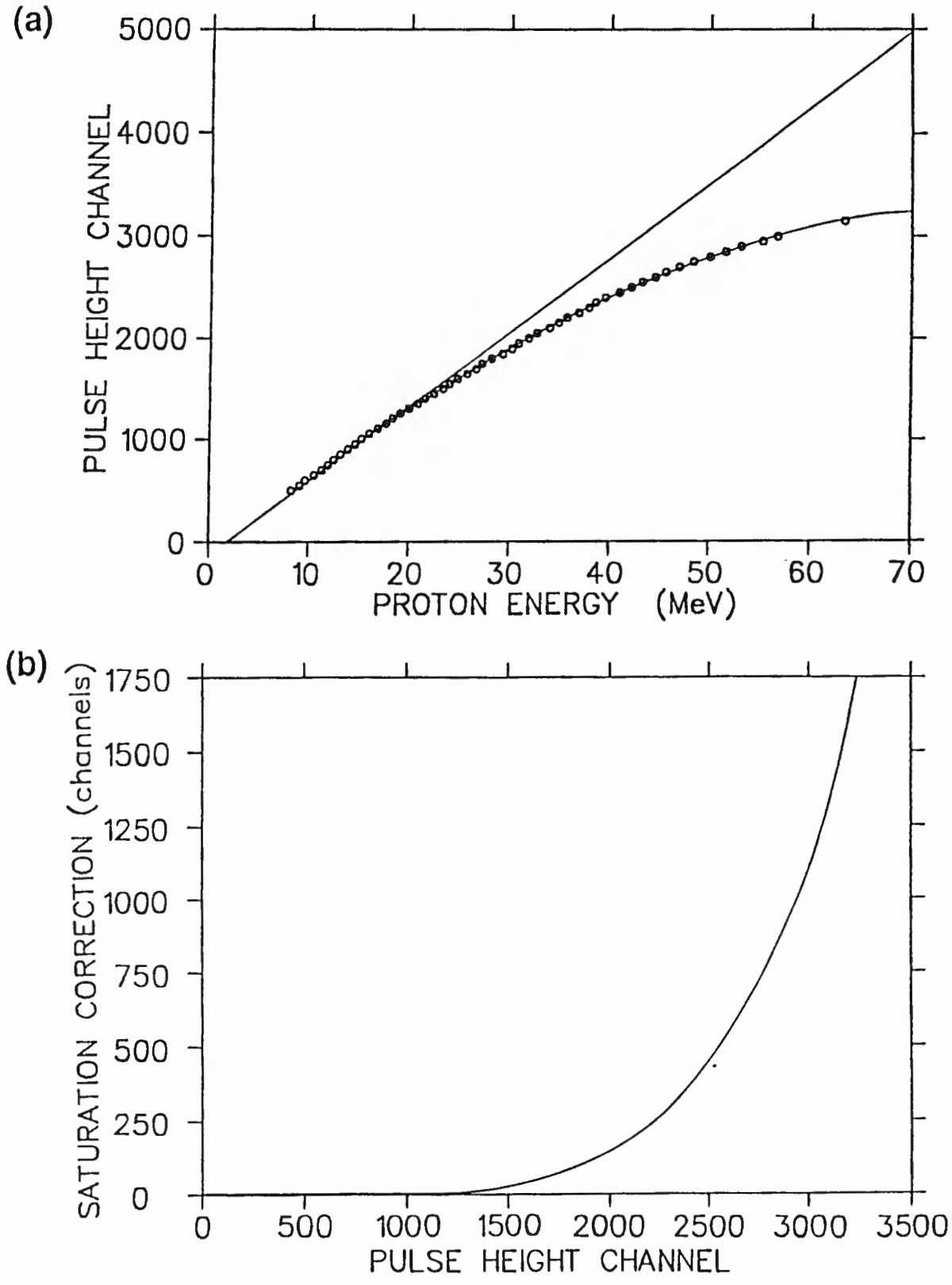

Figure 4.5 *(a) (above) Measurements of the scintillator response (pulse height) to protons as a function of proton energy. The straight line, fitted to the pulse height region less than channel 1300, has the same slope as that in figure 4.2(b). The pulse height region greater than channel 1300 has been fitted with a quadratic (see text).*

(b) (below) The correction applied to the proton, deuteron and alpha response data for the effect of space charge saturation as a function of pulse height, defined by the difference between the straight line and the quadratic in (a), above.

channel 1300 were then corrected to this straight line. The deviation of equation 4.2 from linearity (figure 4.5(b)) describes the correction for this instrumental effect. In correcting the deuteron and alpha data for this effect, it was assumed that the degree of saturation depends only on the pulse height, L. The corrected measurements of the scintillator response (in units of MeVee) to protons, deuterons and alphas are shown together with the electron data in figure 4.6.

4.2 COMPARISON WITH THEORY AND OTHER MEASUREMENTS

(a) THE BIRKS RELATION

The simultaneous measurement of the scintillator response to electrons, protons, deuterons and alphas presented an opportunity to compare with the predictions of the response theory of Birks. By integrating equation 1.1, we obtain:

$$L(E_p) = A \int_0^{E_p} (1 + B\, dE/dx)^{-1}\, dE \qquad (4.3)$$

where:

$L(E_p)$: Total scintillator light output to a charged particle of energy E_p

dE/dx : Specific energy loss for the charged particle of energy E in the scintillator

A : Normalizing constant

The constant B, or so-called 'Birks parameter' was determined by fitting equation 4.3 independently to the corrected proton, deuteron and alpha response measurements (figure 4.6). This gave the values B = 0.0145, 0.0146 and 0.0149 $g.cm^{-2}.MeV^{-1}$ respectively. These values are consistent, as expected from the Birks theory, and give a mean value for the Birks parameter of

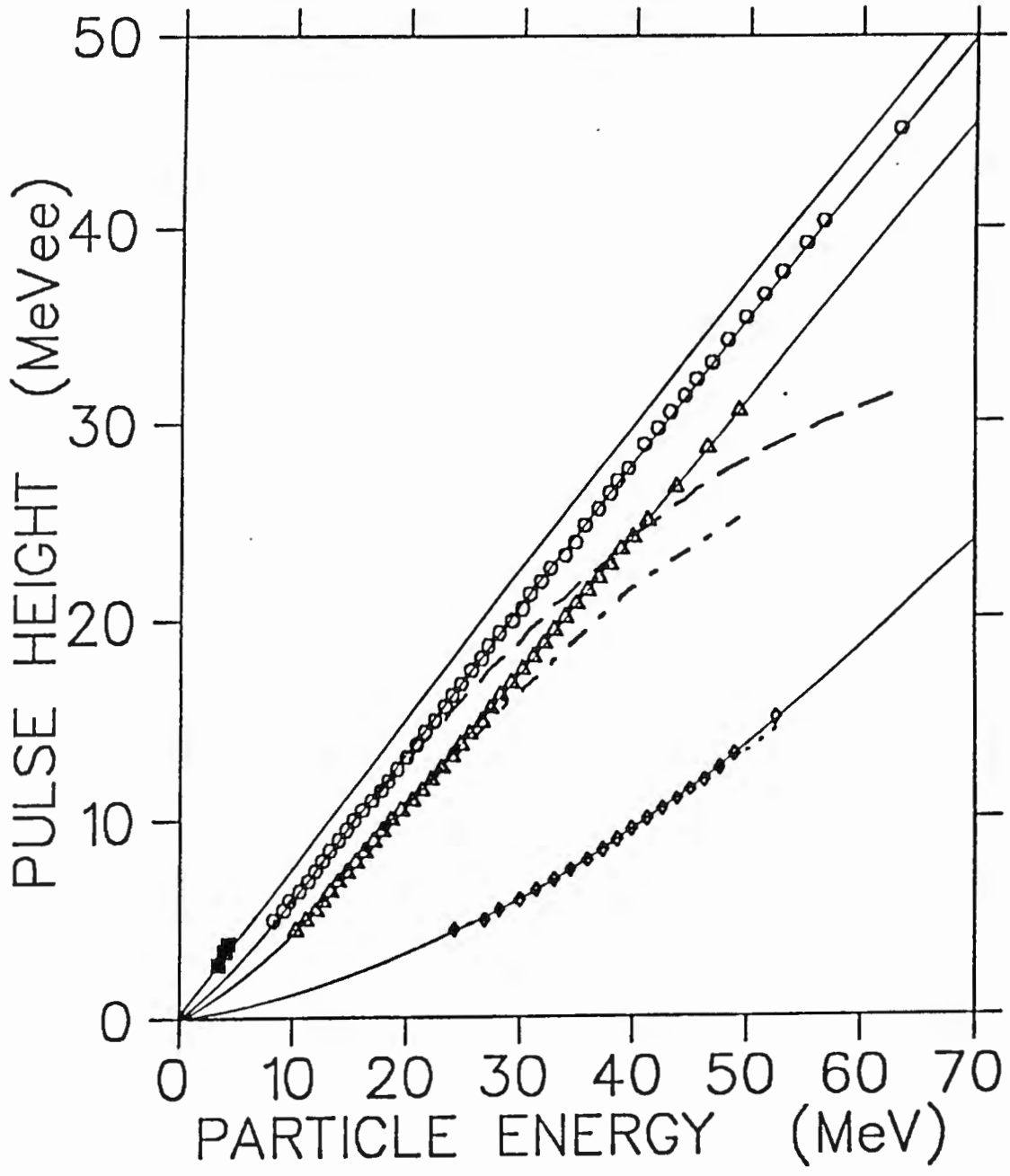

Figure 4.6 Measurements of the scintillator response (pulse height) in units of equivalent electron energy (MeVee) as a function of charged particle energy for (■) electrons, (○) protons, (▲) deuterons and (◇) alphas. The proton, deuteron and alpha data have been corrected for the effect of space charge saturation. The solid curves show the responses calculated from the Birks relation (see text) and the dashed curves show the positions of the uncorrected data (see figure 4.3).

B = 0.0147 ± 0.0001 g.cm^{-2}.MeV^{-1}. It can be seen in figure 4.4 that the Birks curves fit the saturation-corrected measurements extremely well, thus lending confidence to the procedures used to correct for space charge saturation. The dashed curves in figure 4.6 represent the data before the space charge saturation correction was applied.

(b) COMPARISON WITH OTHER WORK.

Plotted in figure 4.7 are the proton response data measured in this work for L < 30 MeVee - corrected for space charge saturation - together with the following other measurements of the response of NE213 to protons (all unnormalised and in units of MeVee): Smith (Sm64); Verbinski *et al* (Ve68); and Uwamino *et al* (Uw82). The present data are seen to agree particularly well with the measurements of Smith *et al* and Uwamino *et al*. Also shown in the figure is the curve calculated from equation 4.3 using the value of B = 0.0147 g.cm^{-2}.MeV^{-1} determined from this work.

Madey *et al* (Ma78) measured the light response of NE102, NE224, NE228 and NE228A scintillators to protons from 2.43 MeV to 19.55 MeV. An empirical relation between the equivalent electron energy, T_e, and the energy, T_p, of heavier charged particles has been presented by Madey of the form:

$$T_e = a\,T_p - b\,[\,1.0 - exp\,(-c\,T_p^{\,d})\,] \qquad (4.4)$$

where the electron energy T_e and the particle energy T_p are in units of MeV and the four coefficients are chosen to fit the data. These coefficients were determined empirically by fitting equation 4.4 independently to the proton, deuteron and alpha response measurements of this work. Listed in table III are these coefficients for protons, deuterons and alphas. These provided equally good fits (to within 5% overall) of equation 4.4 to the measured scintillator response data as the Birks relation. Also listed in table III are the coefficients determined by Cecil *et al* (Ce79) by fitting equation 4.4 to the scintillator response to protons measured for NE213 by Verbinski *et al* (Ve68)

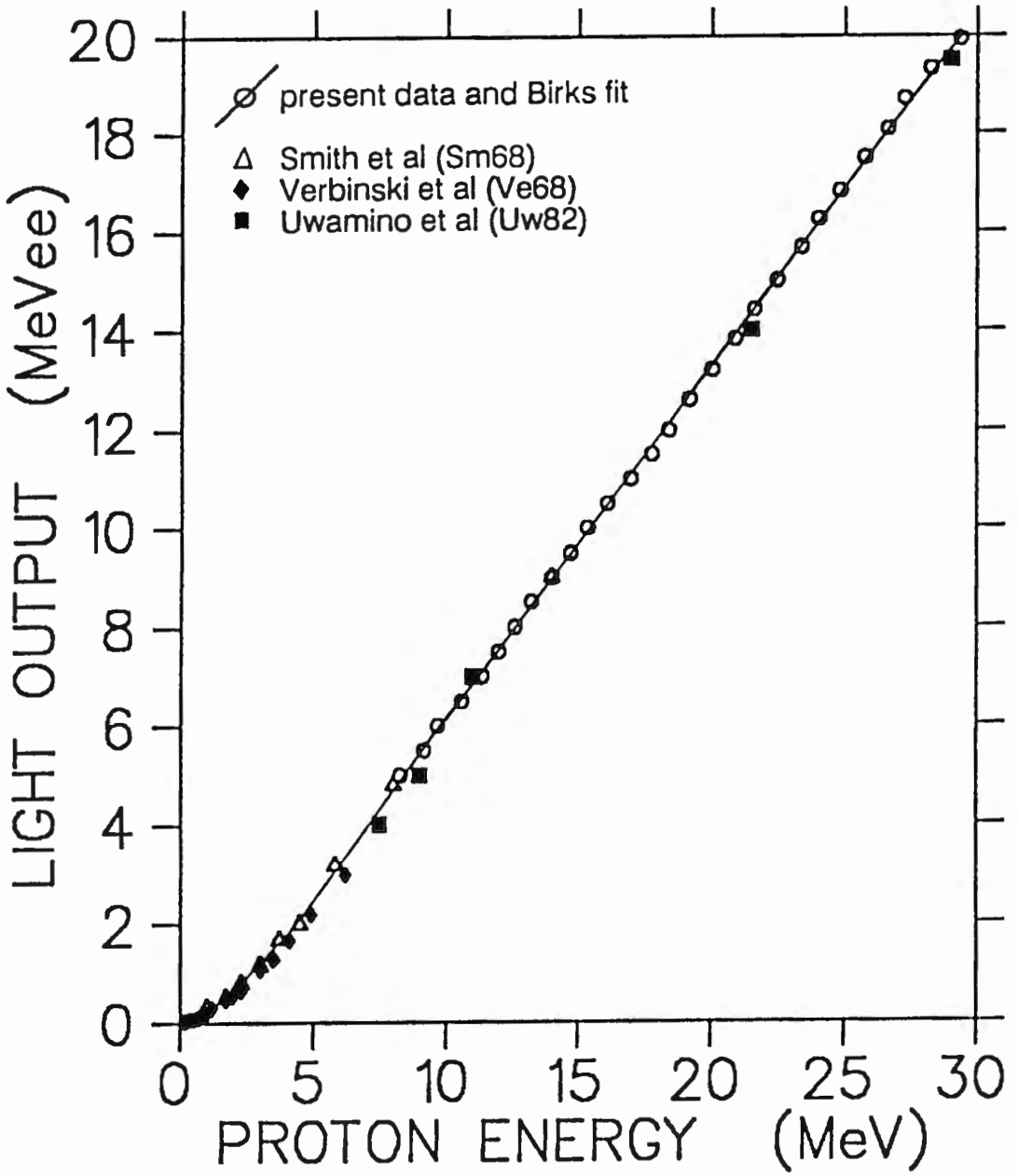

Figure 4.7 Measurements of the scintillator response (pulse height) to protons in units of equivalent electron energy (MeVee) to protons as a function of proton energy. The solid curve shows the proton response calculated from the Birks relation (equation 4.3) using B = 0.0147 g.cm^{-2}.MeV^{-1}. Also shown are the (unnormalised) data of Smith et al, Verbinski et al and Uwamino et al.

and Czirr *et al* (Cz64). Cecil also fitted equation 4.4 to the calculations of Gooding and Pugh (Go60) of the response of NE102 to alphas (figure 1.1), providing the recommended coefficients for alphas listed in table III.

In summary, this work has demonstrated that response data for protons, deuterons and alphas may readily be derived from *L-S* spectra, measured using monoenergetic or quasi-monoenergetic neutrons, resolved into charged particle components by pulse shape discrimination. The data obtained are well described by the Birks formula and give the value of $B = 0.0147$ g.cm^{-2}.MeV^{-1}.

PARTICLE	COEFFICIENT				
	a	*b*	*c*	*d*	
protons	0.77	2.02	0.14	0.88	present work
deuterons	0.69	3.01	0.12	0.95	
alphas	0.42	7.01	0.063	1.03	
protons	0.83	2.82	0.25	0.93	(Ce79)
alphas	0.41	5.90	0.065	1.01	

Table III Coefficients in the light response function (equation 4.4) of Madey et al (Ma78) *for protons, deuterons and alphas in NE213 as measured in this work. Also listed are the measurements of Cecil et al* (Ce79) *for protons and alphas.*

CHAPTER 5

THE RESPONSE FUNCTION OF THE DETECTOR FOR 63 MeV NEUTRONS

There are two main components of the neutron response function or lineshape as measured by an organic scintillator. Firstly, a component due to protons recoiling from $^{1}H(n,n)^{1}H$ elastic scatters; and secondly, the component from charged particles released in neutron-induced carbon reactions. Shown in figure 5.1 is the neutron lineshape for the 5 cm (diameter) by 5 cm cylindrical NE213 detector measured at E_n = 63 MeV together with its components, distinguished by pulse shape discrimination, arising from the detection of protons (released from n-p elastic scatters and n-^{12}C interactions), deuterons and alphas.

A number of Monte Carlo codes have been written (see section 1.4) mainly for the purpose of predicting the neutron detection efficiencies of organic scintillators under different experimental conditions. Accurate measurements of the charged particle components of neutron lineshapes are necessary to test the fidelity of the models used by the codes to simulate the intractions in the scintillator.

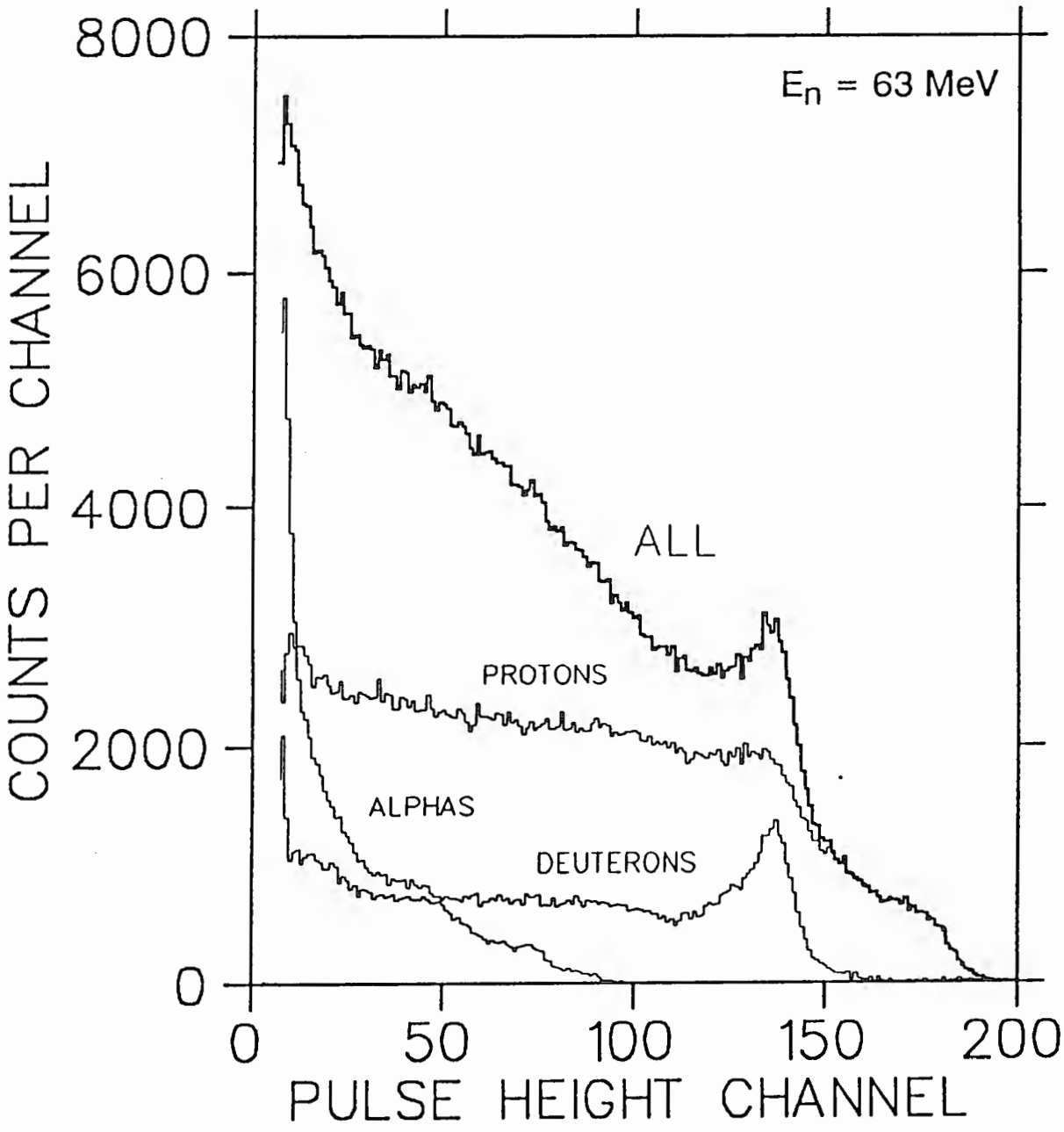

Figure 5.1 Response function (lineshape) of a 5 cm (diameter) x 5 cm NE213 liquid scintillator measured for incident neutrons of energy 63 MeV. Also shown are the components of the lineshape, identified by pulse shape discrimination, to arise from the detection of protons, deuterons and alphas respectively.

Neutron lineshapes were measured at incident neutron energies in the range 15-63 MeV (figure 3.3). The lineshape measured at E_n = 63 MeV has been selected for critical analysis due to the good counting statistics at this energy and to provide information for the n-p radiative capture experiment. Most of the discussion in this chapter may, nevertheless, also be applied to the lineshapes measured at E_n < 63 MeV.

5.1 THE PROTON COMPONENT

Figure 5.2 shows the proton pulse height spectrum measured at E_n = 63 MeV obtained by setting a corridor bordering the proton locus on the *L-S* two parameter spectrum (figure 3.1) as discussed in section 3.2. The upper energy limit for protons released in n-^{12}C reactions, at the position of the $^{12}C(n,p)^{12}B_{gs}$ peak (50.7 MeV), is indicated in the figure.

A computer code, *SCINFUL*, has recently been written by Dickens (Di88) which simulates the light output of an organic scintillator for incident neutrons of energies between 0.1 and 80 MeV. The neutron-induced breakup of ^{12}C into final reaction channels having two, three or four outgoing charged particles has been simulated and the code provides numerical yields of charged particles as a function of charged particle energy, following the breakup of the ^{12}C nucleus. The charged particle pulse height spectra measured in this work have been compared with the charged particle spectra predicted by *SCINFUL*.

(a) THE $^1H(n,n)^1H$ SCATTERING COMPONENT

In order to compare with the proton spectrum predicted by *SCINFUL*, the n-^{12}C reaction component was unfolded from the n-p elastic scattering component of the proton pulse height spectrum measured at E_n = 63 MeV. This was achieved by using a Monte Carlo code (He91) to simulate the n-p

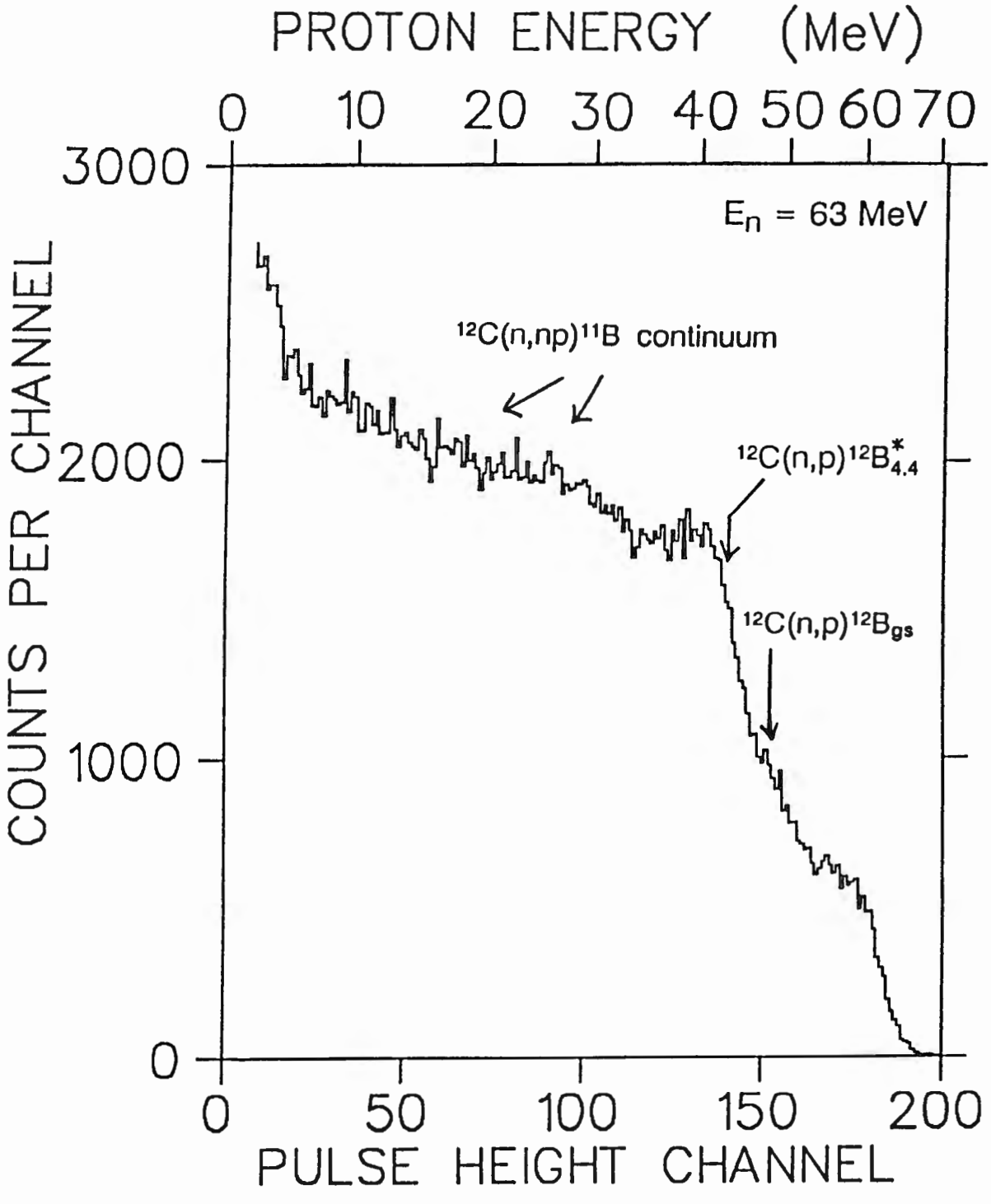

Figure 5.2 Pulse height spectrum, measured by 5 cm (diameter) x 5 cm NE213 liquid scintillator at E_n = 63 MeV, for events identified as protons by pulse shape discrimination. These events include protons released in n-^{12}C reactions and those recoiling from $^1H(n,n)^1H$ scatterings (see figure 5.4).

elastic scattering pulse height spectrum for this scintillator at E_n = 63 MeV. The code was also used to investigate the effect of protons escaping from the scintillator.

For incident neutron energies below 10 MeV, the energy spectrum of recoil protons from n-p elastic scattering can be regarded, to a good approximation, as isotropic in the centre-of-mass system. As E_n increases beyond 10 MeV, p-wave and higher order scattering becomes significant and the energy spectrum becomes increasingly forward-backward peaked (see figure 1.5). Gammel has suggested the following empirical formula (Ga63) for the n-p elastic scattering differential cross section, $\sigma_{nn}(\theta,E_n)$, which is reliable for 1 MeV $< E_n <$ 90 MeV on the assumption that $\sigma_{nn}(\theta,E_n)$ is symmetrical about 90° in the centre-of-mass system. For a centre-of-mass angle, θ, and $^1H(n,n)^1H$ total cross section σ_{nn} (St64), the differential cross section, $\sigma_{nn}(\theta,E_n)$, is given by:

$$\sigma_{nn}(\theta,E_n) = \frac{\sigma_{nn} \quad (1 + b\cos^2\theta)}{4\pi \quad (1 + 1/3\, b)} \tag{5.1}$$

where $b = 2\,(E_n/90)^2$ and E_n in MeV.

Considering the case of 63 MeV neutrons incident on a 5 cm x 5 cm cylindrical NE213 scintillator, the energy spectrum for protons recoiling from n-p elastic scatterings will have the form as shown in figure 5.3(a) as predicted by equation 5.1. For organic scintillators, such as NE213, the pulse height spectrum of detected scintillations from these protons, assuming that no protons escape from the detector, will be as shown in (b) introducing the scintillator response to protons as discussed in section 4.2, but neglecting the finite pulse height resolution of the scintillator. The latter will distribute the events at each pulse height into a Gaussian distribution with a width proportional to the square root of the pulse height, as expected from photon counting statistics. This will smear all sharp edges and peaks as indicated in (c). The space charge saturation phenomenon, present in this work at the

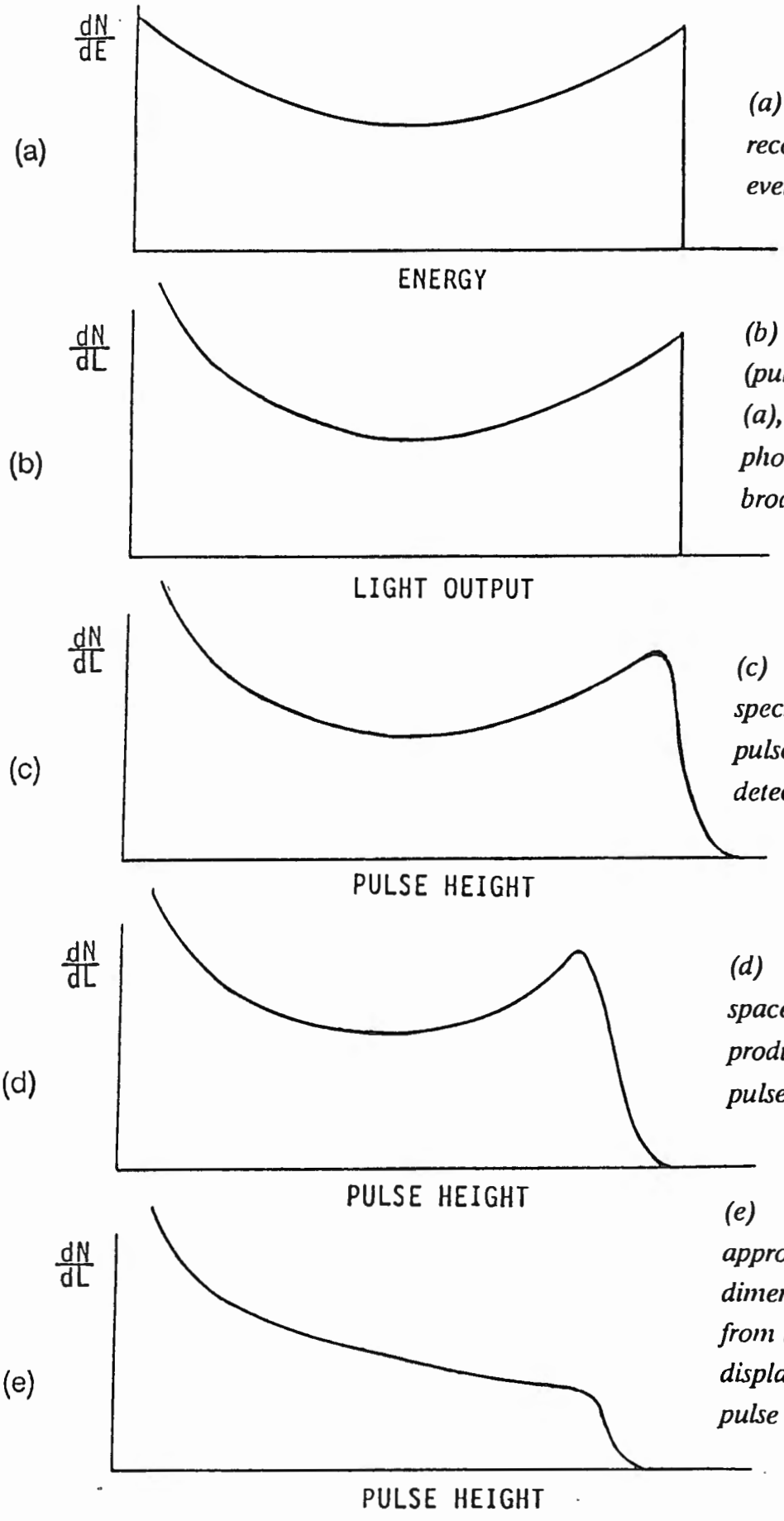

(a) Energy spectrum of protons recoiling from n-p elastic scattering events at E_n = 63 MeV.

(b) Scintillator light output (pulse height) for the spectrum in (a), above, not including photomultiplier resolution broadening.

(c) Scintillator pulse height spectrum introducing the finite pulse height resolution of the detector.

(d) The effect of photomultiplier space charge saturation is to produce a false rise near the upper pulse height limit.

(e) As the proton range approaches the scintillator dimensions , many protons escape from the scintillator and are displaced off the recoil proton pulse height spectrum.

Figure 5.3 Schematic spectra illustrating the evolution of the recoil proton pulse height spectrum for the $^1H(n,n)^1H$ process, predicted by the Monte Carlo (He91) *at E_n = 63 MeV.*

higher pulse heights (see section 4.1), will distort the expected linear scintillator response to protons at these higher pulse heights, (d). This has the effect of producing a false enhancement in the spectrum near the upper pulse height limit. Finally, the probability for protons to escape without depositing all of their energy in the scintillator will increase with increasing proton energy. As described earlier in section 3.3, the events associated with escaping protons will be shifted off the proton locus, thus distorting the proton pulse height spectrum, i.e. those events remaining on the axis, to the form shown in figure 5.3(e).

Multiple scattering whereby the same neutron will be involved in more than one interaction as it passes through the scintillator will also distort the pulse height spectrum. This effect will be more prominent at lower neutron energies as also discussed in section 3.3.

Shown in figure 5.4(a) is the pulse height spectrum (curve) for recoil protons associated with n-p elastic scattering, simulated at an incident neutron energy of 63 MeV. The simulated spectrum includes all the features described above (figure 5.3(a)-(e)) and is shown fitted to the upper region of the observed proton pulse height spectrum (histogram), measured at the same neutron energy. Figure 5.4(b) shows the same simulated elastic scattering spectrum, together with the (simulated) spectrum that should be observed if there were no proton escape. This is the same pulse height spectrum that would be recorded using an infinite detector, but ignoring the effect of multiple scattering. The sharp peak at the high pulse height limit is attributed to the p-wave contribution to the n-p elastic scattering differential cross section (see figure 1.5). The effect of space charge saturation of the photomultiplier signal, (see figure 4.3) further steepens this peak to the form shown in figure 5.4(b).

Watson and Graves (Wa74) have explored the effect of proton escape using several different detector shapes and geometries. In particular, neutron lineshapes for the liquid scintillator NE218 were measured for neutron energies in the range 24-61 MeV. The $^{1}H(n,n)^{1}H$ elastic scattering component was simulated by a Monte Carlo and the effect of protons leaving the

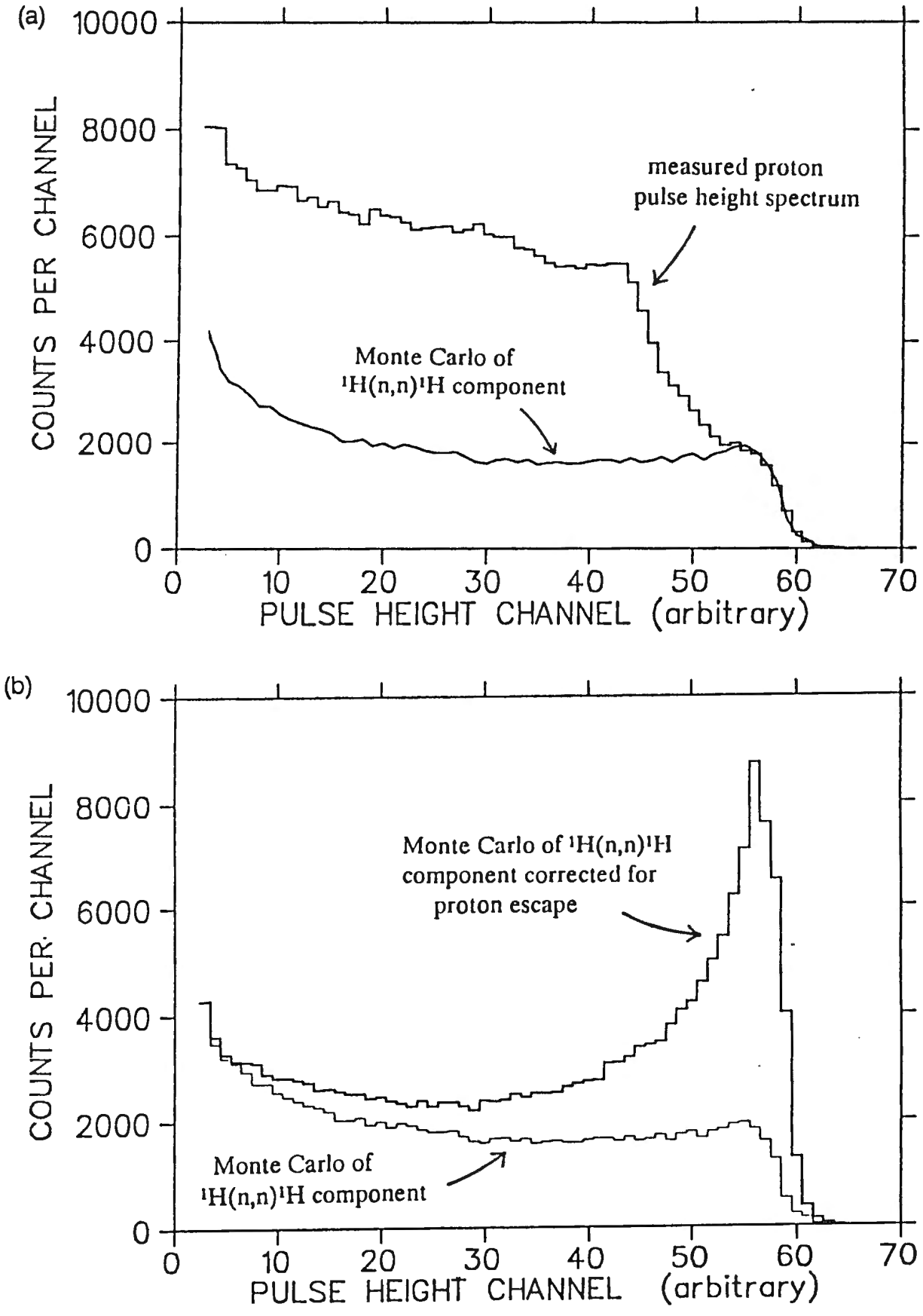

Figure 5.4 *(a) (above) Proton pulse height spectrum (histogram), measured by 5 cm (diameter) by 5 cm NE213 liquid scintillator at E_n = 63 MeV, together with a simulation (curve) of the $^1H(n,n)^1H$ elastic scattering component of the spectrum.*

(b) (below) The simulated n-p elastic scattering component (dashed curve) of the proton pulse height spectrum in (a), above, shown together (solid curve) as would be measured by an infinite detector (no proton escape).

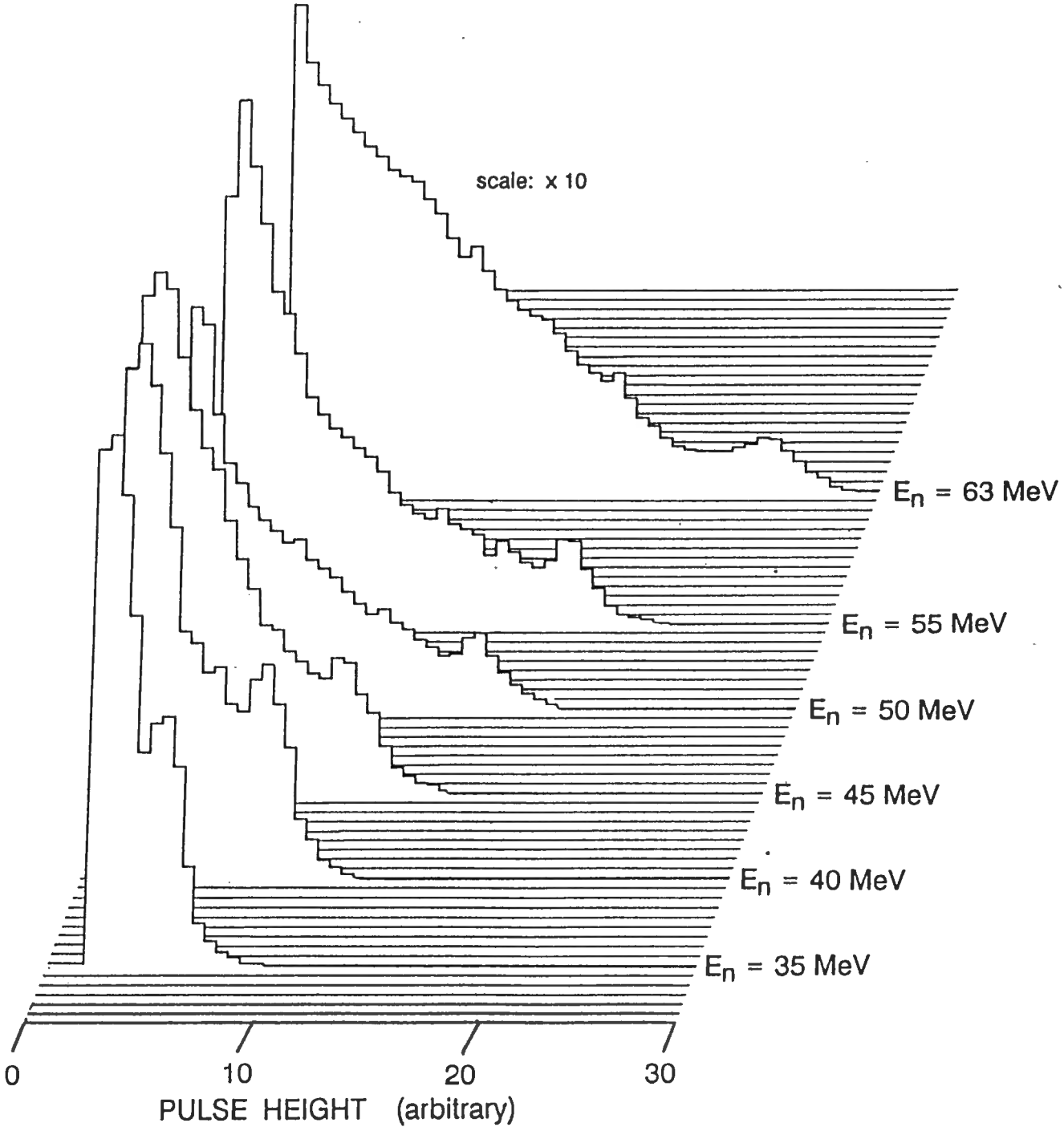

Figure 3.16 Alpha pulse height spectra for different neutron energies for alphas released in the $^{12}C(n,\alpha)^{9}Be$ reaction (see text).

scintillator was investigated. Figure 5.5 shows the measurements and calculations for 61 MeV neutrons incident on a 2.54 cm radius by 7.62 cm long cylindrical capsule of NE218 orientated both axially and radially to the incident neutron beam. It can be seen that the effect of proton escape is more prominent when the detector is in the radial orientation. These results are found to be similar to the present work.

(b) THE n-^{12}C REACTIONS COMPONENT

With reference to the proton pulse height spectrum measured at E_n = 63 MeV (figure 5.2), we note that there is a slight rise near the upper pulse height limit for protons released in n-^{12}C reactions. This is attributed to the transitions to the unresolved ground and 0.95 MeV states of ^{12}B in the reaction ^{12}C(n,p)^{12}B. Also labelled in figure 5.2 is a rise in the spectrum which is attributed to the unresolved 4.44 MeV level in ^{12}B and giant dipole resonance (Fo84).

There is also a large yield from the ^{12}C(n,np)^{11}B reaction as suggested by McNaughton *et al* (Mc75). A broad phase space continuum, labelled in figure 5.2, extending down to the experimental threshold, arises from the detection of the protons released in the ^{12}C(n,np)^{11}B reaction. This is in accordance with the dominance of the ^{12}C(n,np)^{11}B process (90% of total (n,p) cross section at E_n = 90 MeV) as observed by Kellogg (Ke53). In addition, McNaughton found a better agreement between his measurements and calculations of the neutron detection efficiency of an organic scintillator, by including the ^{12}C(n,np)^{11}B rather than the ^{12}C(n,p)^{12}B channel in his Monte Carlo. It should be remembered that contributions to the measured pulse height spectrum from protons released in ^{12}C(n,2np)^{10}B, ^{12}C(n,2n2p)^{9}Be, and other reactions (see table I) might also be significent (Ke53).

Shown in figure 5.6(a) are the differential cross sections for the ^{12}C(n,p)^{12}B and ^{12}C(n,d)^{11}B reactions (Mc75) measured at E_n = 56 MeV together with measurements for the charge symmetric ^{12}C(p,d)^{11}C reaction (Ro75) at the same energy. It can be seen that these reactions, as for the n-p elastic

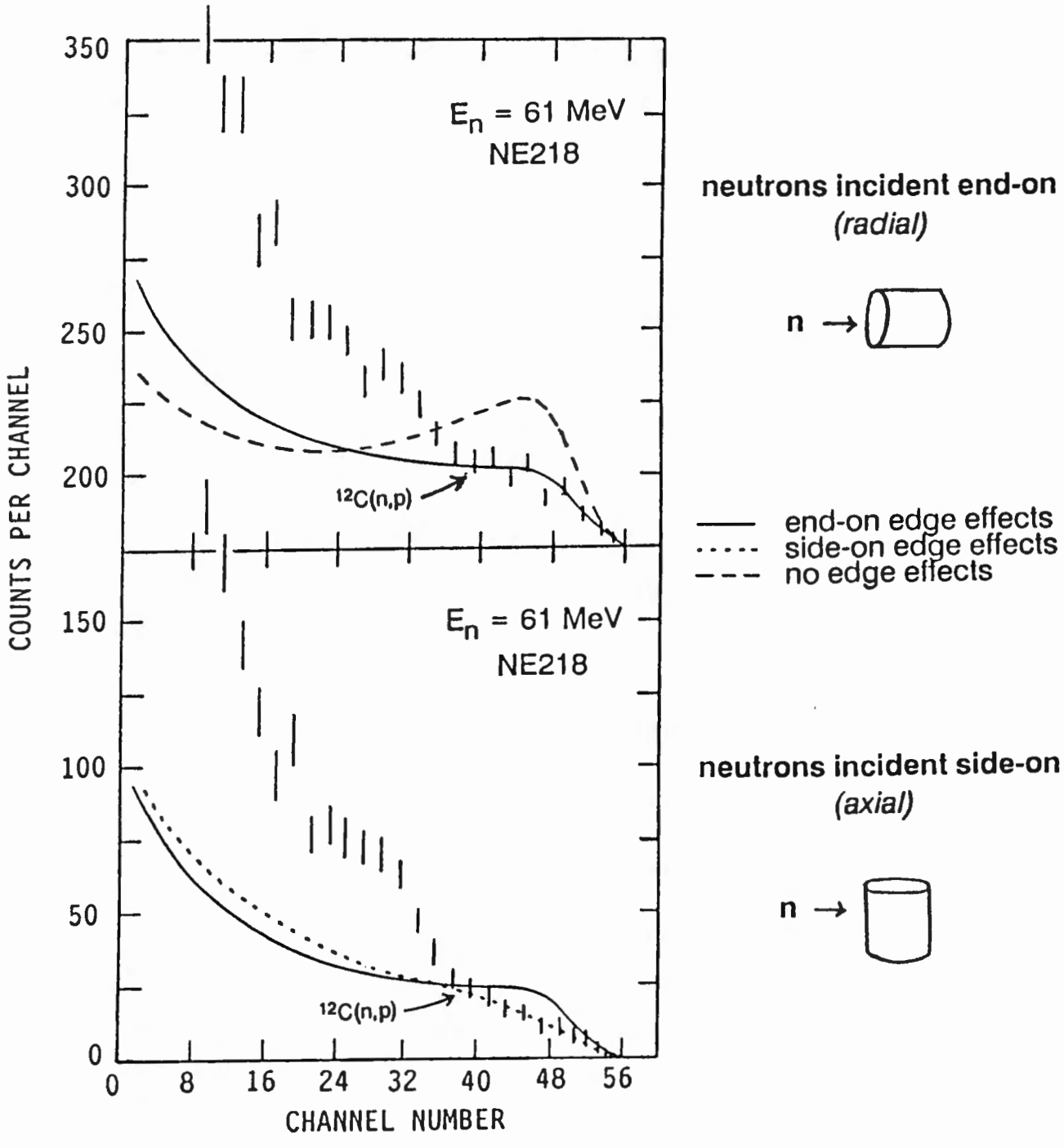

Figure 5.5 Experimental and calculated recoil proton pulse height spectra (Wa74) *for 61 MeV neutrons incident on a 2.54 cm radius by 7.62 cm long cylindrical capsule of NE218, orientated axially in (a), above, and radially in (b), below. The normalization of calculation to experiment is arbitrary. The threshold below which the $^{12}C(n,p)^{12}B$ reaction can contribute events is indicated in each spectrum.*

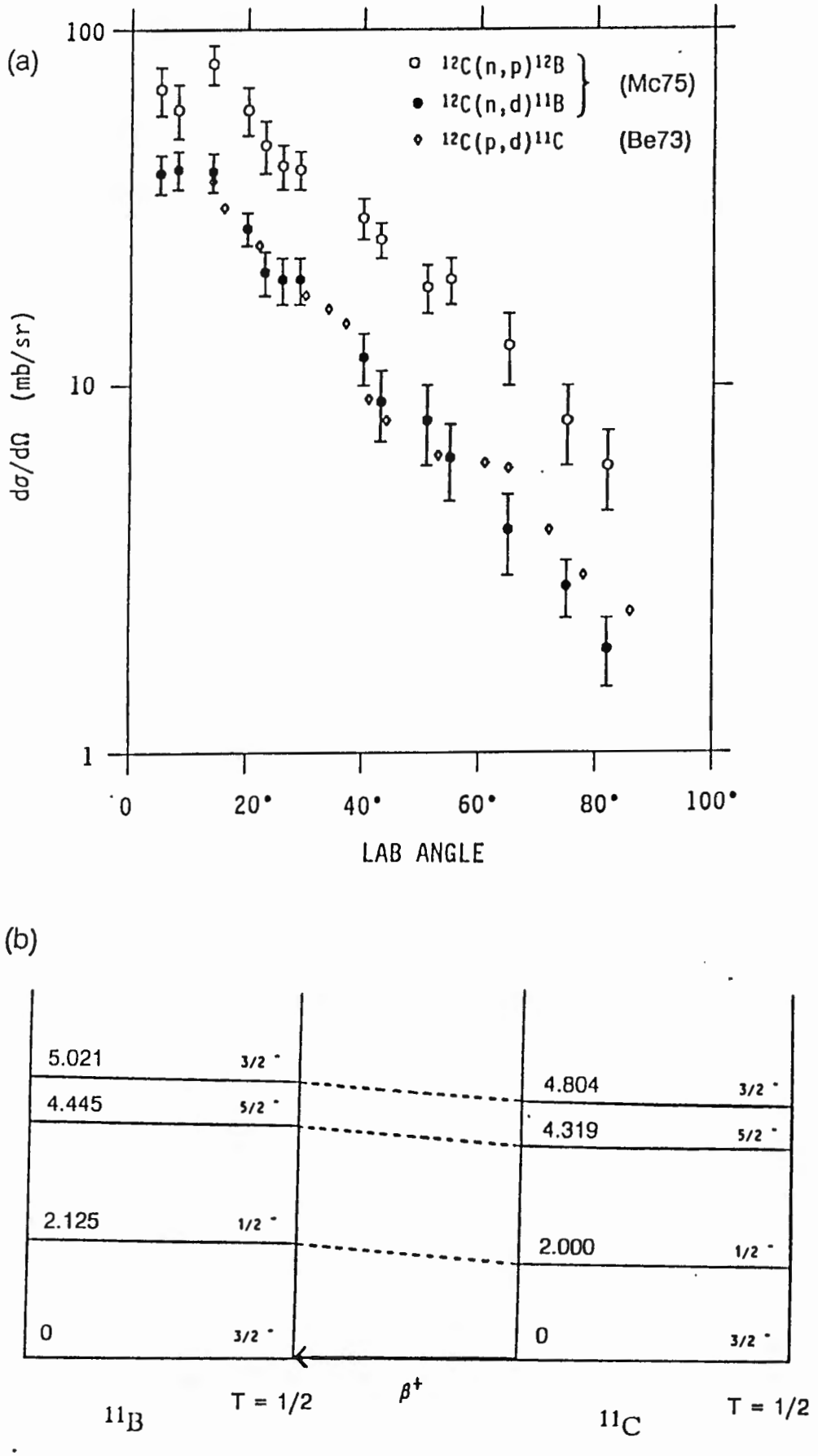

Figure 5.6 *(a) (above) Differential cross sections, measured at* E_n = 56 *MeV, for the reactions* $^{12}C(n,p)^{12}B$ *and* $^{12}C(n,d)^{11}B$ *(Mc75); and* $^{12}C(p,d)^{11}C$ (Be73).

(b) (below) The first few energy levels (Aj84) *of the mirror nuclei* ^{11}B *and* ^{11}C.

scattering process, are strongly forward peaked in the laboratory frame at these energies. This implies that the majority of escaping protons will leave the rear of the scintillator, as opposed to the sides. The first few energy levels of the ^{11}B and ^{11}C mirror nuclei are illustrated in figure 5.6(b).

(c) COMPARISON WITH *SCINFUL*.

The Monte Carlo code of Dickens (Di88) was run under the experimental conditions used in this work at E_n = 63 MeV. Energy spectra for outgoing protons (figure 5.7(a)) and deuterons (figure 5.9(a)) released in n-^{12}C reactions were obtained.

The predicted proton energy spectrum (figure 5.7(a)) was transformed to a pulse height spectrum using the scintillator response to protons as measured in this work (section 4.2). This pulse height spectrum was then convoluted with the same detector resolution function used in the simulation of the n-p elastic scattering component of the measured pulse height spectrum (figure 5.4), to give the curve shown in figure 5.7(b). The corresponding spectrum obtained from the present work by subtracting the simulated n-p elastic scattering component (figure 5.4(a)) from the proton pulse height spectra measured at E_n = 63 MeV, is shown by the histogram in figure 5.7(b). Also shown in figure 5.7(b) is the proton pulse height spectrum simulated by *SCINFUL*. In order to make a comparison, the two spectra were normalized at the position indicated in figure 5.7(b). It can be seen the overall agreement at the higher pulse heights is good, but the code does not model the observed $^{12}C(n,np)^{11}B$ continuum as successfully.

5.2 THE DEUTERON COMPONENT

The deuteron pulse height spectrum measured at E_n = 63 MeV is shown in figure 5.8. As discussed in section 4.1(c), the peak is attributed to the transition to the ground state of ^{11}B in the reaction $^{12}C(n,d)^{11}B$ (Me67). This

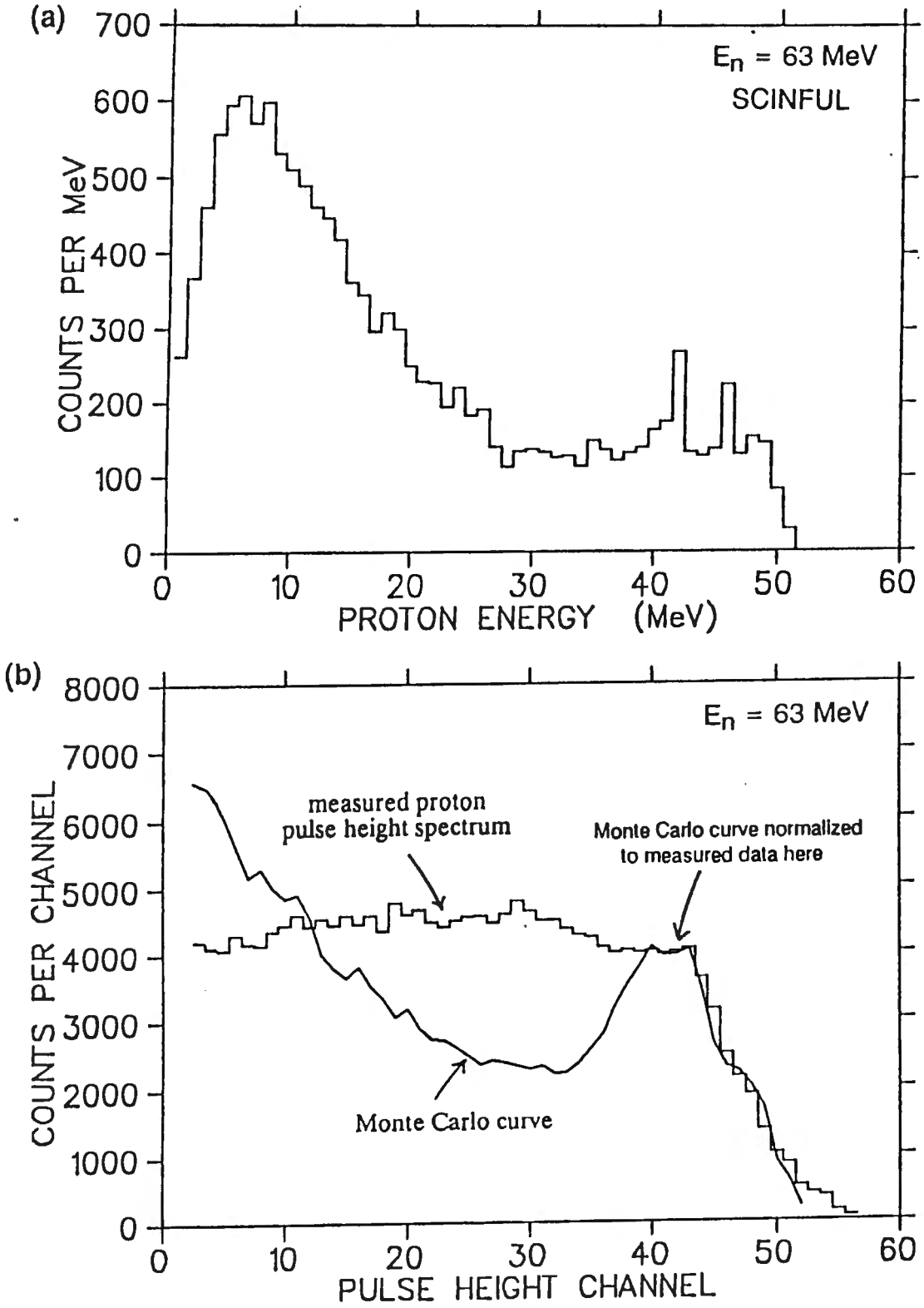

Figure 5.7 (a) (above) Energy spectrum for neutron induced proton production from ^{12}C at E_n = 63 MeV, as simulated by SCINFUL (Di88), *for a 5 cm (diameter) by 5 cm cylinder of NE213.*

(b) (below) The n-12C component of the proton pulse height spectrum (histogram) measured at E_n = 63 MeV, and the predicted pulse height spectrum of the SCINFUL *code, from (a), above. For comparison, the two spectra have been normalised at the position indicated.*

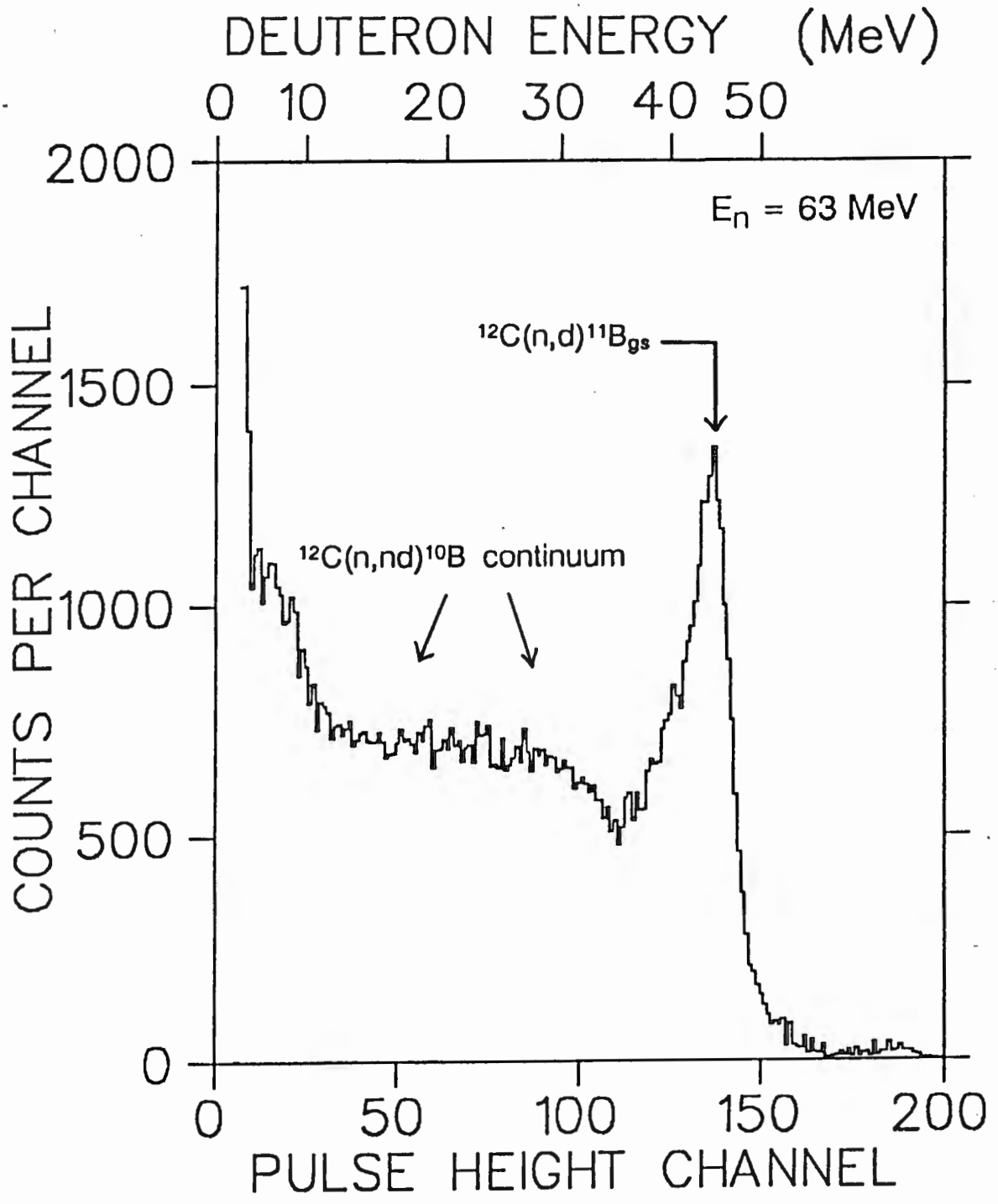

Figure 5.8 Pulse height spectrum, measured by 5 cm (diameter) by 5 cm NE213 liquid scintillator at E_n = 63 MeV, for events identified as deuterons by pulse shape discrimination.

ground state transition is also the most important for the $^{12}C(p,d)^{11}C$ reaction (Co60).

There is also evidence of a phase space continuum (labelled in figure 5.8) arising from the detection of the deuteron released in the $^{12}C(n,nd)^{10}B$ reaction which clearly forms a major contribution to the total deuteron yield.

Shown in figure 5.9(a) is the deuteron energy distribution as was simulated by the *SCINFUL* code (Di88) at E_n = 63 MeV. By following a similar procedure as described for the proton spectrum (section 5.1(c)), a simulated deuteron pulse height spectrum was obtained. This is shown in figure 5.9(b) together with the deuteron pulse height spectrum measured at E_n = 63 MeV. The two spectra were normalised at the ^{11}B peak for comparison and once again the observed (n,nd) continuum appears to have been underestimated by the Monte Carlo.

5.3 THE ALPHA COMPONENT

There are indications (Ho78) that the nucleons are sometimes grouped together in clusters in the nucleus; and of all possible clusters, the alpha particle is the most likely because of its high symmetry and tight binding. There emerge regions of higher density corresponding in number to the number of alphas needed to construct that nucleus : three for ^{12}C, four for ^{16}O and so on. It then follows that, to some extent, these nuclei can be thought of as three or more alpha particles bound together, and many properties of these nuclei may be accounted for on this assumption. The clustering of alpha particles will affect the cross sections of alpha-producing n-^{12}C reactions as at higher energies, the alphas will be emitted from a local "hot spot" on the nuclear surface. Such reactions are particularly sensitive to this grouping of alphas and analysis of their cross sections give estimates of the alpha-formation probability.

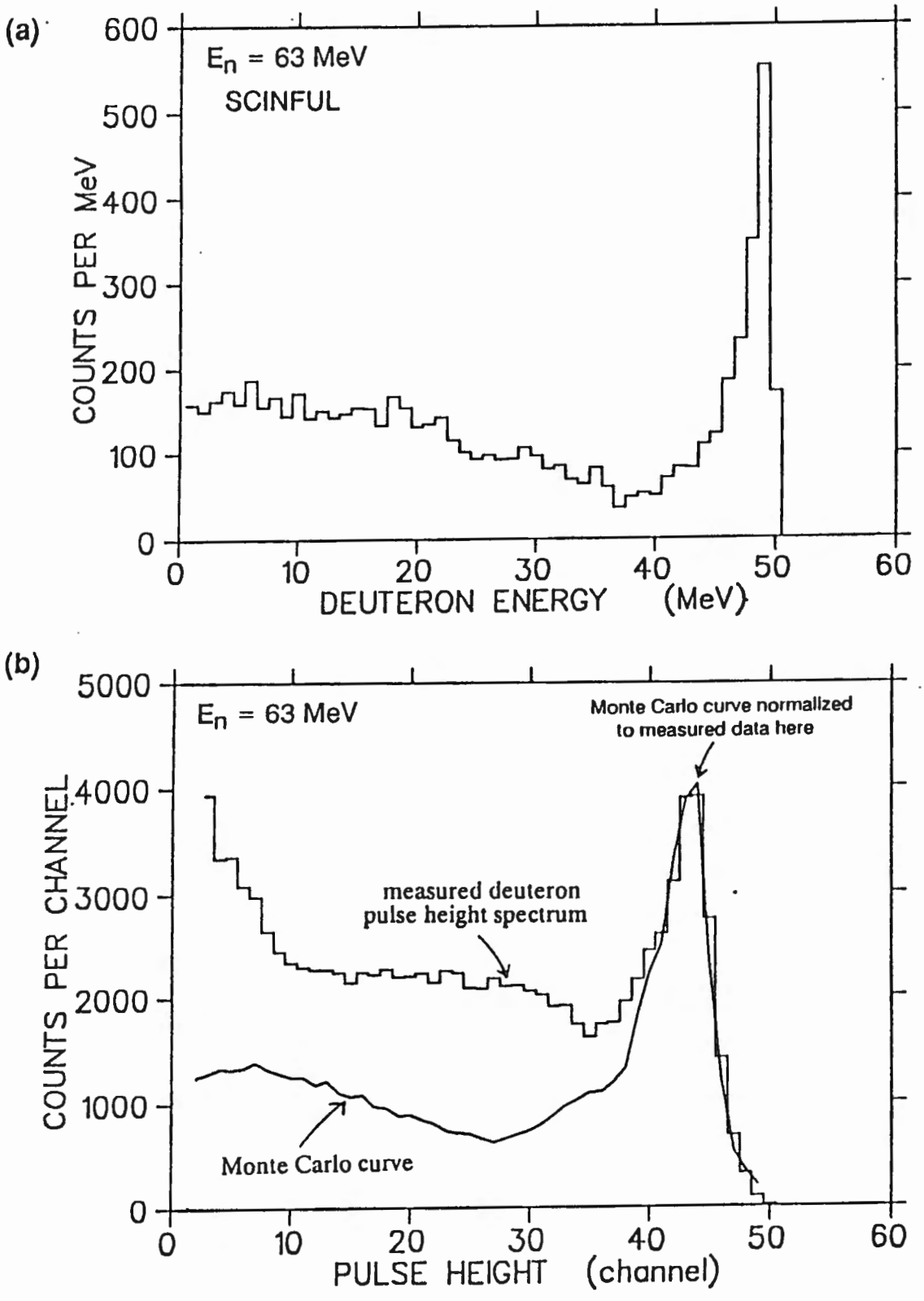

Figure 5.9 *(a) (above) Energy spectrum for neutron induced deuteron production from ^{12}C at E_n = 63 MeV, as simulated by* SCINFUL (Di88), *for a 5 cm (diameter) by 5 cm cylinder of NE213.*

(b) (below) The deuteron pulse height spectrum (histogram) measured at E_n = 63 MeV, and the predicted pulse height spectrum of the SCINFUL *code, from (a), above. For comparison, the two spectra have been normalised at the position indicated.*

Alpha producing reactions are major contributors to the total n-^{12}C cross section above 14 MeV (La75), where the two dominant reactions yielding alpha particles are the ^{12}C(n,α)^{9}Be and ^{12}C(n,n')3α.

There is essentially only one mechanism yielding a single alpha particle and that is the ^{12}C(n,α)^{9}Be reaction. This reaction, which has a Q-value of - 5.79 MeV, may be understood as the incident neutron knocking out an alpha from the ^{12}C and leaving the ^{9}Be in its ground state. Excitation of the ^{9}Be to higher states will lead to a further breakup into two alphas and a neutron.

The situation regarding the triple alpha decay process ^{12}C(n,n')3α (Q-value = -7.65 MeV) is less straightforward and it is difficult to separate overlapping reaction channels. With reference to figure 5.10, the possibilities open as mechanisms of the ^{12}C(n,n')3α reaction are:

(i) ^{12}C (n,α) ^{9}Be* (n',^{8}Be* (2α))
(ii) ^{12}C (n,α) ^{9}Be* (α,^{5}He* (n',α))
(iii) ^{12}C (n,^{5}He (n',α)) ^{8}Be* (2α)
(iv) ^{12}C (n,n') ^{12}C* (α,^{8}Be* (2α))
(v) ^{12}C (n,n' α) 2α (four-body breakup)

In all of these reaction paths, the kinetic energy, 55.6 MeV, available for an incident neutron energy of 63.3 MeV, is shared by the reaction products.

It has been found (An83) that there is a negligable contribution of the sequential decays including ^{5}He (i.e. (ii) and (iii) above) to the total ^{12}C(n,n')3α cross section at E_n = 35 MeV. The sequential decay ^{12}C (n,α) ^{9}Be* (n',^{8}Be* (2α)) contributes about 10% at about E_n = 14.4 MeV (An75) and even less at 18.2 MeV (An76). This is supported by the data available on the charge symmetric process ^{12}C(p,p')3α where for E_p = 58 MeV (Ep69) the reaction was also found to proceed mainly by sequential decay via excited states of ^{12}C. Therefore the ^{12}C(n,n')3α reaction may be understood to proceed appreciably as the sequential decay via excited states of ^{12}C, i.e. (iv) above. Figure 5.11 is an energy level diagram of the

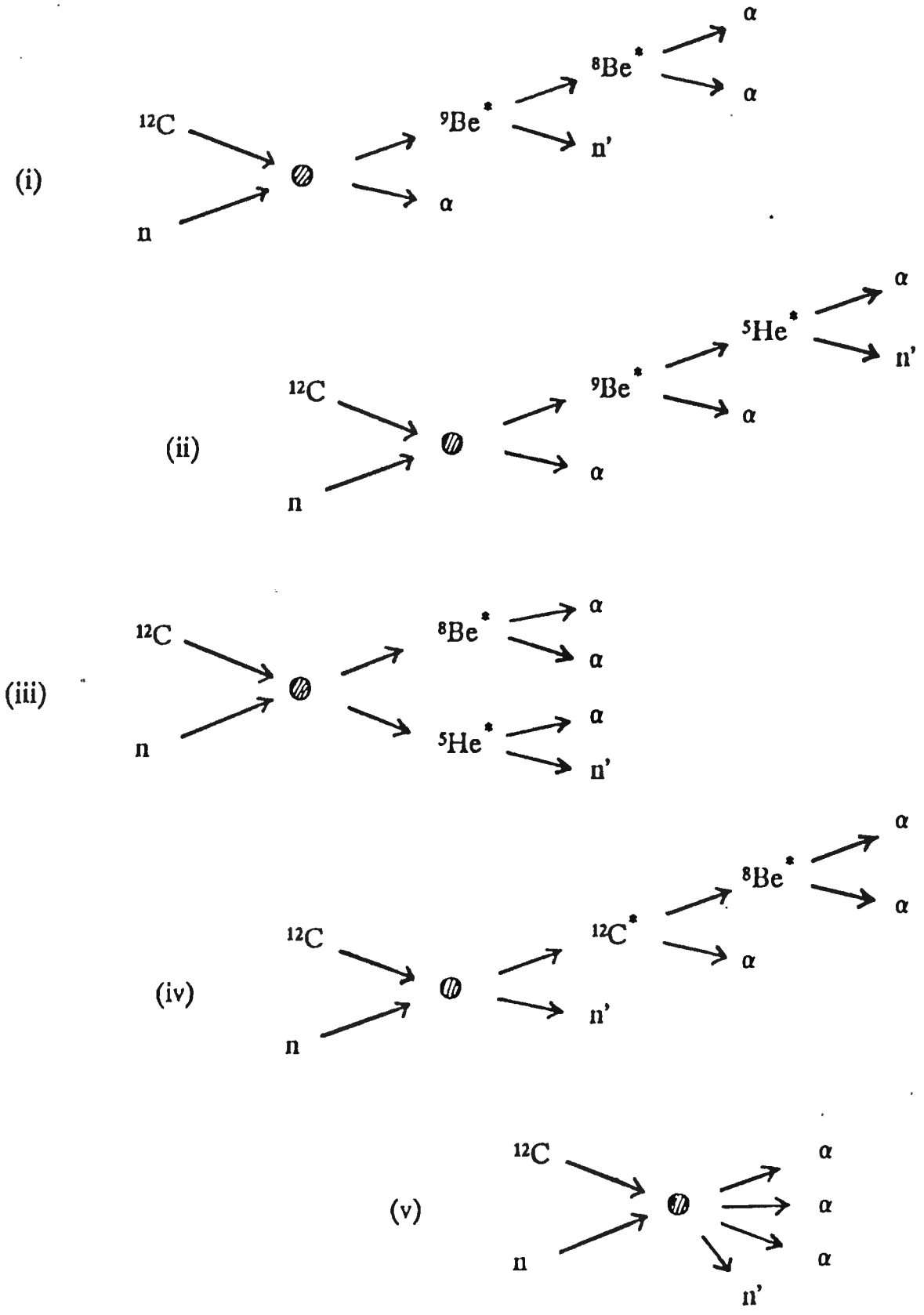

Figure 5.10 Diagrams representing neutron induced sequential alpha decay of ^{12}C via: (i) $^{9}Be^{*}$ and $^{8}Be^{*}$; (ii) $^{9}Be^{*}$ and $^{5}He^{*}$; (iii) $^{8}Be^{*}$ and $^{5}He^{*}$; and (iv) $^{12}C^{*}$ and $^{8}Be^{*}$. Also shown is the four body break-up, (v).

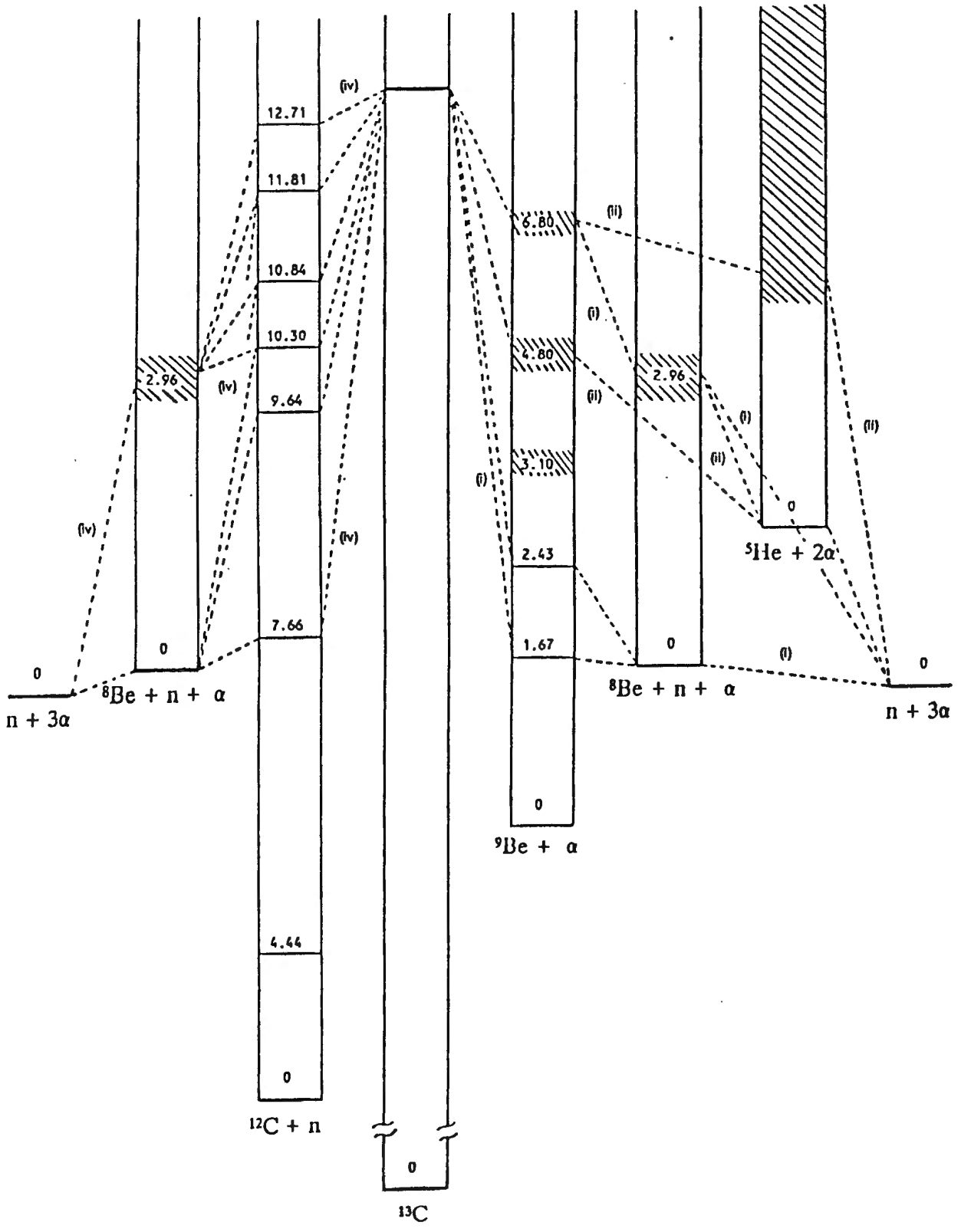

Figure 5.11 Diagrammatic representation of the energies levels of the participating nuclei in the neutron-induced sequential alpha breakup of ^{12}C, showing the possible reaction paths (refer to text). All energies shown are in units of MeV.

participating nuclei in the $^{12}C(n,n')3\alpha$ sequential decay. The reaction branches (i) to (vi) are labelled in the diagram.

Figure 5.12 shows a contour plot of the alpha region of the *L-S* two parameter spectrum (figure 3.1) measured at E_n = 63 MeV, which displays the partial separation of the contributions from the two competing alpha reactions. Any scintillation processed by the detection system will be the sum of the scintillations produced by all the outgoing charged particles in an event. It is then expected that the scintillator light output for an alpha of energy 3E (released in an $^{12}C(n,\alpha)^9Be$ event) will be greater than that for three particles of energy E, outgoing from a $^{12}C(n,n')3\alpha$ interaction. However, the upper pulse height limit of the $^{12}C(n,\alpha)^9Be$ locus is seen to lie at a slightly lower pulse height than the $^{12}C(n,n')3\alpha$ locus. This suggests that one of the outgoing alphas from the $^{12}C(n,n')3\alpha$ reaction will often be released with a large proportion of the available energy, while the rest will be shared between the remaining two. If this is the case, it would explain why the upper limit of the $^{12}C(n,n')3\alpha$ locus lies at a higher pulse height. Another contributing factor is that the recoiling ^9Be residual nucleus from a $^{12}C(n,\alpha)^9Be$ reaction removes some of the energy (about 8% for the alpha outgoing in the forward direction); and as it is heavily ionizing, will contribute a negligable amount towards the scintillation pulse height for the event.

The pulse shape for a signal from an (n,α) event will also be different to that from an $(n,3\alpha)$ event, especially in the region near the upper pulse height limit. The photomultiplier "sees" the ionization from the $(n,3\alpha)$ event as coming from a slightly heavier charged particle as the two lower energy alphas will contribute a large proportion of slow component to the final scintillator light output pulse for the event. This produces the partial separation of the alpha locus seen in figure 5.12.

The summation of the scintillations also causes any structure in the $(n,3\alpha)$ locus, resulting from the decays of specific levels of ^{12}C, to be "smeared" out as the three outgoing alphas, which have a random distribution of energy, cannot be detected separately. There is, however, a slight elevation in the $(n,3\alpha)$

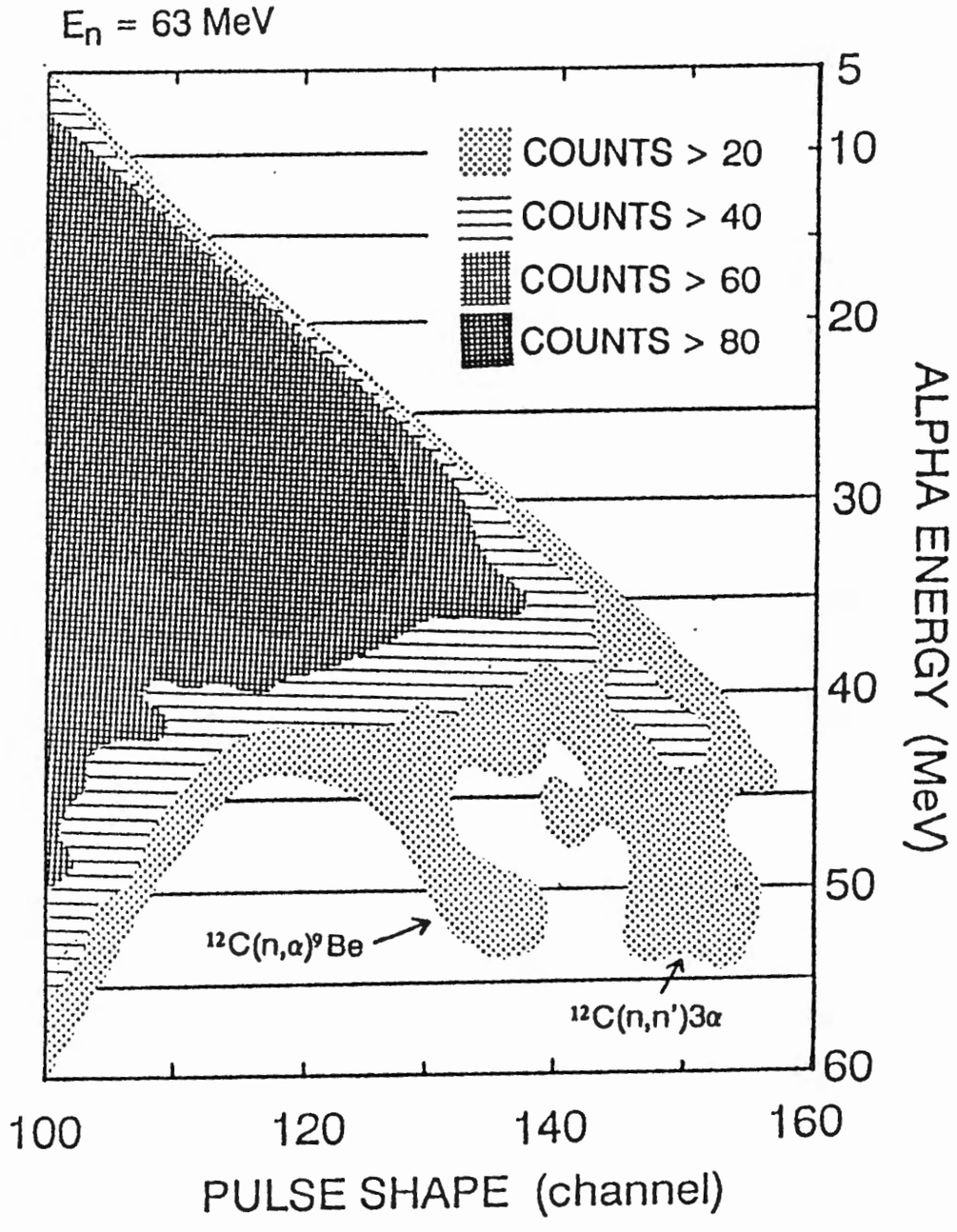

Figure 5.12 Schematic event density plot of counts versus alpha energy and pulse shape channel of the alpha region of the L-S spectrum (figure 3.1). The loci arising from the detection of alphas from $^{12}C(n,\alpha)^9Be$ and $^{12}C(n,n')3\alpha$ are clearly identified. (Refer to the perspective L-S plot (figure 3.1).)

locus at an alpha energy of about 40 MeV, in the region where the 9.64 MeV, 10.30 MeV and higher excited state peaks of ^{12}C are expected.

Shown in figure 5.13 is the alpha pulse height spectrum measured at E_n = 63 MeV for all outgoing alphas. This was obtained by projecting the entire alpha locus in the *L-S* spectrum of figure 5.12 onto the *L*-axis. The spectrum is complex and will depend on whether or not the $^{12}C(n,n')3\alpha$ decay proceeds throught the ground state or first excited state of ^{8}Be; which in turn depends on the level excited in ^{12}C (see figure 5.11). The last two alphas would also be expected to follow some sort of statistical distribution in the centre of mass frame which produces an energy distribution similar to that predicted by phase space considerations. The ^{9}Be ground state peak, associated with the $^{12}C(n,\alpha)^{9}Be$ reaction, is discernable in the figure, although masked by the contribution from the $^{12}C(n,n')3\alpha$ reaction. However, this peak is easily distinguished in the pulse height spectrum for alphas released in $^{12}C(n,\alpha)^{9}Be$ reactions (see section 3.2(b)), the upper pulse height region of which is shown by the dashed line in figure 5.13.

In summary, the lineshape of the detector, measured at E_n = 63 MeV, has been unfolded into pulse height spectra for protons, deuterons and alphas. The n-p elastic scattering component has been separated from the n-^{12}C component by the means of a Monte Carlo. Furthermore, the proton, deuteron and alpha pulse height spectra have been critically analysed, and many of the features described for the response function at E_n = 63 MeV are applicable for the lower neutron energies in the range 20-63 MeV.

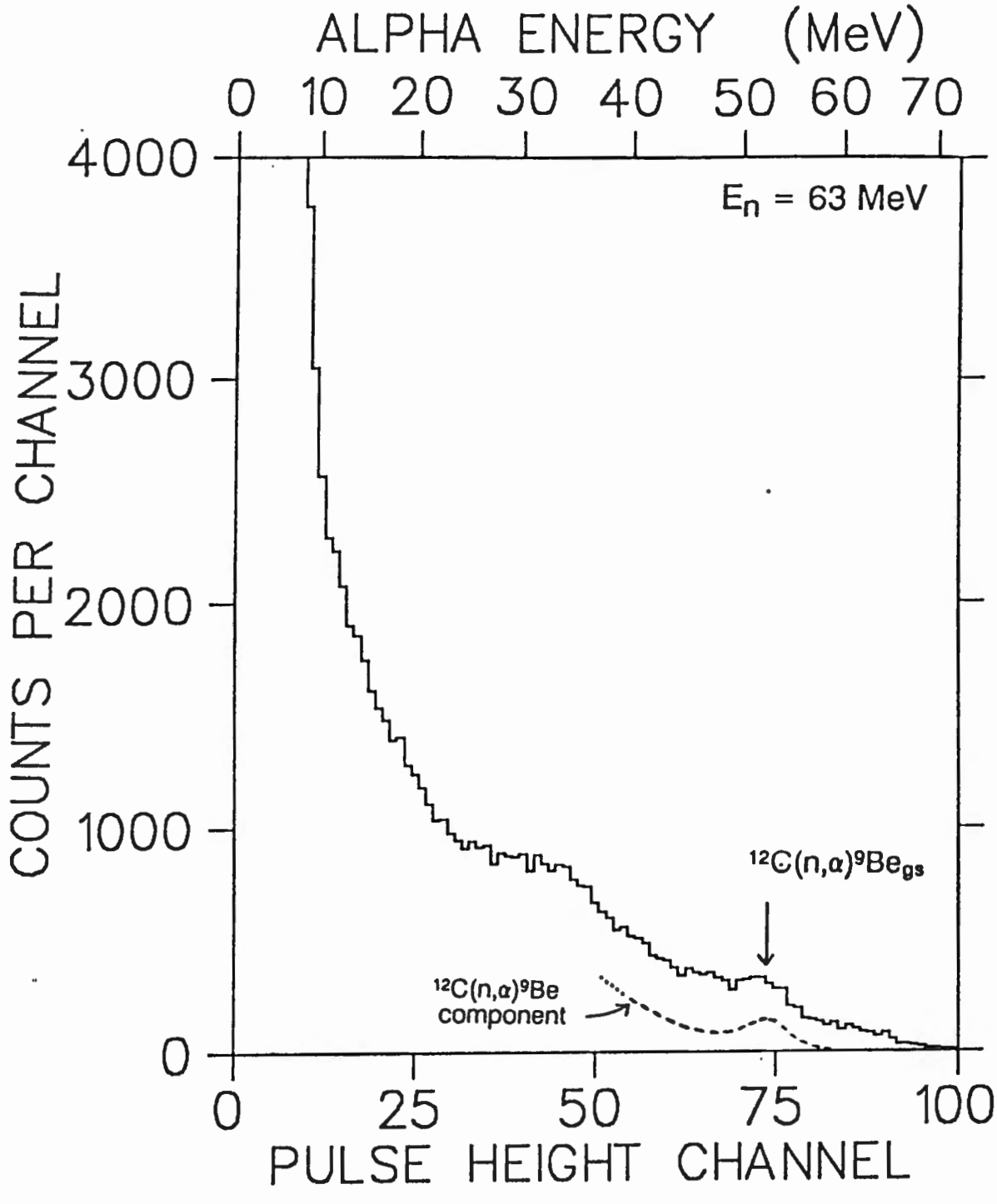

Figure 5.13 Pulse height spectrum, measured by 5 cm (diameter) by 5 cm NE213 liquid scintillator at E_n = 63 MeV, for events identified as alphas by pulse shape discrimination. Also shown is the upper pulse height portion of the $^{12}C(n,\alpha)^9Be$ spectrum (refer to section 3.2(b)).

CHAPTER 6

CROSS SECTIONS FOR n-^{12}C REACTIONS

The response functions (figure 3.3) of the detector, measured for incident neutrons in the range 15-63 MeV, have been separated, by the means of pulse shape discrimination, into their components associated with protons, deuterons and alphas. There are two sources of contribution to the proton component as discussed in chapter 3, namely, protons recoiling from ^{1}H(n,n)^{1}H events and those released in n-^{12}C interactions.

Total cross sections for neutron-induced proton, deuteron and alpha production from ^{12}C, were measured for 15-63 MeV neutrons, by comparing the yields for each type of charged particle with the yield for protons recoiling from elastic scatters. The total cross section for n-p elastic scattering, which is well known over the neutron energy domain of this work, provided a reference to reduce the relative values for the reaction cross sections to an absolute scale.

6.1 CROSS SECTION FOR $^{12}C(n,px)$

In order to measure the total cross section for neutron-induced proton production from ^{12}C i.e. $^{12}C(n,px)$; at each E_n, the $^1H(n,n)^1H$ component was unfolded from the n-^{12}C component in the proton pulse height spectrum.

(a) UNFOLDING OF THE PROTON PULSE HEIGHT SPECTRUM

The maximum kinematically-allowed energy, E_C, for protons released from n-^{12}C reactions, was calculated by means of the standard reaction kinematic equations (Appendix A) using the Q-value of the $^{12}C(n,p)^{12}B$ reaction of -12.59 MeV (Aj85). This reaction was chosen as it has the lowest Q-value of all the proton-releasing n-^{12}C reactions and hence is able to release the most energetic protons. Figure 4.4 showed E_C versus E_n from threshold up to 70 MeV for the reaction $^{12}C(n,p)^{12}B$.

This energy, E_C, corresponds to a maximum pulse height, L_C, on the proton pulse height spectrum. (Refer to figure 6.1 for clarification of all symbols used in this section.) Now all signals associated with protons released from n-^{12}C events in the scintillator lie at pulse heights less than L_C. Then all counts having $L > L_C$ can be attributed to protons recoiling from $^1H(n,n)^1H$ elastic scattering events. There is, however, a slight overlap of the $^{12}C(n,p)^{12}B$ signals to pulse heights greater than L_C due to the Gaussian spreading of the events in each pulse height channel (see figure 6.1). The maximum contribution of this overlap to the uncertainty in the measured cross sections is estimated to be of the order of 3%.

Those protons recoiling from n-p elastic scattering events producing pulses in the range $L > L_C$ ($E > E_C$), lie within a cone with internal angle ζ in the laboratory frame. This angle is related to the incident neutron energy E_n, and recoiling proton energy, E_p by:

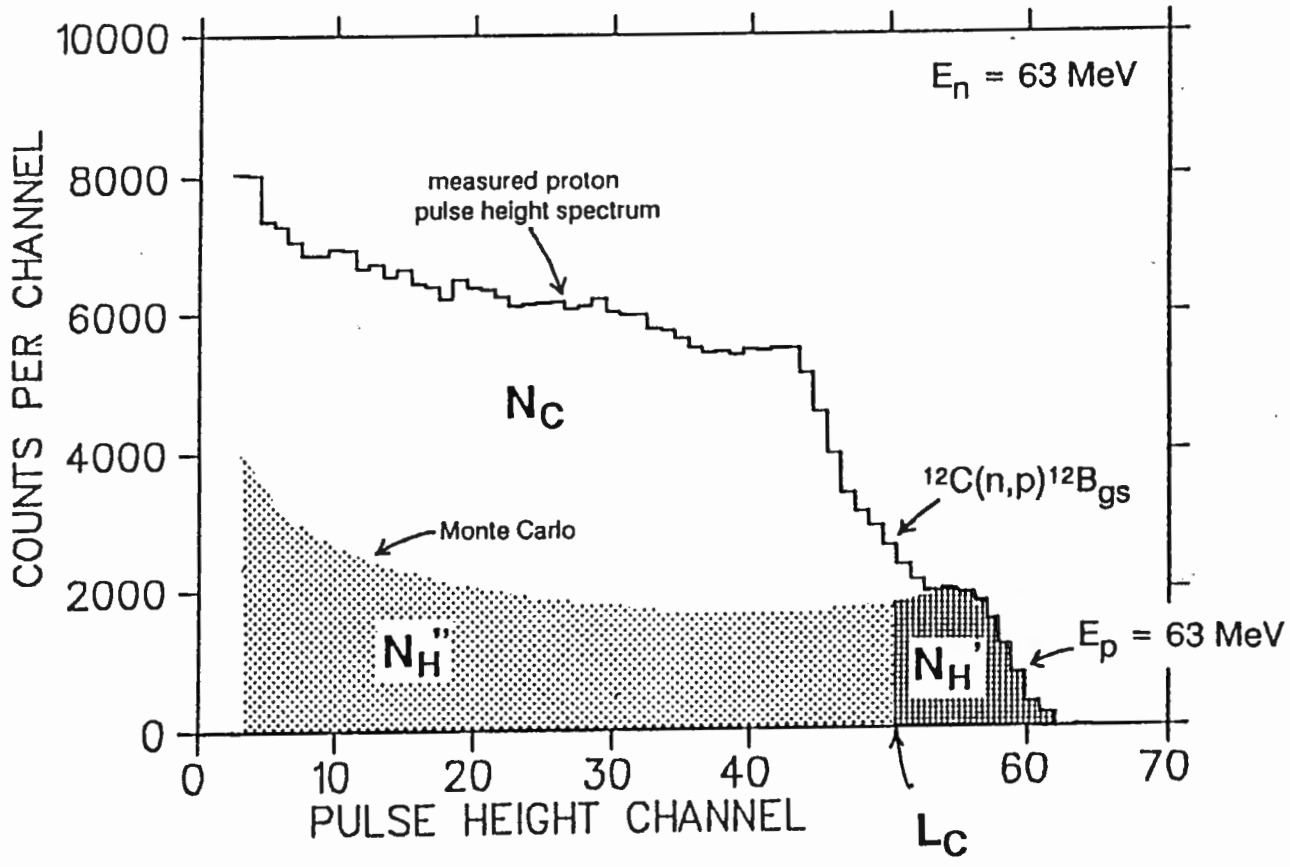

L_C : upper pulse height limit for protons released in $^{12}C(n,p)^{12}B$ reactions

N_H' : (hatched) n-p elastic scattering events having a pulse height greater than L_C

N_H'' : (dots) n-p elastic scattering events having a pulse height less than L_C

N_T : all (proton) events in the spectrum

N_H : all n-p elastic scattering events

$$N_H = N_H' + N_H''$$

N_C : all n-^{12}C reaction proton events

$$N_C = N_T - N_H$$

Figure 6.1 Proton pulse height spectrum, measured at E_n = 63 MeV, illustrating the symbols used in the analysis in the text.

$$E_p = E_n \cos^2\zeta \tag{6.1}$$

The associated scattered neutron angle, θ, in the centre-of-mass frame is obtained from:

$$\cos\theta = 1 - 2\cos^2\zeta \tag{6.2}$$

or from (6.1):

$$\cos\theta = 1 - 2E_p/E_n. \tag{6.3}$$

Therefore E_C is related to an associated neutron angle θ_C in the centre-of-mass frame by:

$$\cos\theta_C = 1 - E_C/E_n. \tag{6.4}$$

A low pulse height threshold corresponding to a proton threshold energy E_0 = 5 MeV was set on the LINK during running. This threshold, E_0 , defines an associated neutron angle θ_0 at each E_n where:

$$\cos\theta_0 = 1 - E_0/E_n \tag{6.5}$$

where E_0 = 5 MeV for all E_n.

Now the fraction, $f(E_n)$, of elastic scattered protons recorded above the threshold L_C $(\theta > \theta_C)$ is given by:

$$f(E_n) = \frac{\int_{\theta_c}^{2\pi} \sigma_{nn}(\theta)\, d\theta}{\int_{\theta_0}^{2\pi} \sigma_{nn}(\theta)\, d\theta} \tag{6.6}$$

where $\sigma_{nn}(\theta)$ is the differential cross section of the n-p elastic scattering process, given by Gammel's empirical formula (equation 5.1). The calculated values of $f(E_n)$ for the neutron energies considered in this work are listed in

table IV. Figure 6.2 shows the n-p differential elastic scattering cross section at the different incident neutron energies considered in this work, as predicted by equation 5.1.

The observed proton yield is strongly affected by the effect of proton escape, especially as E_n increases beyond 40 MeV, as discussed in section 3.3. All the proton pulse height spectra measured for incident neutrons in the energy range 15-63 MeV were corrected for protons escaping from the detector, as follows. The n-p elastic scattering component of the proton pulse height spectrum measured at E_n = 63 MeV has been simulated (see section 5.1). Figure 5.4(a) showed this simulated component fitted to the upper edge of the proton pulse height spectrum measured at E_n = 63 MeV. Figure 5.4(b) showed the same component but simulated neglecting edge effects. The ratio of spectrum (b) to spectrum (a) in figure 5.4 defines the factor, $x(L)$, which was used to correct all proton pulse height spectra measured at $E_n \leq 63$ MeV for the effect of proton escape. This correction was effected by multiplying each pulse height channel in each proton pulse height spectrum by the factor $x(L)$, and is estimated to be good to better than 7 %.

Figure 6.3 shows a plot of $x(L)$ versus pulse height, L, shown together with a proton energy scale. The escape correction factor, $x(L)$, as expected, tends to unity at the low pulse height limit. It is seen to increase significantly for proton energies exceeding about 40 MeV, as the range of the proton approaches the thickness of the detector (5 cm).

At the high pulse height limit, the curve reaches its maximum value of $x(L)$ = 6.8 at the pulse height corresponding to E_p = 63 MeV. The finite detector resolution will spread some 63 MeV proton events to higher pulse heights where $x(L)$ remains constant (indicated by the dahed line in figure 6.3) at its maximum value of 6.8. It can be seen from the figure that about six out of every seven protons of energy 63 MeV will escape from the scintillator without depositing all of their energy in the detector volume.

This is supported by an independent analytical calculation (Appendix B) at E_n = 63 MeV. The ratio of all forward recoiling protons of energy 63 MeV to

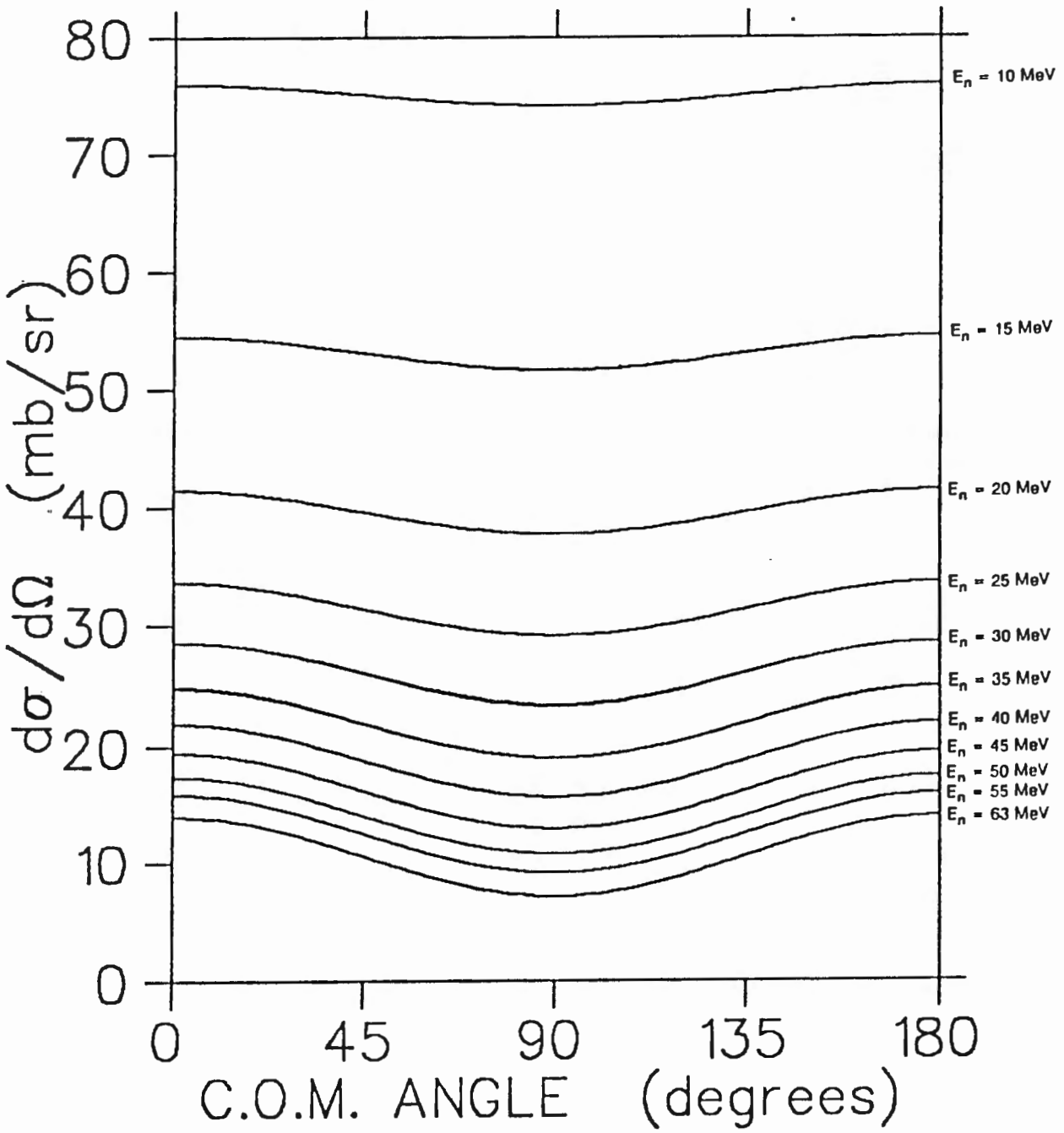

Figure 6.2 Differential cross sections for the process $^1H(n,n)^1H$, calculated using the the empirical relation of Gammel (Ga63) *for the range of incident neutron energies considered in this work.*

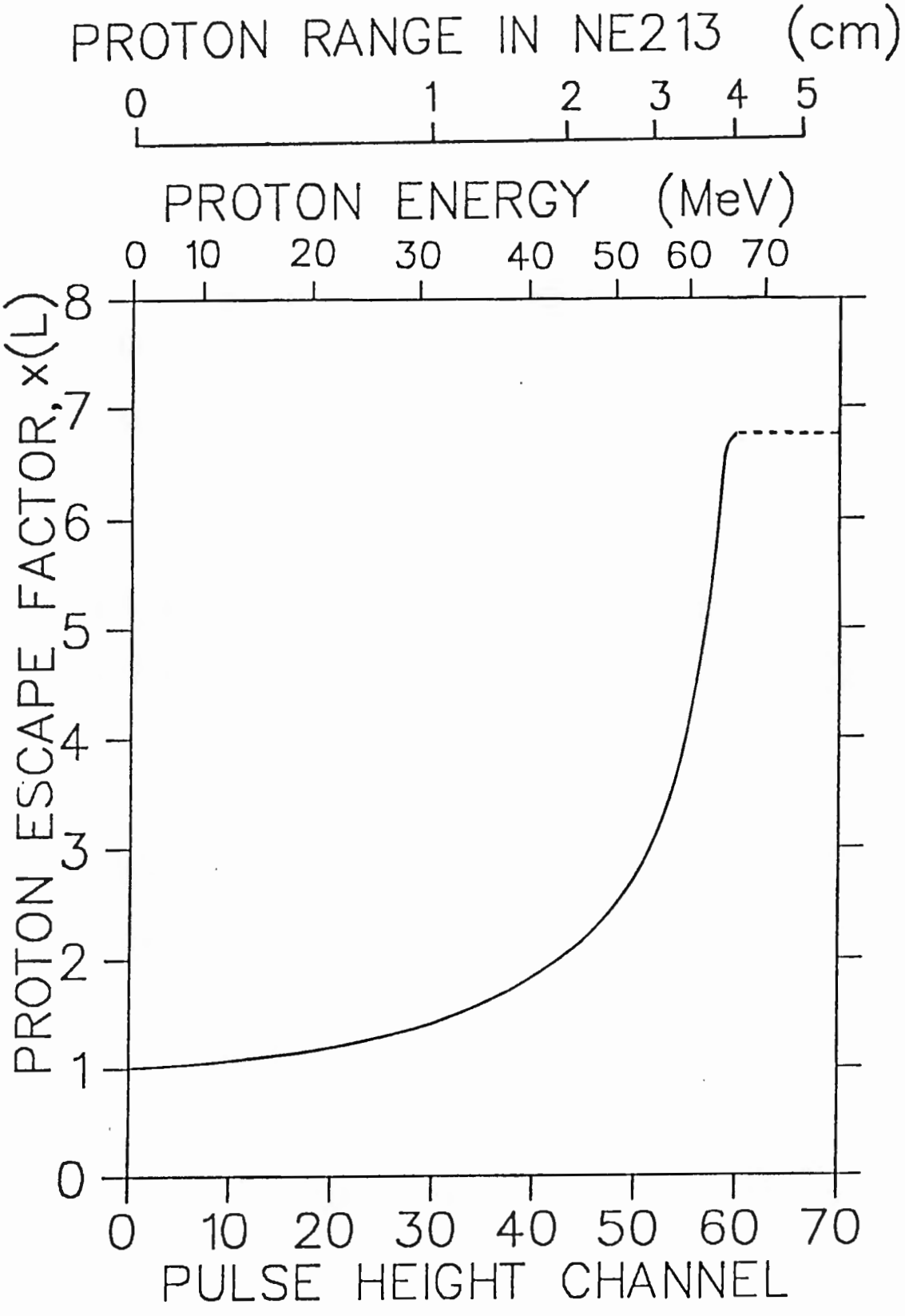

Figure 6.3 Proton escape factor, x(L) , as a function of pulse height channel (arbitrary) and proton energy, used to correct all measured proton pulse height spectra for the effect of proton escape. The correction is seen to become particularly significent at E_p > 40 MeV, as the range of protons in NE213 (also shown) approaches the dimensions of the detector.

those which do not escape from the scintillator was calculated to be 7.3. This value agrees well with the maximum escape factor of $x(L)$ = 6.8 obtained from the Monte Carlo as described above.

After correcting the pulse height spectra measured at each E_n for proton escape, two integrals were determined from each spectrum. These were the total number of counts in the spectrum, N_p, and the number of counts, N_H', from L_C to the upper limit of the pulse height spectrum.

Then the total number of elastically scattered protons, N_H, in the pulse height spectrum measured at a particular E_n, is given by

$$N_H = N_H'/f \tag{6.7}$$

where f is the fraction of measured elastically scattered proton events recorded at pulse heights $L > L_C$, as given by equation 6.6. Then the number of n-p elastic scattering events, N_H'', recorded at pulse heights $L < L_C$ is given by

$$N_H'' = N_H'(1-f)/f, \tag{6.8}$$

and

$$N_H = N_H' + N_H''. \tag{6.9}$$

Finally, the total number of counts in the pulse height spectra arising from the detection of protons released in n-^{12}C reactions, N_C (corrected for proton escape), may be determined from:

$$N_C = N_p - N_H \tag{6.10}$$

(b) THE $^{12}C(n,px)$ CROSS SECTION

In the thin scintillator limit, one may write

$$N_C = N_0 \, n_C \, \sigma_{np} \tag{6.11}$$

and

$$N_H = N_0 \, n_H \, \sigma_{nn} \tag{6.12}$$

where:

- N_0 : total number of incident neutrons
- n_C : number of ^{12}C nuclei per cross sectional area presented by the scintillator to the neuton beam
- n_H : number of ^{1}H nuclei per cross sectional area
- σ_{nn} : $^{1}H(n,n)^{1}H$ total cross section (known (St64), see figure 1.5)
- σ_{np} : $^{12}C(n,px)$ total cross section

Taking the ratio:

$$\sigma_{np} = (N_C / N_H)\,(n_C / n_H)\,\sigma_{nn} \tag{6.13}$$

where $n_C / n_H = 0.825$ for NE213

The total cross section for the reaction $^{12}C(n,px)$ was measured at 10 incident neutron energies. The results are listed in table IV and plotted in figure 6.4. Also shown in the figure are the measurements of Kellogg (Ke53) and Kreger *et al* (Kr59), which compare well with the measurements of this work.

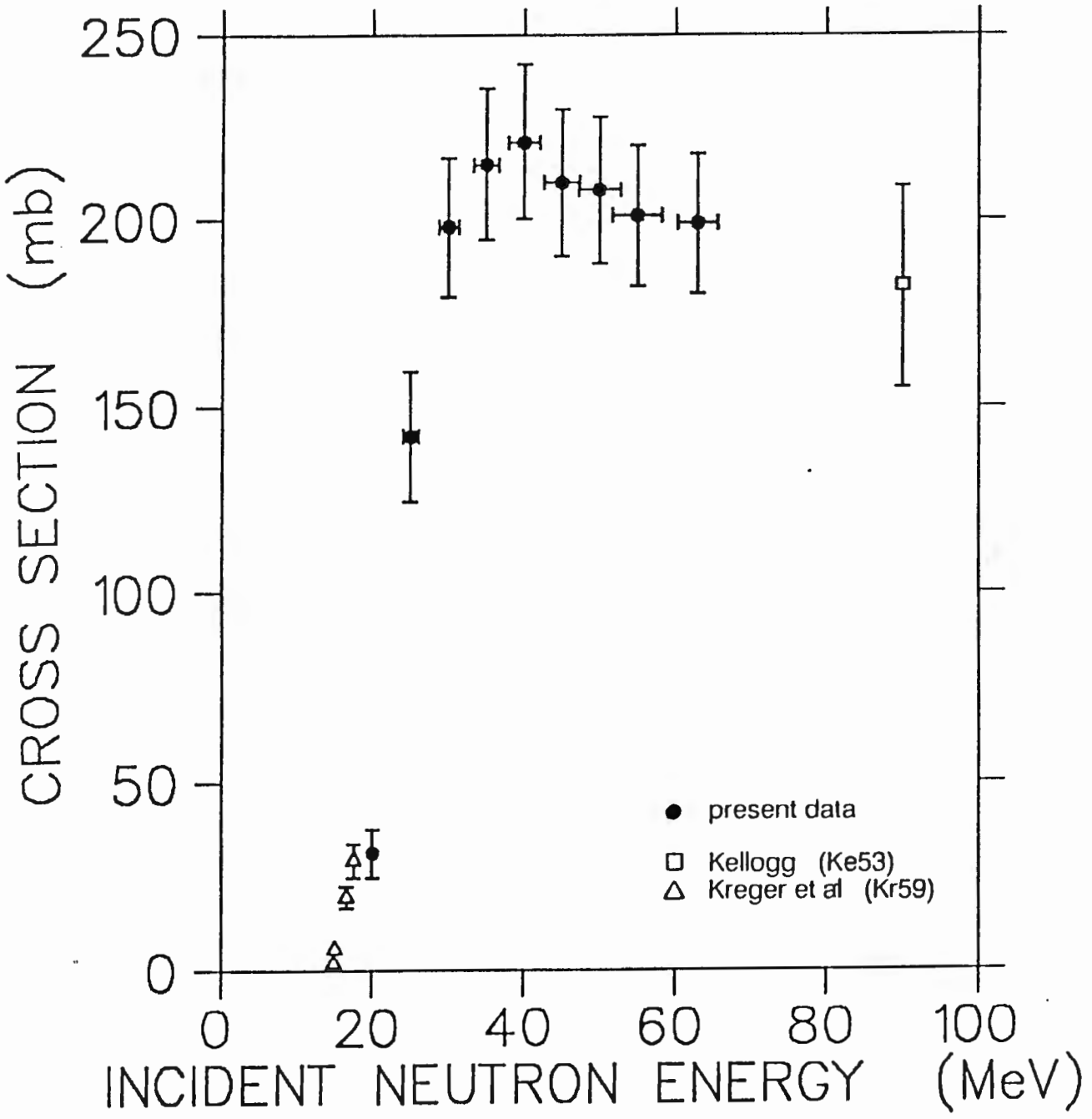

Figure 6.4 Total cross section for the $^{12}C(n,px)$ reaction obtained in this work, compared to the measurements of Kellogg (Ke53) *and Kreger et al* (Kr59).

E_n (MeV)	ΔE_n (MeV)	σ_{nn} (mb)	$f(E_n)$	σ_{np} (mb)	$\Delta\sigma_{np}$ (mb)
20.0	0.7	500	0.59	31.2	7.0
25.0	1.0	380	0.50	141.9	17.6
30.0	1.3	325	0.43	197.6	19.0
35.0	1.7	263	0.37	215.1	20.4
40.0	2.0	222	0.33	221.2	20.9
45.0	2.4	191	0.29	210.0	20.0
50.0	2.8	160	0.27	207.9	19.8
55.0	3.3	143	0.24	201.1	19.2
63.3	2.6	118	0.22	199.1	19.1

Table IV *Total cross sections for neutron induced proton production from ^{12}C, σ_{np}, as measured in this work as a function of incident neutron energy. Also listed are σ_{nn}, the assumed $^1H(n,n)^1H$ total cross section* (St64), *and the fraction $f(E_n)$ (see text).*

(c) ESTIMATES OF UNCERTAINIES

(i) neutron energy:

The uncertainty in the incident neutron energy was calculated using equation 2.3 for neutron energies less than the 63 MeV peak. The width of the 63 MeV peak (2.2 ns) yields the uncertainty in energy for neutrons falling within in the peak as discussed in section 2.3.

(ii) cross section:

Errors due to counting statistics, which are estimated to be of the order of 1%, are negligible as the total number of counts in each pulse height

spectrum is typically greater than 10^4. The Gaussian spread of the counts measured in each pulse height channel is a direct result of the statistical nature of the photo- and secondary emission processes in the photomultiplier. This introduces about a 5% uncertainty with the measurement of any edge or peak in a pulse height spectrum.

The principal sources of systematic uncertainty are as a result of the separation of the charged particle loci in the *L-S* two parameter spectra (section 3.2), the setting of all neutron time of flight (E_n) windows, and the measurement of all peaks and edges in the pulse height spectra. All these stages in the analysis are subject to systematic variations which are difficult to assess. It was found that the best way to do this is to repeat the analysis and to observe the fluctuation in the result. This has been done at a selection of neutron energies and the fluctuation was less than 3%.

The correction for proton escape by Monte Carlo is thought to be accurate to better than 7% over the full range of neutron energies. The error in the final cross section measurements arising from neutron multiple neutron scattering, on the other hand, is difficult to assess. It can be seen figure 3.13(c) that the contribution to the proton ridge associated with multiple scattering events is of the order of 3% at E_n = 63 MeV. The multiple scattering contribution was measured to be of the order of 8% at E_n = 20 MeV. Therefore, it was estimated that it would contribute, on average, an uncertainty of less than 6% to the final result.

The cross sections for neutron-induced charged particle production were determined from the ratio of reaction products and elastically scattered protons. Therefore, it was not necessary to know either the number of incident neutrons or the total number of target nuclei. Therefore there is no contribution from these quantities to the final uncertianty of the cross section measurements.

The total uncertainties, $\Delta\sigma$, in the values for the total cross sections for neutron induced proton, deuteron and alpha production shown in all figures

and tables, were calculated by the quadratic summation of all the components discussed above.

6.2 CROSS SECTION FOR ^{12}C(n,dx)

The total cross section for neutron-induced deuteron production from ^{12}C, i.e. ^{12}C(n,dx), was measured as a function of E_n. This is the cross section for any process which process a pulse, which when plotted on an L-S plane, lies on the deuteron locus as identified by pulse shape discrimination. By measuring the total number of counts, N_d, in each deuteron pulse height spectrum (figure 3.16), the ^{12}C(n,dx) total cross section was calculated as a function of E_n from:

$$\sigma_{nd} = (N_d / N_H)(n_C / n_H)\,\sigma_{nn} \qquad (6.14)$$

where: σ_{nd} : ^{12}C(n,dx) total cross section

σ_{nn}, N_H, and n_H / n_C : as in the case for protons

The total cross section for the reaction ^{12}C(n,dx) was measured at 9 incident neutron energies. The results are listed in table V and plotted in figure 6.5. Also shown in the figure is a measurement made by Kellogg (Ke53) at E_n = 90 MeV which agrees with the trend of the measurements of this work.

6.3 CROSS SECTION FOR ^{12}C(n,ax)

Similarly, as for the case of the deuterons, the number of counts, N_α, in each alpha pulse height spectrum (figure 3.11) were measured as a function of E_n. The total cross section for neutron-induced alpha production from ^{12}C, i.e. ^{12}C(n,αx), was then calculated as a function of E_n from

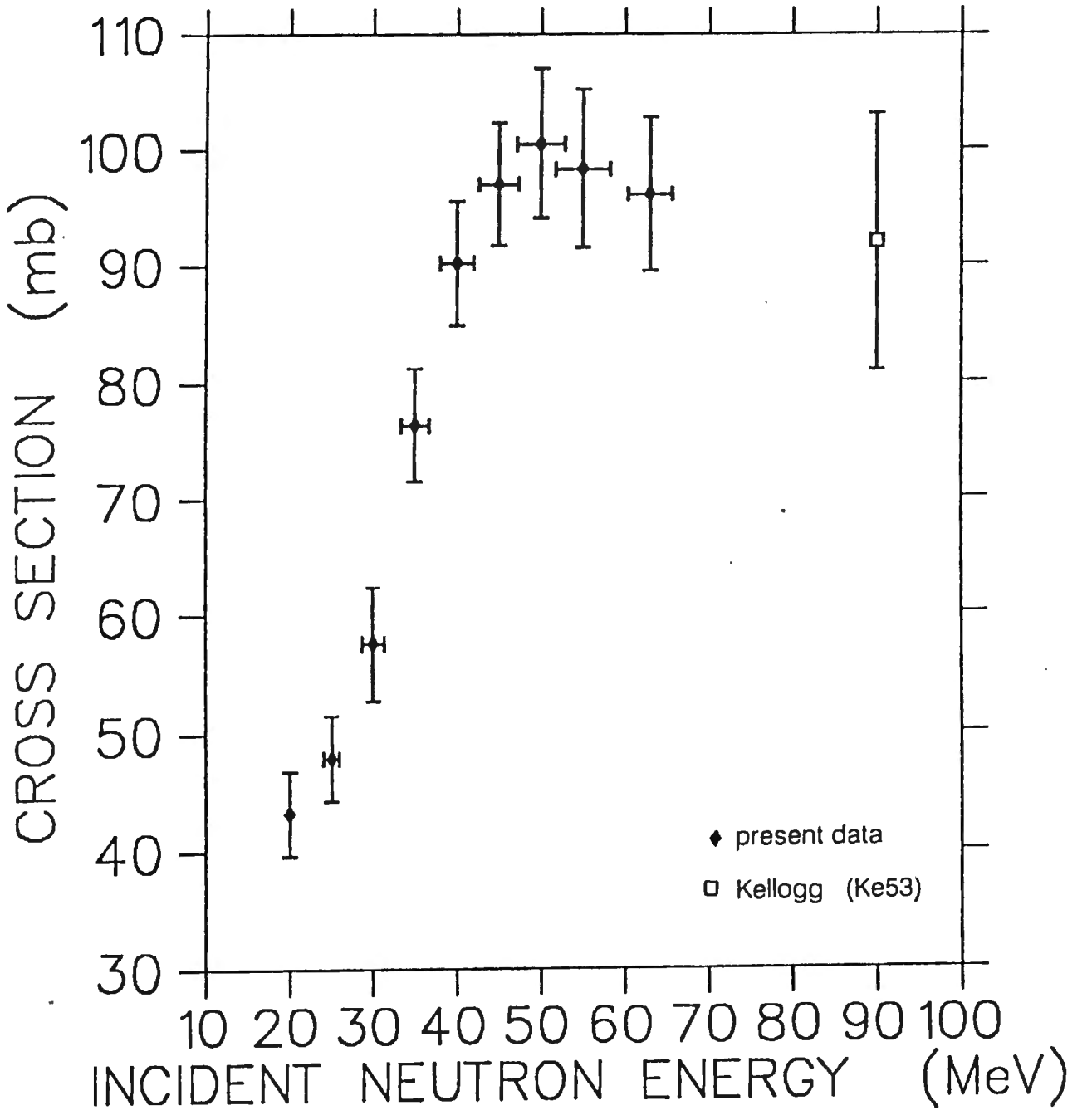

Figure 6.5 Total cross section for the $^{12}C(n,dx)$ reaction obtained in this work, compared to a measurement by Kellogg (Ke53).

$$\sigma_{n\alpha} = (N_\alpha / N_H)(n_C / n_H)\,\sigma_{nn} \qquad (6.15)$$

where: $\sigma_{n\alpha}$: $^{12}C(n,\alpha x)$ total cross section

σ_{nn}, N_H, and n_H / n_C : as before

The total cross section for the reaction $^{12}C(n,\alpha x)$ was measured at 9 incident neutron energies. The results are listed in table VI and plotted in figure 6.6. Also shown in the figure are the measurements of Kellogg (Ke53) and Frye *et al* (Fr55), which again agree well with the measurements of this work.

In conclusion, total cross sections for neutron-induced proton, deuteron and alpha production from ^{12}C have been measured at different neutron energies in the range 20-63 MeV. The present data is seen to correspond well with the few measurements available in the literature for this neutron energy range.

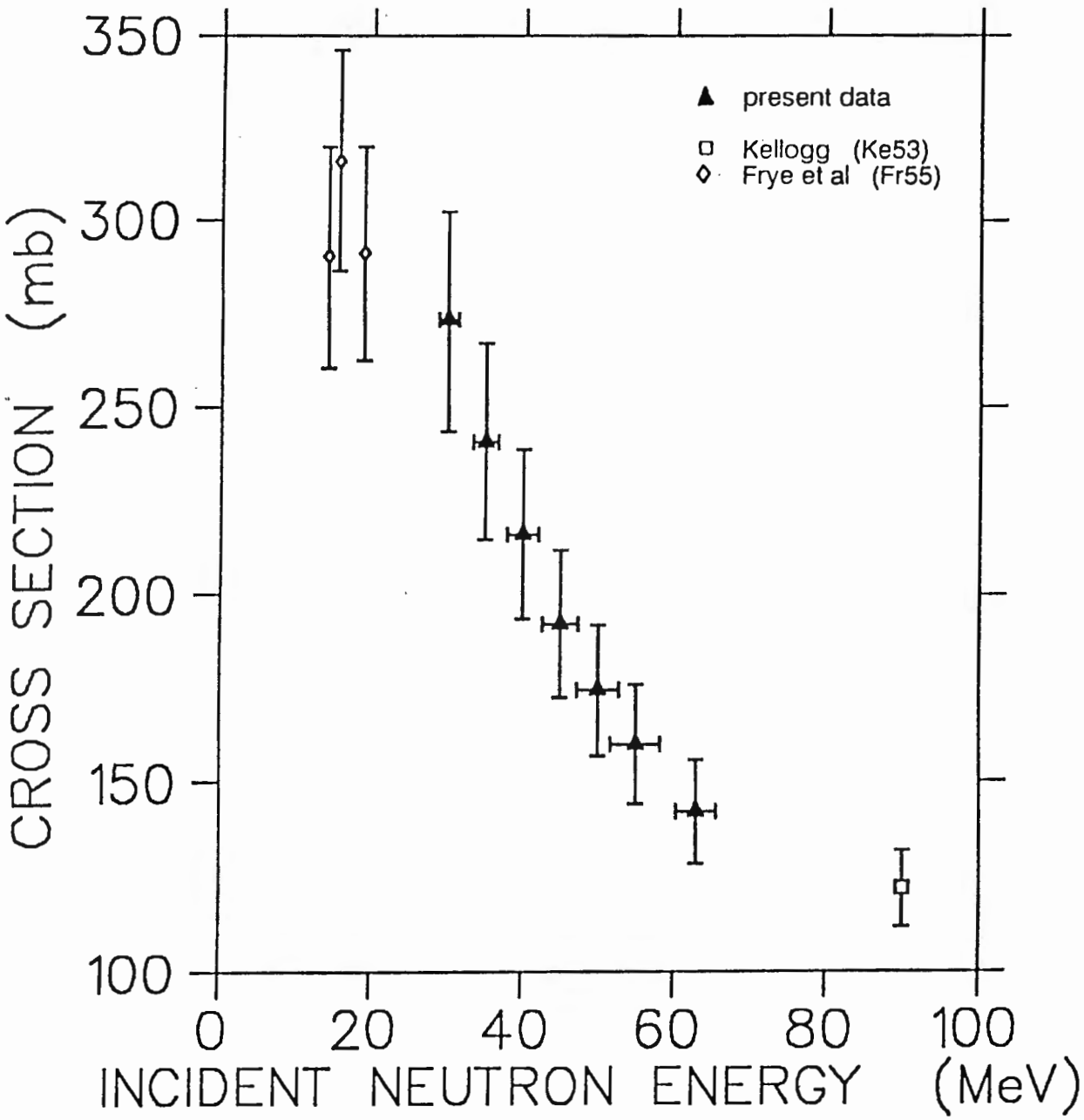

Figure 6.6 Total cross section for the $^{12}C(n,\alpha x)$ reaction obtained in this work, compared to the measurements of Kellogg (Ke53) *and Frye et al* (Fr55).

E_n (MeV)	ΔE_n (MeV)	σ_{nd} (mb)	$\Delta\sigma_{nd}$ (mb)
20.0	0.7	43.2	3.6
25.0	1.0	47.9	3.6
30.0	1.3	57.6	4.8
35.0	1.7	76.4	4.8
40.0	2.0	90.2	5.3
45.0	2.4	97.0	5.3
50.0	2.8	100.5	6.4
55.0	3.3	98.3	6.8
63.3	2.6	96.1	6.6

Table V Total cross section for neutron induced deuteron production from ^{12}C, σ_{nd}, as measured in this work as a function of incident neutron energy.

E_n (MeV)	ΔE_n (MeV)	$\sigma_{n\alpha}$ (mb)	$\Delta\sigma_{n\alpha}$ (mb)
30.0	1.3	272.8	29.4
35.0	1.7	240.6	25.9
40.0	2.0	216.0	22.6
45.0	2.4	192.2	19.8
50.0	2.8	174.4	17.6
55.0	3.3	160.0	15.8
63.3	2.6	142.1	13.6

Table VI Total cross section for neutron induced alpha production from ^{12}C, $\sigma_{n\alpha}$, as measured in this work as a function of incident neutron energy.

CHAPTER 7

NEUTRON DETECTION EFFICIENCY

The efficiency of a detector for detecting neutrons of a particular energy is the probabilty of an incident neutron of that energy producing an acceptable pulse in the detector. The criteria for acceptance will usually include the production of a signal exceeding a certain minimum energy, the 'detector threshold,' and may also require neutron identification, e.g. by pulse shape discrimination. In the case of organic scintillators, such as NE213, the neutron must transfer enough energy to a charged particle (most often a proton) to ensure that a scintillation pulse exceeding the electronic detection threshold is generated.

Therefore the efficiency of a detector for detecting neutrons will depend upon:

(i) the energy of the incident neutron,
(ii) the cross section of the process(es) e.g. n-p elastic scattering, which is (are) used in neutron detection,
(iii) the type, size and shape of the detector,

(iv) the electronic threshold of detection, and

(v) the efficiency with which any signature, e.g. pulse shape discrimination, if applied, recognises the neutron detection pulses used.

The efficiency of the NE213 scintillator for n-p elastic scattering was calculated, in the thin scintillator limit, for incident neutrons in the range 20 to 63 MeV, assuming the measurements of the $^1H(n,n)^1H$ total cross section presented in the literature. By measuring the number of n-p elastic scatterings and the number of n-^{12}C interaction events detected at each E_n, and considering the effect of proton escape, the efficiency of the scintillator for n-^{12}C interactions was determined relative to the calculated n-p elastic scattering effieciency. The sum of the effiencies for n-p elastic scattering and n-^{12}C interactions then gave the total neutron detection efficiency of the detector.

7.1 CALCULATION OF THE EFFICIENCY FOR n-p ELASTIC SCATTERING

For an NE213 scintillator, the efficiency, ϵ_H , for detection via *n-p elastic scattering only* (ignoring multiple scattering events), is given at zero detection threshold by:

$$\epsilon_H = \frac{n_H \sigma_{nn}}{n_H \sigma_{nn} + n_C \sigma_{nC}} \left[1 - exp\left(- n_H \sigma_{nn} - n_C \sigma_{nC} \right) \right] \qquad (7.1)$$

where:

n_H : number of ^1H nuclei per unit cross sectional area presented by the scintillator to the beam

n_C : number of ^{12}C nuclei per unit cross sectional area presented by the scintillator to the beam

σ_{nn} : $^1H(n,n)^1H$ total cross section ((St64), figure 1.5)

σ_{nC} : total cross section for *all* neutron-induced interactions with ^{12}C nuclei in the detector.

As the measurements in the present work were made using a 5 cm (diameter) by 5 cm cylindrical NE213 detector, orientated with its curved surface facing the incident neutron beam, the thin scintillator approximation was assumed to be valid. In the case where $(n_H\,\sigma_{nn} + n_C\,\sigma_{nC}) \ll 1$, equation 7.1 reduces to

$$\epsilon_H = \frac{n_H\,\sigma_{nn}}{n_H\,\sigma_{nn} + n_C\,\sigma_{nC}}\,[\,1 - (\,1 - n_H\,\sigma_{nn} - n_C\,\sigma_{nC}\,)\,] \qquad (7.2)$$

or

$$\epsilon_H = n_H\,\sigma_{nn} \qquad (7.3)$$

The justification for this approximation is as follows.

The molecular mass, M, for NE213 scintillator (consisting mainly of mainly xylene (C_8H_{10})) is simply 108 g/mole. The density, ρ, of NE213 is known to be 0.874 g/cm^3 (table II). Assuming ρ to be constant throughout the NE213 scintillator volume, the average number of ^1H nuclei per unit cross sectional area, n_H, is then given by:

$$n_H = (10/M)\,N_A\,\rho\,\pi\,(R/2) \qquad (7.4)$$

where the neutrons are incident on the curved surface of a cylindrical detector of radius R, and average thickness $\pi\,(R/2)$; and N_A is Avogadro's number. For the detector used in this work (5 cm diameter), n_H was calculated to be 0.195 nuclei per barn. Consequently, the average number of ^{12}C nuclei per barn, n_C, is equal to:

$$n_C = 0.8\,n_H = 0.156 \qquad (7.5)$$

Shown in figure 7.1 is a compilation (De76) of total cross sections for n-p elastic scattering and n-^{12}C interactions (for both including and excluding ^{12}C(n,n)^{12}C elastic scattering). Using the values for *all* n-^{12}C interactions, $(n_H\ \sigma_{nn} + n_C\ \sigma_{nC})$ was calculated to be 0.35 at E_n = 20 MeV and 0.17 at E_n = 63 MeV. In addition, it may be assumed the contribution from ^{12}C(n,n)^{12}C elastic scattering in the scintillator will not affect the efficiency significently as the number of neutrons scattered so as to increase and decrease, respectively, their path lengths in the scintillator will balance each other approximately. Furthermore, the response of NE213 to ^{12}C nuclei is weak and most recoiling ^{12}C nuclei will not be detected above the low pulse height threshold. The value of $(n_H\ \sigma_{nn} + n_C\ \sigma_{nC})$ was then calculated, using the values in the literature (De76) of σ_{nC} for *inelastic* n-^{12}C interactions *only*, to be 0.21 at E_n = 20 MeV and 0.08 at E_n = 63 MeV. Therefore, the thin scintillator approximation is valid to the order of 10% at E_n = 20 MeV and 4% at E_n = 63 MeV.

Section 5.1 showed that for neutron energies up to about 90 MeV, the angular distribution for n-p elastic scattering may be approximated by (Ga63):

$$\sigma_{nn}(\theta,E_n) = \frac{\sigma_{nn}\ (1 + b\cos^2\theta)}{4\pi\ (1 + 1/3\,b)} \qquad (7.6)$$

where $b = 2\,(E_n/90)^2$ and E_n in MeV.

It then follows (Lo76) that the probability, f, for a proton to have energy between $E_n - \delta$ and E_n is given by:

$$f = \frac{(\cos\theta + 1) + (b/3)(\cos^3\theta + 1)}{2(1 + b/3)}\ (\delta/E_n) \qquad (7.7)$$

where $\cos\theta = 2\,(\delta/E_n) - 1$

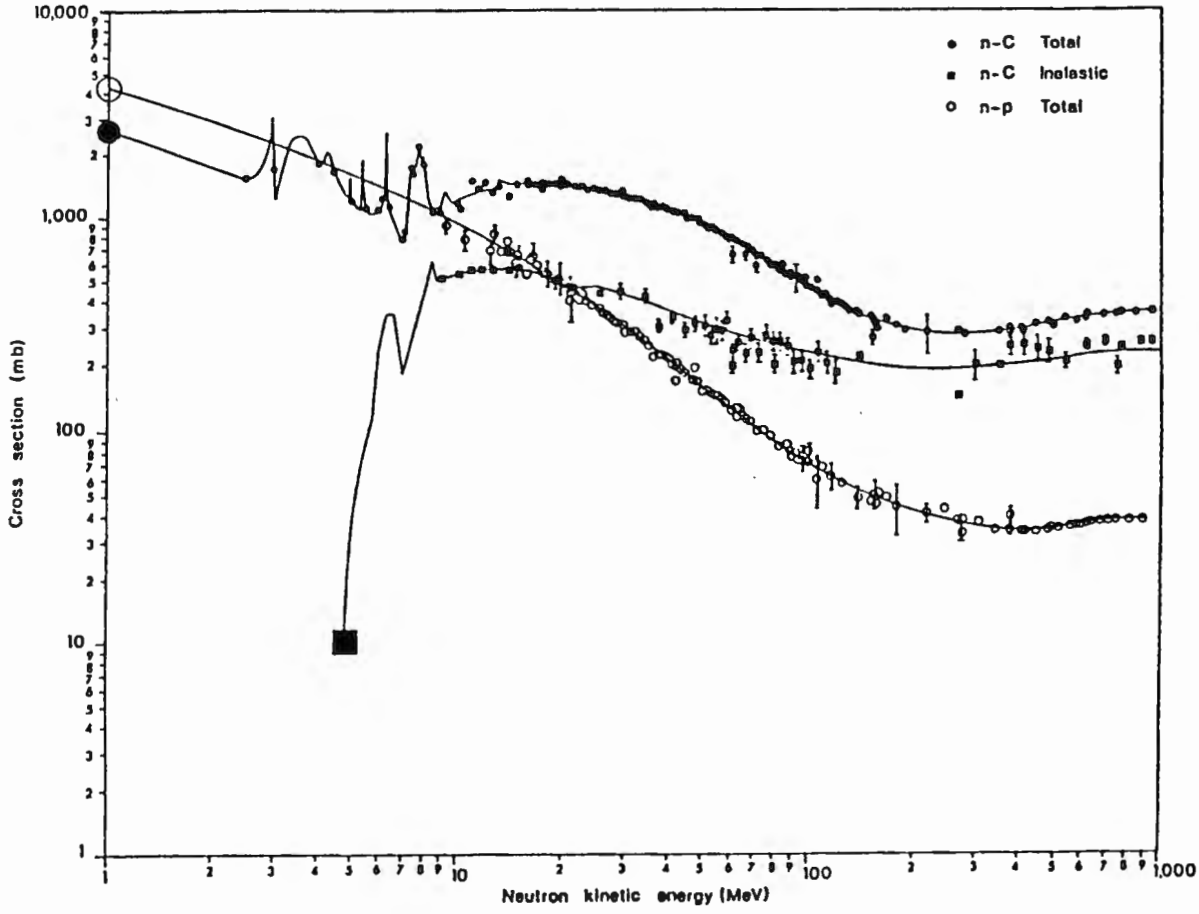

Figure 7.1 A compilation (De76) *of n-^{12}C (total), n-^{12}C (inelastic) and n-p elastic scattering total cross sections data. The full lines show the cross sections used in a Monte Carlo (see reference).*

A low pulse height threshold of 3 MeVee - corresponding to a proton threshold energy of 5 MeV - was set on the LINK during running. Then from equation 7.7, the fraction of n-p elastic scatters detected above the low pulse height threshold is given by:

$$f = \frac{(\cos\theta + 1) + (b/3)(\cos^3\theta + 1)}{2(1 + b/3)} (1 - 5/E_n) \qquad (7.8)$$

where $\cos\theta = 2(5/E_n) - 1$

Then the efficiency for n-p elastic scattering, ϵ_H, calculated for a low pulse height threshold of 3 MeVee, is given by:

$$\epsilon_H = f\, n_H\, \sigma_{nn} \qquad (7.9)$$

where f is given by equation 7.8.

This efficiency, ϵ_H, was calculated at different incident neutron energy in the range 20-63 MeV and the results are plotted in figure 7.2. As expected, ϵ_H is seen to reduce with increasing incident neutron energy as the total cross section for $^1H(n,n)^1H$ decreases.

7.2 THE TOTAL NEUTRON DETECTION EFFICIENCY

Section 6.1 described the unfolding of the proton pulse height spectrum, measured at each E_n, into its two components, namely, events associated with n-p elastic scattering , N_H and those associated with protons released from n-^{12}C reactions, N_C. A Monte Carlo (He91) was used (see section 6.1) to correct the proton pulse height spectrum, measured at each E_n, for the effect of proton escape. The factors $\varphi_C(E_n)$ and $\varphi_H(E_n)$ necessary to correct N_C and N_H respectively for the effect of proton escape, were predicted by the Monte

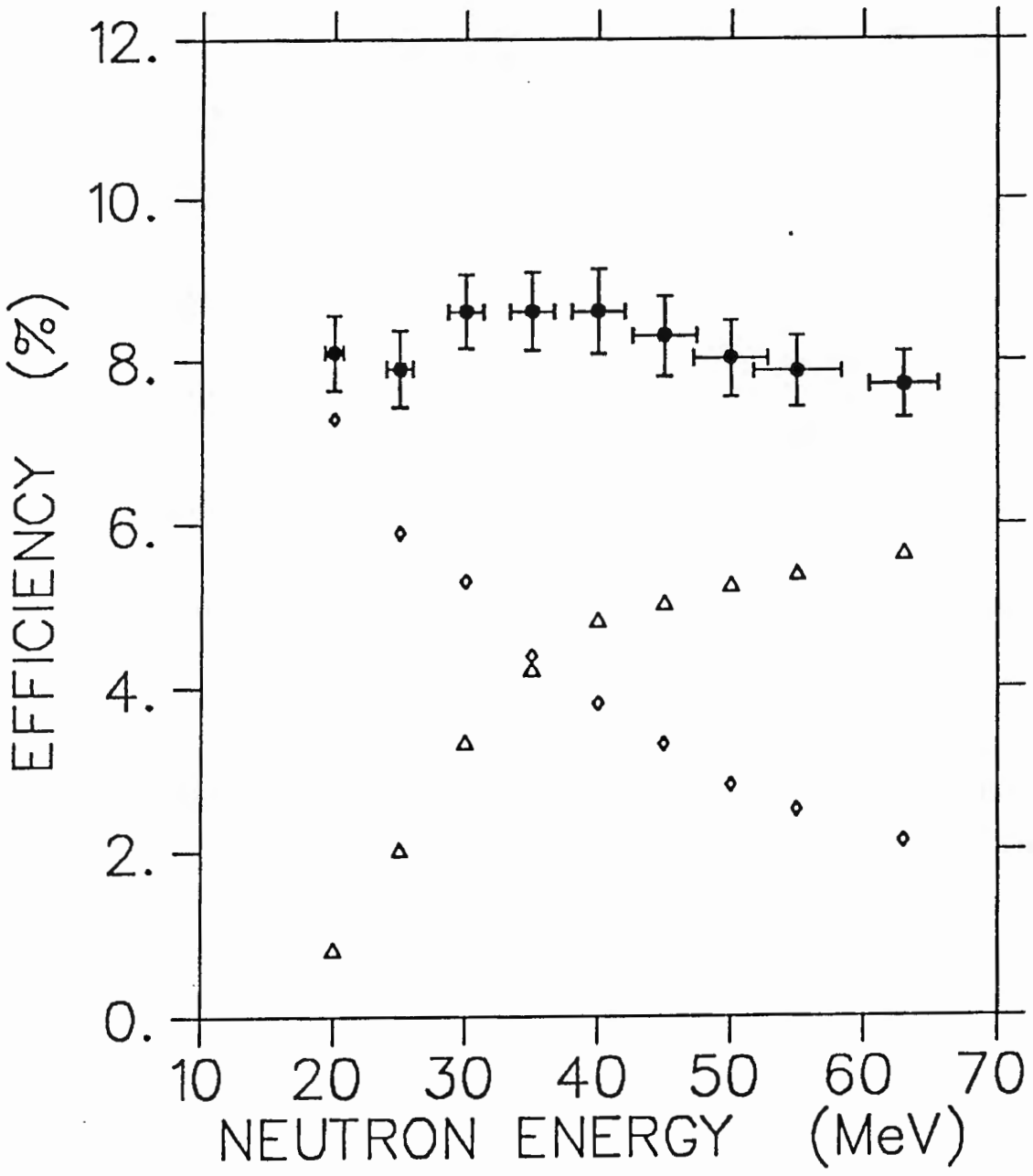

Figure 7.2 Neutron detection efficiency (•) of a 5 cm by 5 cm (diameter) cylinder of NE213, measured with a low detection threshold of 3 MeVee, relative to the calculated efficiency (◊) for n-p elastic scattering events. (see text). Also shown is the contribution to the overall efficiency (△) associated with n-^{12}C interactions in the scintillator. The scintillator was placed with its curved surface facing the incident neutron beam.

Carlo by determining the ratio of all proton events to those events associated with no proton escape, at each incident neutron energy. These factors are shown in figure 7.3 as a function of incident neutron energy.

Now, if N_T is the *total* number of events detected in the scintillator, at a particular neutron energy, excluding events whereby protons leave the scintillator (which will be placed on the proton escape locus (see figure 3.1)), the number of events, N_R ,detected *excluding* any proton-releasing n-^{12}C event (which will be placed on the proton locus) is given by

$$N_R = N_T - (N_C + N_H) \tag{7.10}$$

Then at each E_n , with the low detection bias set on the LINK at 3 MeVee, the efficiency of the scintillator for all n-^{12}C interactions, ϵ_C , may be determined at each incident neutron energy E_n , using:

$$\epsilon_C = N_T/N_0 = \frac{(\varphi_C N_C + N_R)}{\varphi_H N_H} f\, n_H\, \sigma_{nn} \tag{7.11}$$

where:

N_0 : number of incident neutrons of energy E_n

N_T : total number of events detected above the low pulse height threshold, corrected for the effect of proton escape

n_H : number of ^{1}H nuclei per unit cross sectional area presented by the scintillator to the beam

N_H : number of n-p elastic scattering events detected above the low pulse height threshold

N_C : number of n-^{12}C interaction events detected above the low pulse height threshold, associated with neutron-induced *proton* production from ^{12}C.

N_R : number of n-^{12}C interaction events detected above the low pulse height threshold, *excluding* all those attributed to neutron-induced proton production

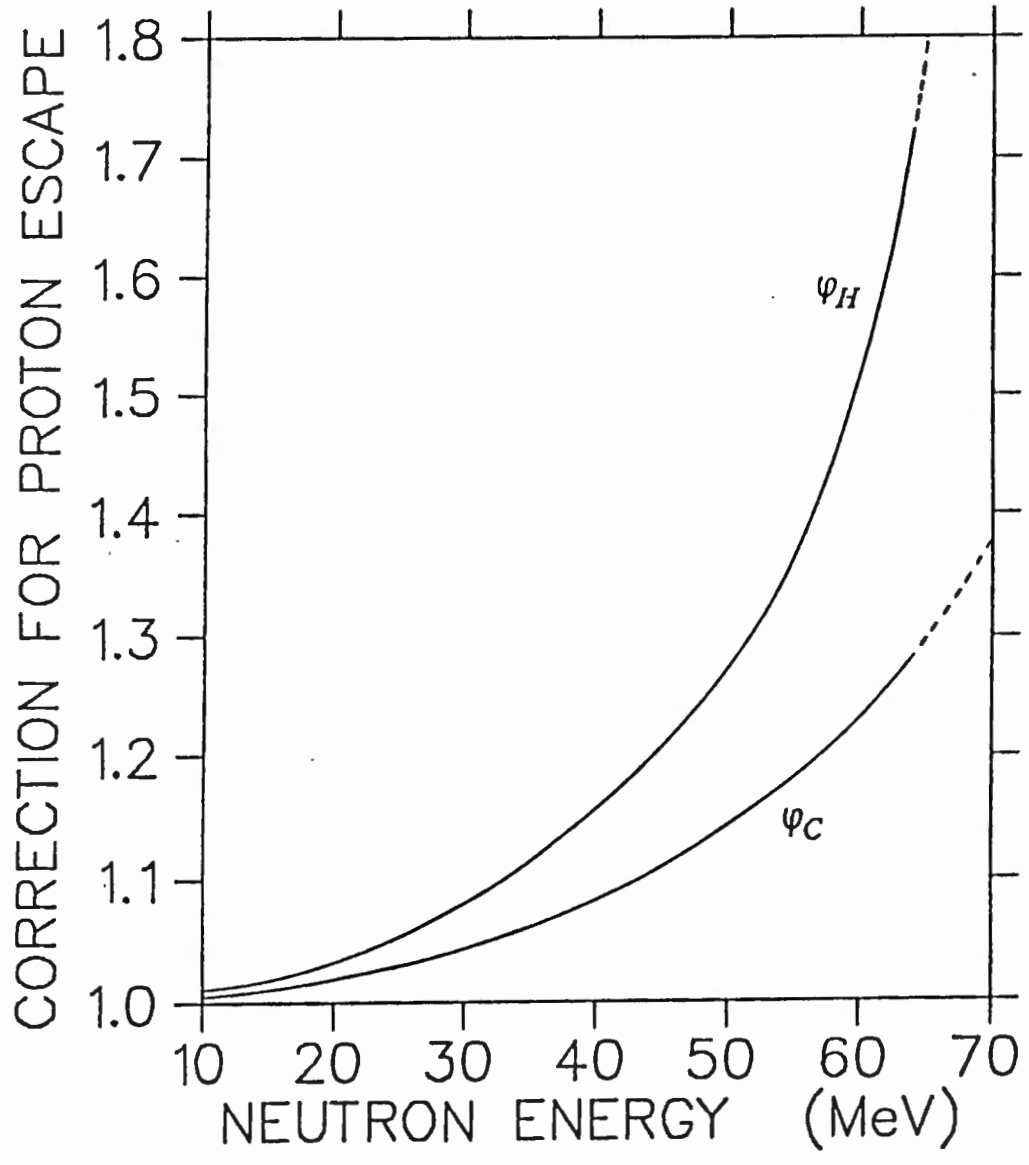

Figure 7.3 Factors used to correct the measured number of n-p elastic scatterings (φ_C) and proton producing n-^{12}C interactions (φ_H) for the effect of proton escape (see text).

φ_H : factor used to correct N_H for the effect of proton escape (figure 7.3)

φ_C : factor used to correct N_C for the effect of proton escape (figure 7.3)

σ_{nn} : ^{1}H(n,n)^{1}H total cross section ((St64), figure 1.5)

f : fraction of n-p elastic scatters detected above the low pulse height threshold of 3 MeVee

Finally, the efficiency of the scintillator, ϵ_T, for detecting all charged particles, protons or heavier, and recognised as such by pulse shape discrimination, above the low pulse height threshold of 3 MeVee, may be determined relative to the calculated n-p elastic scattering efficiency (equation 7.9) from:

$$\epsilon_T = \epsilon_H + \epsilon_C \tag{7.12}$$

Figure 7.2 shows this total neutron detection efficiency, ϵ_T, of a 5 cm (diameter) by 5 cm cylinder of NE213, to incident neutrons in the range 20 to 63 MeV, for detecting all events above the low threshold of 3 MeVee. Also shown in figure 7.2 is the calculated efficiency for n-p elastic scattering, ϵ_H, and the efficiency for neutron-induced ^{12}C interactions in the scintillator, determined relative to ϵ_H. The error bars indicate the statistical uncertainty in the measurements. There is a further systematic error arising from the thin scintillator approximation used, as discussed in section 7.1. This will introduce a further uncertainty to the measurements (not shown in figure 7.2) varying smoothly from 10% at E_n = 20 MeV to 4% at E_n = 63 MeV.

It can be seen that the efficiency of this scintillator for detecting neutrons is approximately uniform over this energy range since the contribution due to the n-^{12}C interactions increases as the n-p elastic scattering component decreases. As the total efficiency is approximately independent to the incident neutron energy, it may be implied that the true form of the neutron spectrum (expressed per unit of energy) is representented by the measurements of this work.

In a similar manner, the efficiency of the scintillator for a low pulse height thresholds greater than 3 MeVee was also determined by setting higher low pulse height threshold than that set on the LINK during running. Figure 7.3 shows the total efficiency for the scintillator to detect incident neutrons in the range 20-63 MeV when operating at low pulse height thresholds of 3, 5, and 7 MeVee respectively. The sets of measurements for 5 and 7 MeVee display similar features as those described for the 3 MeVee measurements as described above. Once again, the systematic uncertainty arising from the thin scintillator approximation is not included in the error bars shown.

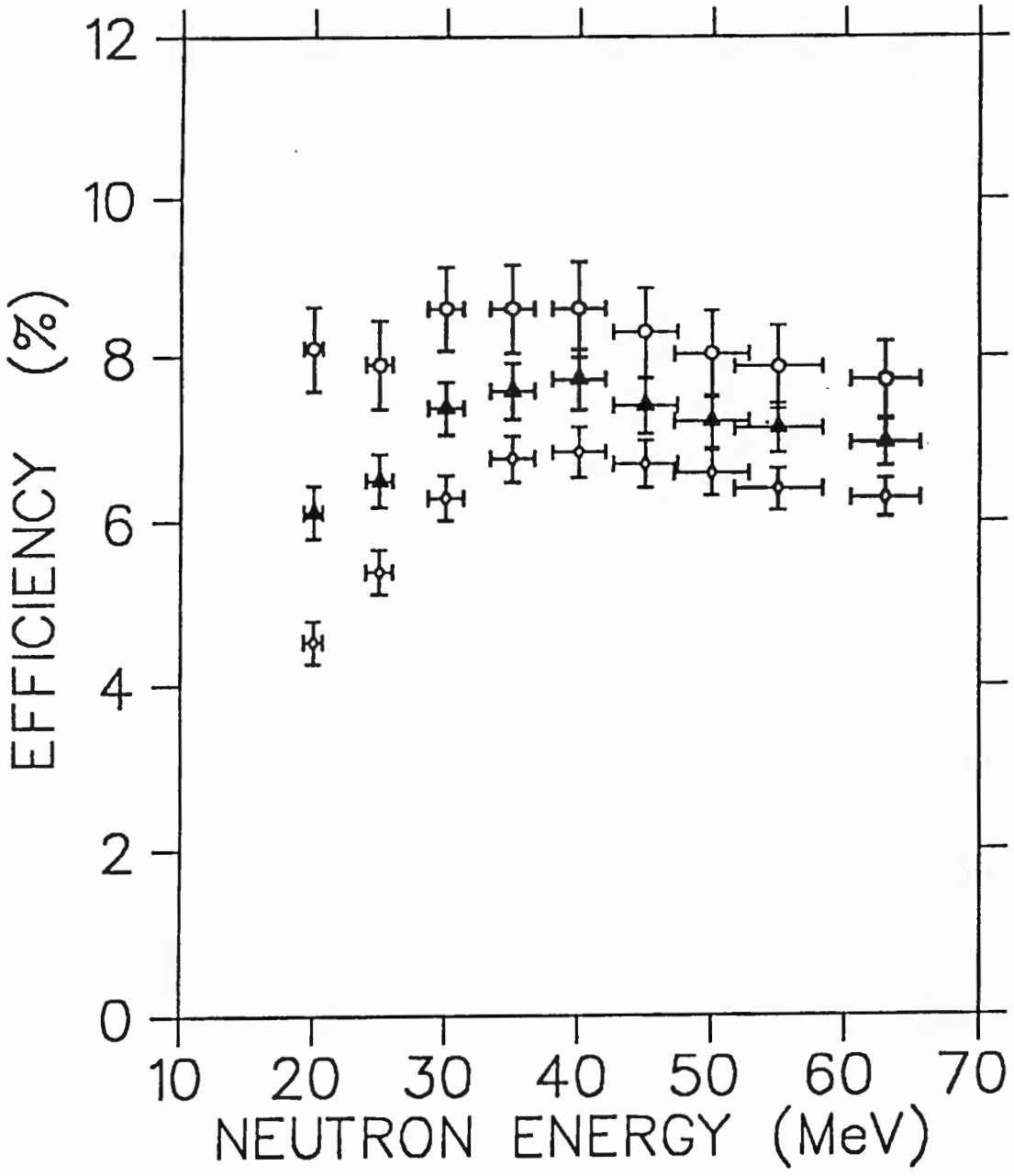

Figure 7.4 Neutron detection efficiency of a 5 cm by 5 cm (diameter) cylinder of NE213, determined relative to the calculated efficiency for n-p elastic scattering events (see text) for a low detection threshold of (○) 3, (▲) 5 and 7 (◇) MeVee. The scintillator was placed with its curved surface facing the incident neutron beam.

CHAPTER 8

CONCLUSION

8.1 SUMMARY AND DISCUSSION

In conclusion, the following has been achieved with respect to the objectives of this work as laid out in section 1.5.

Firstly, the response functions of a 5 cm (diameter) by 5 cm cylindrical NE213 scintillator were measured with good statistics for monoenergetic neutrons, measured and selected by time of flight, in the range 15-63 MeV. These lineshapes were unfolded into pulse height spectra for charged particles emitted in neutron-induced interactions in the scintillator and identified as protons, deuterons and alphas by pulse shape discrimination. Two methods of separating the different charged particle signals were used (see section 3.2) and it was found that a better degree of separation was attained by the second method of fitting Gaussians, in particular in the region of lower pulse height where the separation of the charged particle ridges diminished (see figure 3.5). The pulse shape discrimination also allowed a

finer separation of the signals of the two competing alpha reactions, namely $^{12}C(n,\alpha)^{9}Be$ and $^{12}C(n,n')3\alpha$.

The lineshape measured for neutrons of energy 63 MeV, when unfolded into its charged particle components, provided information regarding reaction mechanisms for neutron induced proton, deuteron and alpha production from ^{12}C at that energy. Many of the results obtained at 63 MeV are applicable for the wider incident neutron energy range of 15-63 MeV. A Monte Carlo code (He91) was used to separate the n-p elastic scattering component from the n-^{12}C component of the response function. Accurate knowledge of the $^{1}H(n,n)^{1}H$ component forms part of the investigations concerning n-p radiative capture at E_n = 63 MeV (see Appendix C). A comparison was made between the proton and deuteron pulse height spectra measured in this work and the simulated spectra of the *SCINFUL* Monte Carlo code (Di88). In both cases, although the overall agreement between the code and the present measurements was generally good, the (n,np) and (n,nd) continua, respectively, were found to have been underestimated by the program.

The pulse height spectra for protons, deuterons and alphas, measured as a function of neutron energy, each displayed features which, when identified with specific energy, provided a means of measuring the response (light output) of NE213 to protons, deuterons and alphas. The pulse height scale was calibrated in units of MeV (electron equivalent) by measuring the pulse height spectrum of the 4.44 MeV γ-ray from an AmBe source under the same conditions as the measurements with the neutron beam. A form of the Birks relation (equation 4.3) was fitted separately to the proton, deuteron and alpha response data. The response theory of Birks was confirmed over this energy range as the Birks parameters, determined from the fits for protons, deuterons and alphas respectively, agreed well with each other within reasonable experimental uncertainty. The mean value of the Birks parameter as determined in this work was $B = 0.0147 \pm 0.0001$ g.cm^{-2}.MeV^{-1}. In addition, the proton response measurements of the current work agreed well with other published results. Coefficients for the empirical formula of Madey (equation 4.4) for the response of a scintillator to charged particles were also

determined for the proton, deuteron and alpha response data. This formula, although having no physical basis, may be made to fit the data well, and therefore provides an useful alternative for use in calculations requiring a scintillator light output relation.

The effect on the proton pulse height spectrum of protons leaving the scintillator was investigated with the use of a Monte Carlo code (He91). The n-p elastic scattering component of the proton pulse height spectrum was simulated and it was determined that six out of every seven 63 MeV protons will escape from the scintillator without depositing all of their kinetic energy. This was confirmed by a separate analytical calculation (Appendix B).

Total cross sections for neutron-induced proton, deuteron and alpha production from ^{12}C were measured as a function of incident neutron energy. These measurements were transformed to an absolute reaction cross section scale with reference to the n-p elastic scattering total cross section in the literature. These measurements were found to agree well with the few published measurements available. It may be deduced from the comparisons of the measured proton and deuteron pulse height spectra of this work and the predictions of the *SCINFUL* code, that more than 60% of the proton and deutron yields at 63 MeV may be attributed to the ^{12}C(n,np) and ^{12}C(n,nd) reactions respectively.

The efficiency of the scintillator for detection via n-p elastic scattering only was calculated as a function of neutron energy in the thin scintillator limit, assuming the elastic scattering total cross section in the literature. Measurements of the ratio of the number of n-p elastic scattering events to the number of n-^{12}C interaction events allowed the efficiency of the scintillator for detection via n-^{12}C interactions, and hence the total neutron detection efficiency, to be determined for low pulse height thresholds of 3, 5 and 7 MeVee respectively. As expected from the relative strengths of the ^{1}H(n,n)^{1}H and n-^{12}C reactions cross sections, the contribution to the efficiency attributed to n-^{12}C interactions increases appreciably with respect to the n-p elastic scattering component which falls off with increasing incident neutron

energy. This results in an approximately flat detection efficiency over this range of neutron energies.

The results of this work have proved to be significant to the analysis of the n-p radiative capture measurements, and further measurements, as outlined below (currently being analysed), will serve to further the present understanding in this field.

8.2 FURTHER DEVELOPMENTS

A number of further developments are suggested from this work. These include use of different scintillator shapes and geometries and a second scintillator to detect escaping charged particles.

As discussed in section 4.1(e), the photomultiplier voltage divider circuit used in this work (figure 2.2(a)), has been found to be unsuitable for work at incident neutron energies greater than about 15 MeV. The photomultiplier voltages required for use at the higher neutron energies resulted in space charge saturation of the photomultiplier signal. In current investigations at similar neutron energies, the standard RCA photomultiplier potential divider (figure 2.2(b)) is being used and preliminary results show an improvement on the Zener circuit.

In current work, neutron response functions have also been measured for a 13 by 13 by 7 cm rectangular NE213 scintillator. When aligned with its long axis facing the beam, the fraction of protons that will escape from the rear of the scintillator with be less than 30%. A thin (5 mm) circular NE102 plastic scintillator has been placed behind the NE213 detector to monitor these proton escapes. These will constitute the majority of escaping charged particles as the the fraction of escapes out of the sides of the scintillator will be small (~ 5%). These measurements are still awaiting analysis and are hoped to supplement the estimates of proton escape of the present work.

Measurements have also been made with the 5 cm (diameter) by 5 cm cylindrical NE213 scintillator orientated with its flat circular face towards the incident neutron beam. The circular NE102 "escape detector" has been used to monitor charged particles escaping out the sides and the rear of the detector. This monitoring of escapes is critical as measurements of the n-p radiative capture differential cross section will soon be made at E_n = 126 MeV, and higher, at which energies all recoiling protons will escape from the detector. Finally, similar measurements, as outlined in this thesis, will be made using other types of organic scintillator, such as NE230 (a deuterated liquid) and a deuterated anthracene crystal.

Appendix A

The non-relativiastic expressions for the energetics for nuclear reactions.

(Reproduced from Marion and Young (Ma68))

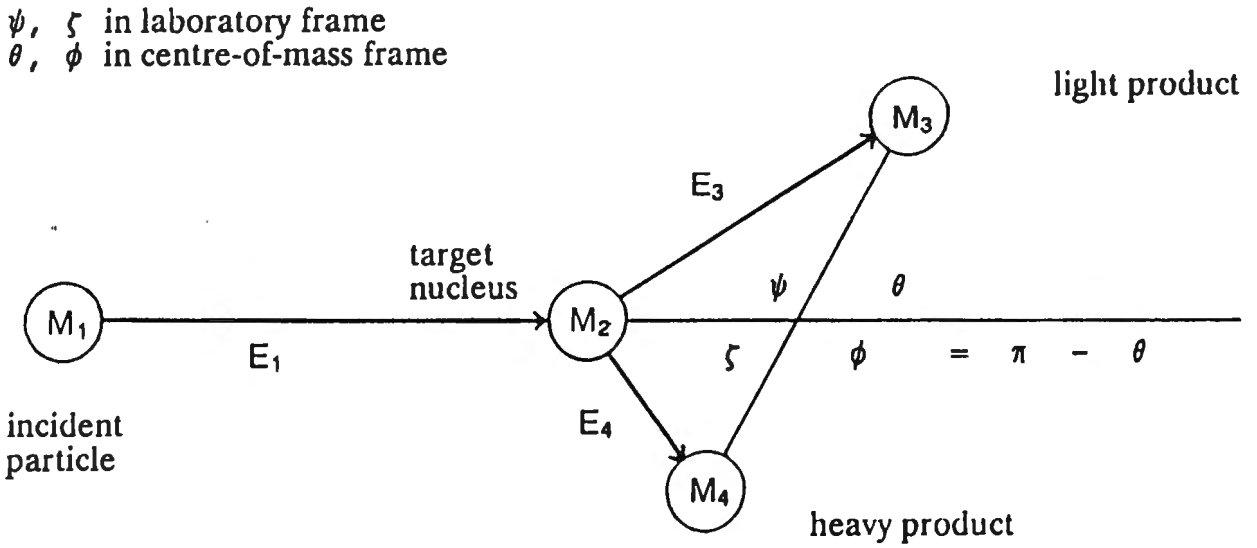

$$Q = M_1 + M_2 - M_3 - M_4$$

$$E_T = E_1 + Q = E_3 + E_4$$

Define:

$$A = \frac{M_1 M_4 (E_1 / E_T)}{(M_1 + M_2)(M_3 + M_4)}$$

$$B = \frac{M_1 M_3 (E_1 / E_T)}{(M_1 + M_2)(M_3 + M_4)}$$

$$C = \frac{M_2 M_3}{(M_1 + M_2)(M_3 + M_4)} \left(1 + \frac{M_1 Q}{M_2 E_T}\right)$$

$$D = \frac{M_2 M_4}{(M_1 + M_2)(M_3 + M_4)} \left(1 + \frac{M_1 Q}{M_2 E_T}\right)$$

$$A + B + C + D = 1$$

Then the laboratory energy of the light product, E_T, is given by:

$$E_3 = E_T \{ B + D + 2 (A C)^{1/2} \cos\theta \}$$

$$= E_T \{ B [\cos\psi + (D / B - \sin^2\psi)^{1/2}]^2 \}$$

Appendix B

Calculation of the ratio of the total number protons which recoil directly forward from $^1H(n,n)^1H$ events in a scintillator to the number of such protons which do not escape from the detector.

Consider the case of neutrons incident on the curved surface of a 5 cm (diameter) cylindrical detector, placed perpendicularly to the incident neutrons.

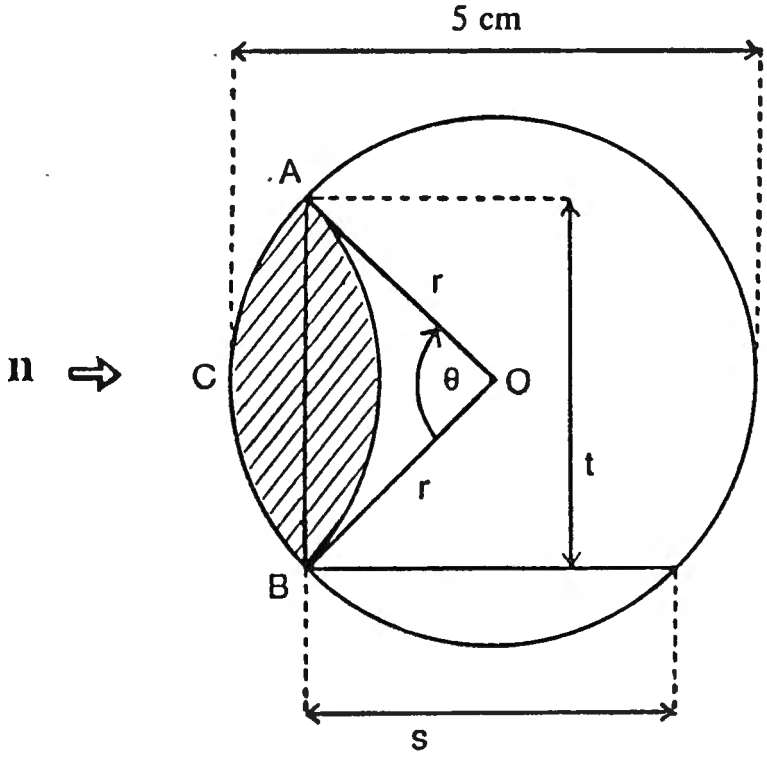

radius, r = 2.5 cm

$t^2 = 4r^2 - s^2$

Ratio of $\frac{\text{all proton events}}{\text{proton non-escapes}}$ (for protons recoiling directly forward *only*)

$= \frac{\pi r^2}{\text{shaded area}}$

Area of segment OACB = $\frac{1}{2}\theta r^2$

where θ is in radians

By the cosine rule:

$$t^2 = r^2 + r^2 + 2rr\cos\theta$$

giving

$$\theta = \cos^{-1}(1 - t^2/2r^2) = \cos^{-1}(s^2/2r^2 - 1)$$

Then the area of segment OACB $= (\frac{1}{2}r^2)\cos^{-1}(\frac{1}{2}s^2/r^2 - 1)$

Area of $\Delta ABO = \frac{1}{4}ts = \frac{1}{4}s\sqrt{4r^2 - s^2}$

Shaded area $= 2\{(\frac{1}{2}r^2)\cos^{-1}(\frac{1}{2}s^2/r^2 - 1) - \frac{1}{4}s\sqrt{4r^2 - s^2}\}$

$= r^2\cos^{-1}(\frac{1}{2}s^2/r^2 - 1) - \frac{1}{2}s\sqrt{4r^2 - s^2}$

Then the ratio of $\dfrac{\text{all proton events}}{\text{proton non-escapes}}$ (for protons recoiling directly forward *only*)

$$= \frac{\pi r^2}{r^2\cos^{-1}(\frac{1}{2}s^2/r^2 - 1) - \frac{1}{2}s\sqrt{4r^2 - s^2}}$$

For incident neutrons of energy 63 MeV:

The elastically scattered protons which recoil directly forward (and thus have energy 63 MeV) have a range in NE213, s , of 3.8 cm.

Hence, for these protons *only*:

$$\frac{\text{all proton events}}{\text{proton non-escapes}} = 7.3$$

Appendix C

Reproduction of reports detailing the n-p capture experiment: (a) (Al88), (b) (Al89), and (c) (Al90).

(a)

7.1 Experimental Nuclear Physics

7.1.1 Differential cross-section for n-p radiative capture at E_n = 61 MeV

M S Allie, F D Brooks, D G Aschman, W A Cilliers, M Murray, S M Perez, D Steyn
University of Cape Town

D T L Jones, W R McMurray, J V Pilcher, J C Cornell, B R S Simpson, F D Smit
National Accelerator Centre

D W Mingay
Atomic Energy Corporation

K Bharuth-Ram
University of Durban Westville

H G Miller
University of Pretoria

I J van Heerden
University of Western Cape

The angular distribution of photons from the $^1H(n,\gamma)^2H$ reaction at E_n= 61 MeV is being studied using the new collimated neutron beam facility at NAC (see section 5.1 of this report.) Deuterons from the reaction are detected in an active proton target consisting of an NE213 liquid scintillator (50 mm diam. × 50 mm) located at the vertex of the experiment. Coincident gamma rays are detected in an array of 9 sodium iodide crystals (75 mm diam. × 125 mm) with centres at a radius of 264 mm (see figure 1). The multiparameter data which are recorded and analysed event-by-event include the incident neutron time-of-flight, the NE213 pulse height L and pulse shape S, the NaI pulse height, the coincidence time delay between NE213 and NaI, and a pattern register indicating the gamma detector (or detectors) active in the event. The off-line analysis of the multiparameter data enables the very rare np→dγ capture events to be clearly identified from their kinematics and their pulse-shape discrimination characteristics. Figure 2 shows, for example, a density plot of counts in the L-S plane obtained in 133 hours of running, from one of the NaI detectors, at a laboratory angle of 90°. The deuteron peak from np-capture is clearly identified, centred at the co-ordinates (L,S) = (36,34).

The differential cross-section for this reaction may be tranaformed by application of time-reversal invariance to a cross-section for the inverse reaction, deuteron photodisintegration at E = 31.5 MeV. There is special interest [1] in measurements at this energy because a number of experiments have reported data in disagreement with one another and with theoretical predictions. The analysis of the present measurements is now under way and comparisons are being made with calculations based on the Paris potential and other nuclear potentials. The good signal-to-background ratios obtained in the raw data (e.g. figure 2) should lead to accurate values for the differential cross-section, which should in turn permit a critical comparison with the theory.

Reference

1. J F Mathiot, J Phys. G: Nucl. Phys. 14 (1988) 5357

Fig. 1 Experimental arrangement for detecting gammas and deuterons from the np→dγ reaction. Nine NaI detectors surrounded by lead shields form a ring around the central vertex detector (NE213 liquid scintillator). The neutron beam enters through the gap in the lead shielding (top left).

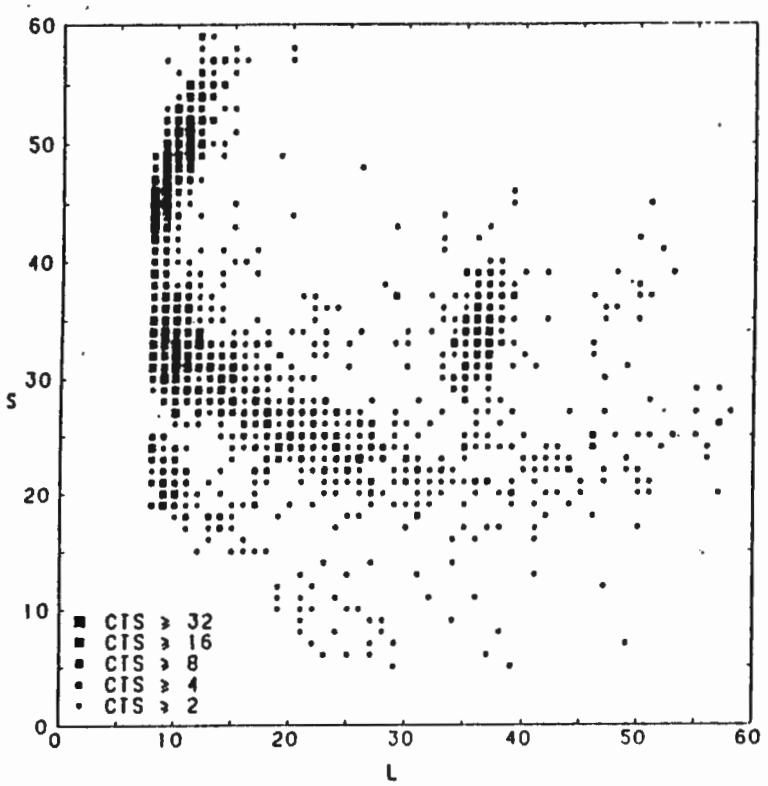

Fig. 2 Density plot of counts versus NE213 pulse height L and pulse shape S for NE213-NaI coincidences at $\theta_\gamma = 90°$. The peak centred at (L,S) = (36,34) is attributed to np→dγ events.

(b)

9.1 Experimental Nuclear Physics

9.1.1 Differential cross-section for n-p radiative capture at E_n = 63-123 MeV

M S Allie*, F D Brooks*, D G Aschman*, W A Cilliers*, M Murray*, S M Perez*, D Steyn*, D T L Jones, W R McMurray, J V Pilcher, J C Cornell, B R S Simpson, F D Smit, D W Mingay§ K Bharuth-Ram+, H G Miller$^{\phi}$, I J van Heerden$^{\neq}$

*University of Cape Town
§Atomic Anergy Corporation
+University of Durban Westville
ϕUniversity of Pretoria
$\neq$University of Western Cape

The np → dγ experiment which was outlined in the previous NAC Research Report (1) has had two further experimental runs, i.e. an additional run at E_n = 63 MeV and a preliminary run at E_n = 123 MeV. The analysis of the 63 MeV data is not yet complete and will shortly be augmented by further experimental measurements which are designed to determine corrections for the effects of proton and deuteron escape from the vertex detector. These corrections must be included when the relative measurements of differential cross-sections from the experiment are reduced to an absolute cross-section scale.

In the meanwhile some interest is being focused on the ratio R of cross-sections at the angles corresponding to θ_p = 45° and 90° (laboratory) in the inverse deuteron-photodisintegration reaction, $^2H(\gamma,p)n$ at $E\gamma$ = 34 MeV. The preliminary analysis of the np → dγ data gives R = 0.61 ± 0.07, compared with the value R = 0.71 obtained from photodisintegration experiments (2). Kassaee et al. (3) have recently drawn attention to the importance of the ratio R as an indicator of the contribution of E2 transitions to np → dγ.

References

1. National Accelerator Centre Annual Report (1988) item 7.1.1

2. W Jaus and W S Woolcock, Nucl. Phys. A473 (1987) 685

3. A Kassaee, L N Pandey, M L Rustgi and E Hadjimichael, Phys. Rev. C39 (1989) 1147

(c)

7.1 Experimental Nuclear Physics

7.1.1 Differential cross-section for n-p radiative capture at E_n= 63 MeV

M S Allie*, F D Brooks*, D G Aschman*, A Buffler*, W A Cilliers*, C Henderson*, D Steyn*, M Murray*, W R McMurray, F D Smit, B R S Simpson, J C Cornell, K Bharuth-Ram§, H Miller+, I J van Heerden$^{\phi}$

* University of Cape Town
§ University of Durban Westville
\+ University of Pretoria
ϕ University of Western Cape

The angular distribution of photons from the $^1H(n,\gamma)^2H$ reaction at E_n=63 MeV is being investigated as outlined in previous NAC reports (1). Preliminary analysis of the data has been completed. This includes kinematic corrections as well as an estimate of the gamma detector efficiency at each angle studied.

In order to compare the results with previous measurements and with theory the angular distribution is transformed into a photoproton differential cross-section for the inverse photodisintegration reaction for the corresponding centre-of-mass photon energy of 33 MeV. Our measurements are shown in figure 1 together with the theoretical predictions of Jaus and Woolcock (2). The experimental data were normalised so as to give the same integrated capture cross-section as the theory. The error bars indicated are purely statistical.

It is clear that a fit to experiment will result in a curve that rises more steeply and is also more peaked at 90° than that predicted by theory. However, in order to be able to ascertain the physics implications of this possible discrepancy it is necessary to reduce our measurements to an absolute cross-section scale. We have therefore undertaken further n-p capture measurements with seven gamma detectors at 90° to the beam in order to determine the differential capture cross-section at this angle relative to the well-known n-p elastic scattering cross-section for the incident neutron energy of 63 MeV. The ratio of n-p captures to n-p elastic scatters (in the NE213 vertex detector) is determined directly from these measurements. The data are now being analysed and a careful study is being made to estimate the extent of neutron-carbon reactions as well as edge effects due to the escape of protons in the vertex detector (see item 7.1.3 of this report).

References

1. National Accelerator Centre Annual Reports NAC/AR/88-01 (1988) item 7.1.1 and NAC/AR/89-01 (1989) item 9.1.1

2. W Jaus and W S Woolcock, Nucl. Phys. A473 (1987) 685.

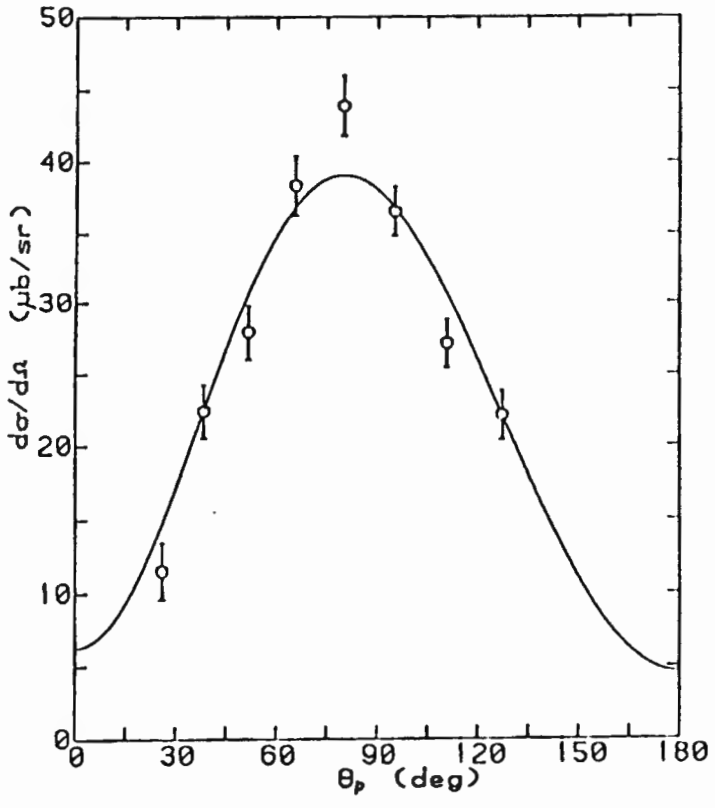

Fig. 1 Differential cross-section for the $^2H(\gamma,p)$ reaction at E_γ=33 MeV, showing the theoretical calculation of Jaus and Woolcock (curve) and the experimental data calculated from the inverse n-p capture measurements at E_n=63 MeV. The experimental data have been normalised to the theory as described in the text.

REFERENCES

Aj84 F.Ajzenberg-Selove *Nuclear Physics* **A413** (1984) 1

Aj85 F.Ajzenberg-Selove *Nuclear Physics* **A433** (1985) 1

Al88 M.S.Allie, F.D.Brooks, D.G.Aschman, W.A.Cilliers, M.Murray, S.M.Perez, D.Steyn, D.T.L.Jones, W.R.McMurray, J.V.Pilcher, F.D.Smit, B.R.S.Simpson, J.C.Cornell, D.W.Mingay, K.Bharuth-Ram, H.Miller, I.J.van Heerden National Accelerator Centre Annual Report **NAC/AR/88-01** (1988) item 7.1.1

Al89 M.S.Allie, F.D.Brooks, D.G.Aschman, W.A.Cilliers, M.Murray, S.M.Perez, D.Steyn, D.T.L.Jones, W.R.McMurray, J.V.Pilcher, F.D.Smit, B.R.S.Simpson, J.C.Cornell, D.W.Mingay, K.Bharuth-Ram, H.G.Miller, I.J.van Heerden National Accelerator Centre Annual Report **NAC/AR/89-01** (1988) item 9.1.1

Al90 M.S.Allie, F.D.Brooks, D.G.Aschman, A. Buffler, W.A.Cilliers, C.Henderson, D.Steyn, M.Murray, W.R.McMurray, F.D.Smit, B.R.S.Simpson, J.C.Cornell, K.Bharuth-Ram, H.G.Miller, I.J.van Heerden National Accelerator Centre Annual Report **NAC/AR/90-01** (1990) item 7.1.1

An75 B.Antolkovic & Z.Dolenec *Nuclear Physics* **A237** (1975) 2 5

An76 B.Antolkolvic *Fizika* **8** (1976) 163

An79 M.Anghinolfi, G.Ricco, P.Corvisiero & F.Masulli *Nucl. Instr. and Meth.* **165** (1979) 217

An83 B.Antolkovic, I.Šlaus, P.Macq, J.P.Meulders & D.Plenkovic *Nuclear Physics* **A394** (1983) 87

Au72 M.Auman, F.P.Brady. J.A.Jungerman, W.J.Knox, M.R.McGie & T.C.Montgomery *Phys. Rev. C* **5** (1972) 1

Be89 P.Bennett & C.J.Kost OPDATA (version 2.99) **TRI-CD-87-04**, available from TRIUMF, 4004 Wesbrook Mall, Vancouver, Canada V6T 2A3

Bi51 J.B.Birks *Proc. Phys. Soc.* **A64** (1951) 874

Br79 F.D.Brooks *Nucl. Instr. and Meth.* **162** (1979) 477

Br84 F.P.Brady, G.A. Needham, J.L.Ullman, C.M.Castanada, T.D.Ford, N.S.P.King, J.L.Romero, M.L.Webb, V.R.Brown & C.H.Poppe *J.Phys. G: Nucl. Phys.* **10** (1984) 363

Bu69 W.R.Burrus & V.V.Verbinski *Nucl. Instr. and Meth.* **67** (1969) 181

By89 R.C.Byrd & W.C.Sailor *Nucl. Instr. and Meth.* **A274** (1989) 494

Ce79 R.A.Cecil, B.D.Anderson & R.Madey *Nucl. Instr. and Meth.* **161** (1979) 439

Ci82 S.Cierjacks, M.T.Swinhoe, L.Buth, S.D.Howe, F.Raupp, H.Schmitt & L.Lehmann *Nucl. Instr. and Meth.* **192** (1982) 407

Ch90 J.L.Chuma PLOTDATA graphics package (version 10.01) **TRI-CD-87-03**, available from TRIUMF, 4004 Wesbrook Mall, Vancouver, Canada V6T 2A3

Co60 P.F.Cooper & R.Wilson *Nuclear Physics* **15** (1960) 373

Cr70 R.L.Craun & D.L.Smith *Nucl. Instr. and Meth.* **80** (1970) 29

Cu89 J.Cub, E.Finckh, K.Gebhardt, K.Geissdörfer, R.Lin, J.Strate & H.Klein *Nucl. Instr. and Meth.* **A274** (1989) 217

Cz64 J.Czirr, D.R.Nygren & C.D.Zafiratos *Nucl. Instr. and Meth.* **31** (1964) 226

De65 K.Debertin & E.Rossele *Nuclear Physics* **70** (1965) 89

De76 A.Del Guerra *Nucl. Instr. and Meth.* **135** (1976) 337

Di82 G.Dietze & H.Klein *Nucl. Instr. and Meth.* **193** (1982) 549

Di88 J.K.Dickens Oak Ridge National Laboratory Report **ORNL-6462** (1988)

Di89 J.K.Dickens *Computers in Physics* **Nov/Dec 1989** 62

Ed72 R.M.Edelstein, J.S.Russ, R.C.Thatcher, M.Elfield, E.L.Miller, N.W.Reay, N.R.Stanton, M.A.Abolins, M.T.Lin, K.W.Edwards & D.R.Gill *Nucl. Instr. and Meths.* **100** (1972) 355

El74 S.A.Elbakr, J.W.Watson & C.A.Miller *Nucl. Instr. and Meth.* **115** (1974) 115

Ep69 M.B.Epstein, H.D.Holmgren, M.Jaus, H.G.Pugh, R.G.Roos, N.S.Wall & C.D.Goodman *Phys. Rev.* **178** (1969) 1968

Fo84 T.D.Ford, G.A.Needham, F,P.Brady, J.L.Romero & C.M.Castanada *Nucl. Instr. and Meth.* **228** (1984) 81

Fr55 G.M.Frye Jr., L.Rosen & L.Stewart *Phys. Rev.* **99** (1955) 1375

Ga63 J.L.Gammel, in *Fast Neutron Physics* part 2 (Interscience, New York, 1963)

Ga70 D.I.Garber, L.G.Strömberg. M.D.Goldberg, D.E.Cullen & V.M.May *Angular Distributions in neutron-induced reactions* Volume I **BNL-400** (1970)

Go60 T.J.Gooding & H.G.Pugh *Nucl. Instr. and Meth.* **7** (1960) 189

He91 C.G.L.Henderson M.Sc. thesis (to be submitted), University of Cape Town

Ho78 P.Hodgson *New Scientist* (27 April 1978) 231

Ka47 H.Kallmann *Natur und Technik* (July 1947); I.Broser & H.Kallmann *Z. Naturforsch* **2a** (1947) 439 and 6425

Ke53 D.A.Kellogg *Phys. Rev.* **90** (1953) 2 224

Kn72 H.H.Knox & T.G.Miller *Nucl. Instr. and Meth.* **101** (1972) 519

Kr59 W.E.Kreger & B.D.Kern *Phys. Rev.* **90** 2 (1953) 224

Ku64 R.J.Kurz Lawrence Radiation Laboratory Report **UCRL 11339** (1964)

La75 J.Lachkar, F.Cocu, G.Haouat, P.leFloch, T.Patin & J.Sigaud **NEANDC (E) 168** "L" (1975)

LINK **LINK Model 5010** Pulse Shape Discriminator from LINK SYSTEMS, Halifax Road, High Wycombe, Bucks, England, HP123SE

Lo76 J.A.Lockwood, C.Chen, L.A.Friling, D.Swartz, R,N.St.Onge, A.Galonsky & R.R.Doering *Nucl. Instr. and Meth.* **138** (1976) 353

Ly75 F.J.Lynch IEEE *Trans. Nucl. Science* **NS-22** (1975) 58

Ma68 J.B.Marion & F.C.Young *Nuclear Reaction Analysis* (North Holland, Amsterdam, 1968) 161

Ma78 R.Madey, F.M.Waterman, A.R.Baldwin, J.N.Knudsen, J.D.Carlson & J.Rappaport *Nucl. Instr. and Meth.* **151** (1978) 445

Mc74 M.W.McNaughton, F.P.Brady, W.B.Broste, A.L.Sagle & S.W.Johnson *Nucl. Instr. & Meth.* **116** (1974) 25

Mc75 M.W.McNaughton, N.S.P.King, F.P.Brady & J.L.Ullmann *Nucl. Instr. and Meth.* **129** (1975) 241

Me67 D.F.Measday & J.N.Palmieri *Phys. Rev.* **161** (1967) 4 161

Mo73 T.C.Montgomery, F.P.Brady, B.E.Bonner, W.B.Broste & M.W.McNaughton *Phys. Rev. Lett.* **31** (1973) 10 640

NAC NATIONAL ACCELERATOR CENTRE, P.O.Box 72, Faure, Republic of South Africa, 7131

NE NE213 liquid scintillator specification sheet, available from NUCLEAR ENTERPRISES Technology Limited, Sighthill, Edinburgh, Scotland EH11 4BY

No70 L.C.Northcliffe, C.W.Lewis & D.P.Sailor *Nucl. Instr. and Meth.* **83** (1970) 93

Pa75 G.Pauletta & F.D.Brooks *Nuclear Physics* **A255** (1975) 267

Pa90 A.Pantaleo, L.Fiore, G.Guarino, V.Paticchio, G.D'eraśmo, E.M.Fiore & N.Colonna *Nucl. Instr. & Meth.* **A291** (1990) 570

Pe79 L.J.Perkins & M.C.Scott *Nucl. Instr. and Meth.* **166** (1979) 451

RCA RCA Specification Sheet **6-72**, available from RCA Electronic Components, Harrison, NJ 07029

Ri68 E.M.Rimmer & E.Rossele *Nuclear Physics* **A108** (1968) 567

Ro75 P.G.Roos, N.S.Chant, A.A.Cowley, D.A.Goldberg, H.D.Holmgren & R.Woody III *Phys. Rev. C* **15** (1977) 69

Sl76 I.Šlaus Lowell Conference Proceedings Volume II (1976) 273

Sm68 D.L.Smith, R.G.Polk & T.G.Miller *Nucl. Instr. and Meth.* **64** (1968) 451

Sm86 F.D.Smit Ph.D. thesis (unpublished), University of Cape Town

St64 J.R.Steyn, M.D.Goldberg, B.A.Magurno & R.Wiener-Chasman *Neutron cross sections* Volume I **BNL-325** (1964)

St71 N.R.Stanton Ihio State University Report **COO-1545-92** (1971)

St75 R. St.Onge, A.Galonsky, R.K.Jolly & T.M.Amos *Nucl. Instr. and Meth.* **126** (1975) 391

Su83 T.S.Subramanian, J.L.Romero, F.P.Brady, J.W.Watson, D.H.Fitzgerald, R.Garrett, G.A.Needham, J.L.Ullmann, C.I.Zanelli, D.J.Brenner & R.E.Prael *Phys. Rev. C* **28** (1983) 2 521

Te68 R.E.Textor & V.V.Verbinski Oak Ridge National Laboratory Report **ORNL-4160** (1968)

Th71 S.T.Thornton & T.R.Smith *Nucl. Instr. and Meth.* **96** (1971) 551

Un79 B.Y.Underwood *Nucl. Instr. and Meth.* **165** (1979) 523

Uw82 Y.Uwamino, K.Shin, M.Fujii & T.Nakamura *Nucl. Instr. and Meth.* **204** (1982) 179

Ve68 V.V.Verbinski, W.R.Burrus, T.A.Love, W.Zobel & N.W.Hill *Nucl. Instr. and Meth.* **65** (1968) 8

Vo68 R.Voltz, H. du Pont & G.Laustrait *J. Physique* **29** (1968) 297

Wa74 J.W.Watson & R.G.Graves *Nucl. Instr. and Meth.* **117** (1974) 541

Yo69 J.C.Young, J.L.Romero, F.P.Brady & J.R.Morales *Nucl. Instr. and Meth.* **68** (1969) 333